Volume 23 & 24, June & December 2018 ISSN : 1816-1081

Bangladesh Journal of Physics

Editorial Board

Volume 23 & 24, June & December 2018 ISSN : 1816-1081

Bangladesh Journal of Physics

Published By :
Bangladesh Physical Society
All communications to:
The Editor, Bangladesh Journal of Physics
Department of Physics
Bangladesh University of Engineering and Technology (BUET)
Dhaka 1000, Bangladesh
E-mail : bjp_bps@yahoo.com

Price :
Individual : Tk. 2000.00
Institutional : Tk. 2000.00
Foreign : US$ 40.00

Printed at :
ADS Printing Press
234/1 Elephant Road, Dhaka 1205
Tel : 01817078796

Editorial

The creation of new scientific knowledge and its communication are inextricably bound together. It is not enough that a researcher discovers a new scientific knowledge, it is also essential that his new idea is agreed to by other scientists working in the field. Thus the task of invention and its communication, the production and dissemination of the results of research go hand in hand. This constitutes the reason why the referring system has been introduced to ensure that the individual scientists use suitable and trustworthy methods for communicating the work that constitutes his claim to priority. Scientific publications have a structural order and not chaotic and thus are ruled by a particular set of norms. The constraint imposed on the body of scientific knowledge is that it must have objectivity, emotional neutrality, disinterestedness and generality. Science, when thus looked at a social system, can not be treated merely as a body of knowledge or a set of methods or techniques but as an organized social activity of the scientists who are engaged in extending the body of empirical knowledge. According to Storer the relationship among these people who are guided by the scientific norms constitute the social characteristics of science. There are other sociologists of Science like Kuhn who are concerned with identifying the characteristics of scientific knowledge that bring about change in scientific ideas rather than with identifying external influences upon this process. We are thus faced with two opposite views about the relation between science and society. One is concerned with the influence of social institutions upon the development which follows Mark's idea and the others stress the view that ideas are not entirely affected by material factors and they play an independent role in society. This view is in keeping with the Webers idea. It appears that although there is some evidence to support either of these ideas, no idealized concept of science and its relation to society can work permanently. This is because science is basically a dynamic and creative activity where high emphasis upon inventiveness, originality and criticisms are essentially needed.

The development of scientific communication to the stage of assuming the structure of a scientific journal, and the growth of science to the stage of bringing about a scientific revolution appears to be correlated in respect of space and time. This can be seen from the fact that the initiation of scientific journals, and the sudden rise of scientific activity manifested through the technological revolution, took place in Europe in the seventeenth century. Scientific growth represents an accretion of many innovations, small or big and in the process of the development authors build upon each other contributions. This is reflected in the citation of each other works. Thus the growth of scientific knowledge is a kind of diffusion process in which ideas are transmitted from person to person. The exponential increase in the number of adopters of new ideas has been explained as a social process. When the members of a research area are interacting with each other, there should be a period of exponential growth. This is because the probability that scientists who have not previously published in the new area will increase in proportion to the number of people who have already adopted it. This should be reflected in the growth of the number of publications and the number of new authors publishing for the first time. When members of a research area are not interacting with each other and with the scientists who have not published in the area, the growth rate should be linear. Scientific journals as a formal means of communicating scientific discovery have special functions and uniqueness. Publication in journals is going through the process of editing and referring and organized skepticism of the community of scientists develops a norm and order. It keeps permanent record of original ideas documenting the priority of discovery, evaluating the contributions and comparing the relative merits and developments of different fields while treatise and books require that the author must complete his work before publication. In a scientific journal every phase of development of a grand idea may be published stage by stage enriched by feedback from the fellow scientists.

M. A. Asgar

Acknowledgement

We are grateful to the Ministry of Science and Technology, Government of the People's Republic of Bangladesh for the Grant to the Bangladesh Physical Society to Publish Society's Journal "Bangladesh Journal of Physics".

Volume 23 & 24, June & December 2018 *ISSN : 1816-1081*

Bangladesh Journal of Physics

CONTENTS

*Bangladesh Journal of Physics, **23 & 24**, 1-8, 2018*

DISTRIBUTION OF RADIONUCLIDES IN SEDIMENT OF THE BAY OF BENGAL, BANGLADESH

M. M. RAHMAN[1*], H. M. MAHFUJ[1], Q. M. RASHED-NIZAM[1], S. I. BHUIAN[2] AND M. KAMAL[2]

[1]*Department of Physics, University of Chittagong, Chittagong-4331, Bangladesh*

[2]*Atomic Energy Center, Chittagong, Chittagong-4210, Bangladesh*

[*]*Corresponding author: E-mail: mashiur72@yahoo.com*

Received on 30.07.2017, Revised received on 09.06.2018, Accepted for publication on 10.06.2018

ABSTRACT

The distribution of natural and anthropogenic radionuclides in sediments along the Bay of Bengal from Sitakunda, Chittagong to Teknaf, Cox's Bazar was measured by using gamma ray spectroscopy. The activity of ^{238}U, ^{232}Th and ^{40}K were found to be, on average, 42.6±6.3 Bq.kg^{-1}, 83.4±10.7 Bq.kg^{-1} and 448.6±20.7 Bq.kg^{-1}, respectively. Annual effective outdoor dose to adults in the coastal region of the Bay of Bengal was found higher than the world average value of 0.07 mSv. Ratio of the concentration of ^{232}Th to ^{238}U in the sediments of this bay was observed to be around 2.0. Anthropogenic radionuclide ^{137}Cs was not observed anywhere in this coastal area.

Keywords: Terrestrial radioactivity, Gamma spectroscopy, Absorbed dose rate, Bay of Bengal, Fukushima nuclear accident.

1. INTRODUCTION

On 11 March 2011, there happened a sever nuclear accident at the Fukushima Daiichi Nuclear Power Plant at Fukushima Prefecture, Japan due to the tsunami followed by the Tohoku 9.0-magnitude earthquake [1]. This accident released a huge amount of radioactivity into the environment. Release of radioactive nuclides ^{131}I and ^{137}Cs was estimated in the range of 100-500 petabecquerels (PBq) and 6-20 PBq, respectively. A large portion of these release flowed into the Pacific Ocean due to wind flow. Tsunami water also caused a release of radioactive material directly to the ocean. This direct release was estimated to an amount of 10-50 PBq ^{131}I and 3-10 PBq ^{137}Cs [2]. Although Bay of Bengal is far from the Pacific Ocean, one day it will become contaminated with the radioactivity released from the Fukushima nuclear disaster. In order to assess the contamination due to the Fukushima disaster, it is necessary to measure the concentrations and distribution of natural and anthropogenic radionuclides in the sediments of the Bay of Bengal before the contamination.

Naturally soil contains different radioactive nuclides; these are mainly daughter nuclides of ^{238}U and ^{232}Th. Apart from these, ^{40}K is a dominant natural radionuclide in soils. Concentration of these natural radionuclides varies from place to place [3]. So, the survey of radionuclides in soil and sediments has become an interested research area all over the world [4-10]. This study has been conducted along the western costal line of the Bay of Bengal, Chittagong Division, Bangladesh. This costal line is the meeting place of all the rivers in this region [11]. The largest river in Chittagong is the Karnaphuli river and its tributaries e.g., Rainkhiang, Kasalong, Halda and Ichamati. Marking the eastern boundary of the port city Chittagong, it flows into the Bay of

Bengal at Patenga, Chittagong. Along with the naturally washed-off sand and mud, it carries all the industrial and domestic wastes of Chittagong and nearby regions into the Bay of Bengal. Other rivers e.g., Sangu, Matamuhuri, and Bakkhali, etc. carry the agricultural and domestic wastes into the Bay of Bengal. These wastages may contaminate the sediments of the Bay of Bengal. Another potential source of contamination is the ship-breaking industrial area located in the Sitakunda coastal area, Kumira, Chittagong. This study provides the data on terrestrial radionuclides in the regions along the Bay of Bengal before the sediments get contaminated by the radionuclides released from the Fukushima disaster.

2. MATERIALS AND METHODS

2.1 Sample collection

Beach of the Bay of Bengal stretched from Sitakunda, Chittagong to Teknaf, Cox's Bazar was chosen as the sampling site. The distance between Sitakunda and Teknaf along the Bay of Bengal is about 220 km. Based on the ease of transportation, sediment samples were collected from 17 places along this long coastal line. Table-1 shows the location of the sample collection sites. Sweeping away all kinds of non-sediment material from each sampling site, sediment samples are collected from surface to 5 cm depth by using an iron corer of inner diameter 10 cm. These samples were collected during the month of June, 2011.

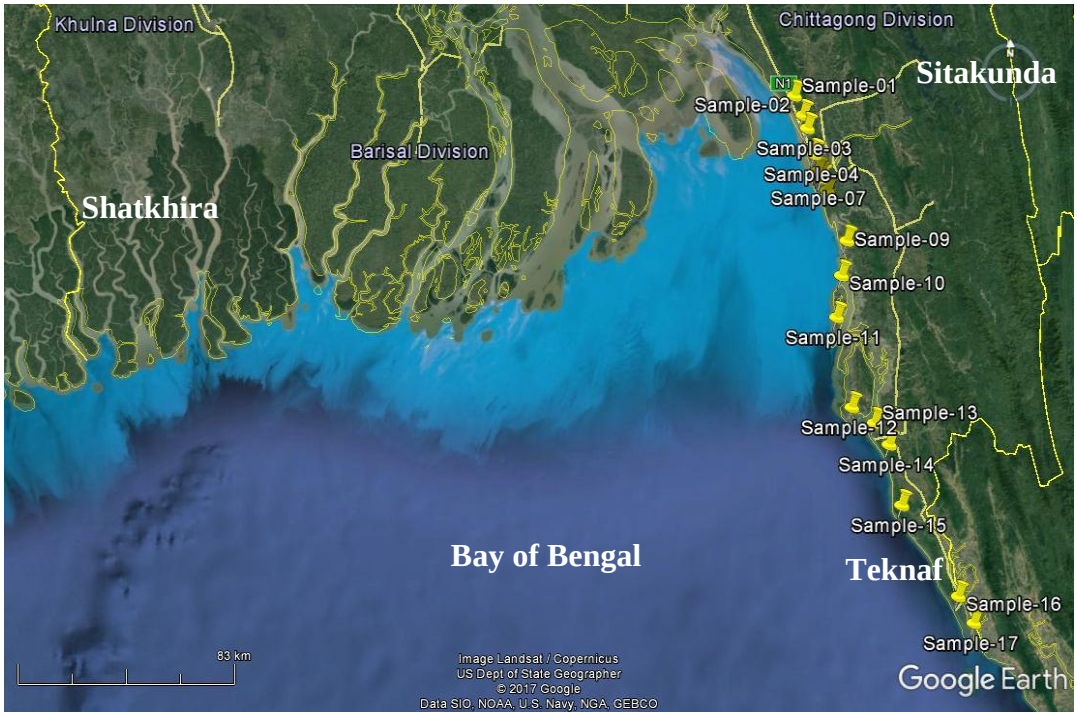

Fig 1. Sampling Sites from Sitakunda, Chittagong to Teknaf, Cox's Bazar.

Table 1: Location of sample collection sites

Sample Id	Location		
	Local Name	Latitude	Longitude
Sample-01	Sandwip Ship Ghat, Kumira, Sitakunda	22°30'22.87"N	91°41'51.88"E
Sample-02	Bhatiari, Chittagong	22°26'31.10"N	91°43'45.06"E
Sample-03	North Salimpur, Chittagong	22°23'56.44"N	91°44'36.16"E
Sample-04	Ananda Bazar Beach, North Halishahar, Chittagong	22°18'47.28"N	91°46'02.21"E
Sample-05	Khejurtola Beach, Katgar, Chittagong	22°15'22.41"N	91°46'38.51"E
Sample-06	Golden Beach, Katgar, Chittagong	22°14'42.70"N	91°47'03.89"E
Sample-07	Patenga Sea Beach, Chittagong	22°14'4.51"N	91°47'30.45"E
Sample-08	Parki Sea Beach, Anwara	22°11'36.10"N	91°48'45.17"E
Sample-09	North Bahar Chara, Banshkhali	22° 1'37.80"N	91°52'52.94"E
Sample-10	Northern side of Kutubdia Island, Cox's Bazar	21°54'47.79"N	91°51'33.13"E
Sample-11	Southern side of Kutubdia Island, Cox's Bazar	21°46'35.45"N	91°50'19.30"E
Sample-12	Soadia Island, Moheskhali, Cox's Bazar	21°28'47.55"N	91°53'20.72"E
Sample-13	Laboni Sea Beach, Cox's Bazar	21°25'36.40"N	91°58'15.62"E
Sample-14	Himchari Sea Beach, Cox's Bazar	21°21'17.62"N	92° 1'26.67"E
Sample-15	Inani Sea Beach, Cox's Bazar	21° 9'15.85"N	92° 4'00.45"E
Sample-16	Teknaf Sea Beach, Teknaf	20°50'53.94"N	92°16'15.54"E
Sample-17	Dakhinpara, Teknaf	20°45'28.51"N	92°19'37.33"E

2.2 Sample preparation

Sediment samples were prepared by following the standard procedures [12]. Sediment samples were dried at first under the sun and then cleaned to remove pebbles, roots and any other non-sediment impurity. These sun-dried samples are grinded by mortar and pestle in order to bring homogeneity in the samples. Then the samples were dried in an electrical oven at a temperature 100°C until the water contents were evaporated. Then the samples were kept in some air-tight plastic container for a period of more than one month to ensure the state of secular equilibrium among the long lived parent radionuclides (e.g., ^{226}Ra in uranium-238 series) and their short lived daughter radionuclides (e.g., ^{222}Rn in uranium-238 series). Masses of the dried samples were also recorded by an electronic balance.

2.3 Analysis of sediment samples

A High Purity Germanium (HPGe) detector (IG2020, SN-2251 made by Canberra Industries Inc, USA) was used to carry out the gamma spectroscopy of the sediment samples. The measured

resolution of the detector was 1.83 keV (FWHM) at gamma ray energy 1332 keV of ^{60}Co. Calibration and efficiency measurement of the detection system was performed by using the standard gamma sources provided by International Atomic Energy Agency (IAEA). Gamma emission from each sample was recorded for 20,000 seconds. The gamma spectrum of the sediment samples was analyzed by using the software Genie-2000.

2.4 Estimation of activity concentration and radiological hazard parameters

From the gamma spectrum of each sample, net gamma emission per second (C_{net} in Bq) for different radionuclides is recorded. Then the activity concentration (A in Bq.kg^{-1}) of each radionuclide is determined by the unitary method:

$$A = \frac{C_{net}}{\varepsilon\, i\, m} \tag{1}$$

Here, ε is the efficiency of the emission of a gamma energy from a radionuclide, i is the intensity of the emission of that gamma energy and m is the mass of the sediment samples in kg. The activity concentration of ^{238}U was calculated by averaging the measured activities of ^{214}Pb (295.22 and 351.93 keV lines), and ^{214}Bi (609.31, 1120.29 and 1238.11 keV lines). For the estimation of the activity of ^{232}Th, the measured activities of ^{228}Ac (338.32, 911.20 and 968.97 keV lines), ^{212}Pb (238.63 keV line), ^{212}Bi (727.33 keV line), and ^{208}Tl (583.19 keV line) were taken into consideration. For the activity concentration of radionuclide ^{40}K, emission of 1460.8 keV gamma was considered. For the estimation of anthropogenic radionuclide ^{137}Cs, emission of 661.66 keV gamma was observed. The intensities of these gamma emissions were taken from the library Nuclide-LARA [13].

Activity concentrations of ^{238}U, ^{232}Th and ^{40}K in sediment and soil samples are significantly different in different places. So, in order to compare the radiation hazard due to these radionuclides in different places, it is customary to assess the outdoor absorbed dose rate (D in $nGy.h^{-1}$) in air at one meter above the ground by using the following equation [14]:

$$D\ (nGy.h^{-1}) = 0.462A_U + 0.604\ A_{Th} + 0.0417\ A_K \tag{2}$$

Here A_U, A_{Th} and A_K are the activity concentrations of ^{238}U, ^{232}Th and ^{40}K, respectively in sediments and soils in the unit of $Bq.kg^{-1}$. The average annual effective dose (H) to adults is estimated from the outdoor exposure D but it is expressed in milli-Sievert (mSv) rather than Gray (Gy). For this purpose United Nations Scientific Committee on the Effects of Atomic Radiation (UNSCEAR) proposed in 2008 [14] that the general people stay outdoor 20% time in a day and the Gray (Gy) to Sievert (Sv) transformation factor is 0.7 $Sv.Gy^{-1}$. Then the equation for H becomes

$$H\ (mSv) = D\ (nGy.h^{-1}) \times 8760h \times 0.2 \times 0.7\ Sv.Gy^{-1} \times 10^{-6} \tag{3}$$

Another common radiological hazard parameter is the radium equivalent activity (Ra_{eq} in $Bq.kg^{-1}$). It was calculated by using the following equation [15]:

$$Ra_{eq} = A_U + 1.43\ A_{Th} + 0.77\ A_K \tag{4}$$

3. RESULTS AND DISCUSSION

Table 2: Activity concentrations of natural terrestrial radionuclides in sediments

Location	Activity Concentration (Bq.kg^{-1})		
	^{238}U	^{232}Th	^{40}K
Sandwip Ship Ghat, Kumira, Sitakunda	46.9±6.5	70.6±9.9	424.4±20.6
Bhatiari, Chittagong	56.3±7.5	75.0±8.4	462.8±21.5
North Salimpur, Chittagong	52.6±7.2	79.2±10.5	447.1±21.2
Ananda Bazar Beach, North Halishahar, Chittagong	33.4±5.6	59.0±7.7	670.6±25.9
Khejurtola Beach, Katgar, Chittagong	50.1±6.7	81.8±9.0	394.1±19.9
Golden Beach, Katgar, Chittagong	60.1±8.1	113.6±12.2	307.4±17.5
Patenga Sea Beach, Chittagong	34.2± 5.3	67.1±8.2	761.6±27.6
Parki Sea Beach, Anwara	28.2±5.1	60.0±9.3	470.7±21.7
North Bahar Chara, Banshkhali	42.1±6.3	94.0±11.7	1056.8 ±32.5
Northern side of Kutubdia Island, Cox's Bazar	60.87±7.7	101.40±12.3	1460.8±38.2
Southern side of Kutubdia Island, Cox's Bazar	66.2±8.1	119.8±13.1	499.3±22.4
Soadia Island, Moheskhali, Cox's Bazar	23.3±4.8	57.8±9.0	613.4±24.8
Laboni Sea Beach, Cox's Bazar	51.8±7.0	86.2±11.2	201.0±14.2
Himchari Sea Beach, Cox's Bazar	28.3±5.1	76.8±10.0	461.4±21.5
Inani Sea Beach, Cox's Bazar	62.3±7.8	125.7±13.1	364.1±19.1
Teknaf Sea Beach, Teknaf	109.6±10.4	255.9±19.2	302.9±17.4
Dakhinpara, Teknaf	41.4±6.4	87.7±11.3	507.0±22.5
Average	**42.6±6.3**	**83.4±10.7**	**448.6±20.7**

The three natural radionuclides ^{238}U, ^{232}Th, and ^{40}K were found to vary significantly from Sitakunda to Teknaf along the Bay of Bengal, as shown in the Table-2. ^{238}U and ^{232}Th were observed to be very high – 109.6±10.4 *Bq.kg*$^{-1}$ and 255.9±19.2 *Bq.kg*$^{-1}$, respectively, at Teknaf Sea Beach, Cox's Bazar. In other places, the specific activity of ^{238}U ranged from 23.3±4.8 Bq.kg^{-1} to 66.2±8.1 Bq.kg^{-1} and ^{232}Th ranged from 57.8±9.0 Bq.kg^{-1} to 119.8±13.1 Bq.kg^{-1}. The world average values of activity concentration of ^{238}U, ^{232}Th and ^{40}K in soil are 33 Bq.kg^{-1}, 45 Bq.kg^{-1} and 412 Bq.kg^{-1}, respectively [14]. Table-2 shows that ^{238}U was found to be within the world average value at few places, for example, North Halishahar, Patenga Sea Beach, Parki Sea Beach, Moheshkhali Island and Himchari Sea Beach, Cox's Bazar. In all other places ^{238}U was found to be on an average 1.6 times higher than the world average value. The radionuclide ^{232}Th was found to be on an average 1.9 times higher than the world average value. ^{40}K was found to vary from 201.0±14.2 Bq.kg^{-1} to 1460.8±38.2 Bq.kg^{-1}.

Although there was no nuclear accident in Bangladesh, observation of anthropogenic radionuclide ^{137}Cs was reported in small amount at different places due to stratospheric fallout [8, 9]. However, this fission fragment was not found anywhere in this study.

Due to the radionuclides in the sediment of the Bay of Bengal, the outdoor absorbed dose rate was found to be in the range from 69±9 $nGy.h^{-1}$ to 150±13 $nGy.h^{-1}$ with an average of 92±10 $nGy.h^{-1}$ which is higher than the world average value 58 $nGy.h^{-1}$ [13]. The annual effective dose was assessed to be in the range of 0.08±0.01 – 0.18±0.02 mSv with an average of 0.11±0.01 mSv; this value is also higher than the world average value of 0.07 mSv. The radium equivalent activity was found to be in the range of 150.2±0.01 – 318.4±28.2 $Bq.kg^{-1}$ with an average of 206.2±23.2 $Bq.kg^{-1}$; this average is less than the maximum limit of 370 $Bq.kg^{-1}$ as recommended by OECD [16].

Table 3: Different radiological hazard parameters

Location	Radiological Hazard Parameters		
	D ($nGy.h^{-1}$)	**H ($mSv.a^{-1}$)**	**Ra_{eq} ($Bq.kg^{-1}$)**
Sandwip Ship Ghat, Kumira, Sitakunda	82.0±10.0	0.10±0.01	180.4±22.5
Bhatiari, Chittagong	90.6±10.6	0.11±0.01	199.1±23.9
North Salimpur, Chittagong	90.8±10.6	0.11±0.01	200.1±23.8
Ananda Bazar Beach, North Halishahar, Chittagong	79.0±9.1	0.10±0.01	169.3±20.5
Khejurtola Beach, Katgar, Chittagong	89.0±10.6	0.11±0.01	197.2±23.9
Golden Beach, Katgar, Chittagong	109.2±11.8	0.13±0.01	246.0±26.8
Patenga Sea Beach, Chittagong	88.0±9.5	0.11±0.01	188.5±21.5
Parki Sea Beach, Anwara	68.9±8.9	0.08±0.01	150.2±20.1
North Bahar Chara, Banshkhali	120.3±11.3	0.15±0.01	257.7±25.5
Northern side of Kutubdia Island, Cox's Bazar	150.3±12.6	0.18±0.02	318.4±28.2
Southern side of Kutubdia Island, Cox's Bazar	123.8±12.6	0.15±0.02	275.9±28.5
Soadia Island, Moheskhali, Cox's Bazar	71.2±8.6	0.09±0.01	153.0±19.5
Laboni Sea Beach, Cox's Bazar	84.4±10.6	0.10±0.01	190.4±24.2
Himchari Sea Beach, Cox's Bazar	78.7±9.3	0.10±0.01	173.5±21.0
Inani Sea Beach, Cox's Bazar	115.2±12.3	0.14±0.02	259.8±28.0
Teknaf Sea Beach, Teknaf	217.9±17.1	0.27±0.02	498.5±39.1
Dakhinpara, Teknaf	93.2±10.7	0.11±0.01	205.7±24.2
Average⁎	**91.6±10.3**	**0.11±0.01**	**206.2±23.2**

⁎Values observed at Teknaf Sea Beach are not considered in the average.

4. CONCLUSIONS

Distribution of radionuclides in sediments of the coastal region of the Bay of Bengal from Sitakunda, Chittagong to Teknaf, Cox's Bazar was measured using gamma spectroscopy. The average activity concentration of ^{238}U, ^{232}Th and ^{40}K in the sediments were found to be 43±6 Bq.kg^{-1}, 83±11 Bq.kg^{-1}, and 449±21 Bq.kg^{-1}, respectively. Shatkhira district in Khulna division is located in the other part of the coastal area of the Bay of Bengal as shown in the Figure-1. Concentration of ^{238}U and ^{232}Th in soil and sediment of Shatkhira were found to be 44±3 Bq.kg^{-1} and 92±8 Bq.kg^{-1}, respectively [17]. So, our measurement on ^{238}U and ^{232}Th are in close agreement with the values observed in Shatkhira. These observations lead to the conclusion that the costal region of the Bay of Bengal is rich in ^{238}U and ^{232}Th.

Ratio of activity concentration of ^{232}Th to that of ^{238}U was found here to be in the range 1.33 - 2.72 with an average 1.95. This ratio is observed to be 1.82 in the sediments of the Karnaphuli River [18]; this river has its estuary with the Bay of Bengal. In another study on the Sitakunda coastal region of the Bay of Bengal, this ratio was found to be 1.99 [19]. So, it can be said that the ratio of ^{232}Th to ^{238}U in the sediments of the Bay of Bengal is around 2. The coastal region of the Bay of Bengal is rich in different thorium minerals such as monazite, thorite and zircon.

Due to higher concentration of ^{238}U and ^{232}Th in sediment, the coastal region of the Bay of Bengal has a greater risk of radiological hazard. However, the radium equivalent activity is within the allowable limit (≤370 Bq.kg^{-1}). So, the sediment of the Bay of Bengal is safe for the aquatic animals. Both the radionuclide ^{238}U and ^{232}Th were observed in higher concentration in the Teknaf sea beach area than the other places. Further study is needed to know the reason.

The radionuclide ^{137}Cs is an important marker of anthropogenic radiological contamination due to nuclear fall-out. This nuclide was not observed in the coastal region of the Bay of Bengal from Sitakunda, Chittagong to Taknaf, Cox's Bazar.

5. ACKNOWLEDGEMENT

Authors are grateful to Bangladesh Atomic Energy Commission, Bangladesh for giving the permission to use the Gamma Spectroscopy system for this study.

REFERENCES

[1] IAEA update Log on Fukushima Nuclear Accident https://www.iaea.org/newscenter/news/fukushima-nuclear-accident-update-log-12

[2] UNSCEAR Report 2013 http://www.unscear.org/docs/reports/2013/13-85418_Report_2013_Annex_A.pdf

[3] UNSCEAR Report 2000 http://www.unscear.org/docs/publications/2000/UNSCEAR_2000_Annex-B.pdf

[4] M Abbaspour, F Moattar, A Okhovatian and M Kharrat Sadeghi *Radiat Prot Dosimetry* **142**, 265, (2010).

[5] B Baggoura, A Noureddine and M Benkrid *Appl Radiat Isot* **49**, 867, (1998).

[6] V Kannan, M P Rajana, M A R Iyengara and R Ramesh *Appl Radiat Isot* **57,** 109, (2002).

[7] G Karahan and A Bayulken *J Environ Radioact* **47**, 213, (2000).

[8] F K Miah, S Roy, M Touhiduzzaman and B Alam *Appl Radiat Isot* **49**, 133, (1998).

[9] Q M Rashed-Nizam, M M Rahman, M Kamal and M I Chowdhury *J Radiat Res* **56**, 22, (2015).

[10] S N A Tahir, K Jamil, J H Zaidi, M Arif, N Ahmed and S A Ahmad *Radiat Prot Dosimetry* **113**, 421, (2005).

[11] Banglpedia Chittagong Region River System http://en.banglapedia.org/index.php?title=Chittagong_Region_River_System; retrieved on 02 November, 2017

[12] IAEA *Technical Report Series* **295** (1989).

[13] B Marie-Martine, V Chiste and C Dulieu, Rapport CEA-R-6201:Nucleide-LARA 2008 http://www.nucleide.org/DDEP_WG/Nucleide-LARA_2008.pdf

[14] UNSCEAR Report 2008 http://www.unscear.org/docs/reports/2008/09-86753_Report_2008_Annex _B.pdf

[15] J Beretka and P J Mathew *Health Phy* **48**, 87, (1985).

[16] OECD Report 1979 https://www.oecd-nea.org/rp/reports/1979/exposure-to-radiation-1979.pdf

[17] M I Chowdhury, M Kamal, M N Alam, S Yeasmin and M N Mostafa *Radiat Prot Dosimetry* **118**, 126, (2006).

[18] M I Chowdhury, M N Alam and S K S Hazari *Appl Radiat Isot* **51**, 747, (1999).

[19] M M Rahman, A T Islam, M Kamal and M I Chowdhury *Sc. J Phy* doi:10.7237/sjp/211 (2012**).**

*Bangladesh Journal of Physics, **23 & 24**, 9-21, 2018*

$Ni_{0.5}Cu_{0.5}Fe_2O_4$/DDA-MMT COMPOSITES: SYNTHESIS, STRUCTURAL, MAGNETIC AND ELECTRICAL PROPERTIES

K. HOQUE[1,4], T. C. PAUL[1], D. K. SAHA[2], S. ISLAM[3], N. KHATUN[3] AND P. BALA[1*]

[1]*Department of Physics, Jagannath University, Dhaka – 1100*
[2]*Atomic Energy Commission, Agargaon, Dhaka – 1207*
[3]*Industrial Physics Division, BCSIR Laboratories, BCSIR, Dhaka-1205*
[4]*Physics Discipline, Khulna University, Khulna - 9208*

** Corresponding author: E-mail: balaparimal@gmail.com*

Received on 18.04.2018, Revised received on 02.068.2018, Accepted for publication on 27.06.2018

ABSTRACT

1 wt% and 5 wt% dodecylalkylammonium montmorillonite (DDA-MMT) supported $Ni_{0.5}Cu_{O.5}Fe_2O_4$ (Ni-Cu ferrite) composites were synthesized by double sintering method. The structural and microstructural characterizations of the samples were performed using X-ray diffraction (XRD) and scanning electron microscopic (SEM) techniques. Magnetic, dielectric and electrical properties of the samples were investigated. Both naked and DDA-MMT supported Ni.Cu ferrites were found to be cubic spinel structure. The values of lattice parameter, crystallite size and porosity of naked Ni-Cu ferrite we recalculated to be 8.365Å, 29 nm and 25% respectively. The lattice parameter of1wt% DDA-MMT supported Ni–Cu ferrite was found to be 8.361Åand an increase in crystallite size was observed. The porosity of Ni-Cu ferrite supported with 1wt% and 5wt% DDA-MMT were found to be 29% and 38% respectively. The lower value of saturation magnetization was observed for DDA-MMT supported Ni-Cu ferrites compare to that of naked Ni-Cu ferrite. The Curie temperature of 1wt% DDA-MMT supported Ni-Cu ferrite was very close to that of naked Ni-Cu ferrite and decreased significantly for5wt% DDA-MMT supported composite. The electrical conductivities were found to be greater in 5 wt% DDA-MMT supported Ni-Cu ferrites than the naked Ni-Cu ferrite. It appears that DDA-MMT acts as a matrix material and influences the crystallization, aggregation, magnetic ordering and transport properties of Ni-Cu ferrite particles which eventually be useful for tailoring and diversify their applications.

1. INTRODUCTION

Montmorillonite (MMT), a 2:1 type of layer structure clay mineral, comprised of negatively charged silica sheets held together by charge-balancing counterions such asMg^{2+}, Na^{+}, and Ca^{2+}. The general chemical formula of the montmorillonite is $(M_y^{+}.nH_2O)(Al_4\text{-}yMg_y)Si_8O_{20}(OH)_4$, where M (M = Na^{+}, Ca^{2+}, Mg^{2+}, etc.) is the interlayer cation. These interlayer cations balance the negative charges which are generated by the isomorphous substitution of Mg^{2+} and Fe^{2+} for Al^{3+} in the octahedral sheet; and Al^{3+} for Si^{4+} in the tetrahedral sheet[1].Montmorillonite possesses interesting structural features such as – the thickness of MMT layers is around 1 nm[2]; can be organically modified easily by ion exchange reaction [3]; individual MMT layers can be exfoliated into other materials [4]; MMT layers contain negative charges bound with interlayer cations and water molecules [1]. Exploiting these interesting structural features, montmorillonite and their

organomodified form have been used in different areas such as thickeners in paints, greases, oil-base drilling muds, purpose of gelling various organic liquids, catalysts, polymer clay nanocomposites [5-7].

Magnetic nanoparticles possess large specific surface area, much higher surface energy and reduced magnetic anisotropy energy [8]. Due to these interesting properties, magnetic nanoparticles (MNP) have wide practical applications in different areas including magnetic storage media [9], catalysis [10], ferrofluid [11], environmental remediation [12], drug and gene delivery system [13], cell separation [14], and magnetic resonance imaging (MRI) [15]. However, naked MNPs have some limitations since the aggregation of naked MNP is practically unavoidable due to their high surface energy, van derWaals force and the dipole-dipolemagnetic attraction among particles [16, 17]. Again, naked MNP is at the high risk of oxidation [18, 19], acid/basic erosion [20] and the release of metal ions [21]. In order to address these issues, a typical method is to use matrix materials to isolate, accommodate and stabilize individual MNP is of great interest [22, 17]. The widely used matrixmaterials include graphene [23, 24], active carbon [25], carbon nanotubes [26], silica [27, 28], clay minerals [29, 30], polymers [31, 32], ionic liquids [33, 34], starch [35], and even collagen gels [36]. However, using two-dimensional layered materials as the matrices to isolate, accommodate and stabilized individual magnetic nanoparticles have some advantages due to their high specific surface area, intercalating, pillaring, supporting, and encapsulating properties [8]. Among the variety of two-dimensional layered materials, naturally occurring gmontmorillonite have much distinct 2D sheet-like structure with interesting physicochemical properties[37]. The interlayer spaces, surfaces and edges of montmorillonite minerals provide potential sites to host, stabilize and tune MNP[12, 38]. Thus, the synthesis and characterizations of montmorillonite supported magnetic nanoparticles are of great interest for many researchers such as Peng et al. have studied $LaFeO_3$/MMT composite synthesized by assembling $LaFeO_3$ nanoparticles on the surface of montmorillonite sheets [39], Mulewa et al. have studied MMT-supported Ni/TiO_2naocomposite [40],Son et al. have investigated α-Fe_2O_3/Na-MMT[30]composite, Bartonkova have investigated Fe_3O_4/MMTT [29], Ai et al. have studied$CoFe_2O_4$/MMT composite [41], Hashemian has investigated $MnFe_2O_4$/MMT composite [42].However, most of the studies mainly deal with the application of pure montmorillonite as the supporting matrix material for magnetic nano-particles. But organomodified montmorillonite synthesized by intercalating of organic species into the interlayer spaces of Na-montmorillonite provide expanded basal spacing, greater exfoliation capabilities and organophilic natureseems to be an interesting matrix material for magnetic nanoparticles. Thus,an attempt has been made to synthesis and characterizes organo modified clay supported ferrite composites.More specially, synthesis of $Ni_{0.5}Cu_{0.5}Fe_2O_4$/MMT composite using an organo-clay termed as dodecylalkylammonium montmorillonite (DDA-MMT)synthesized by intercalating dodecylalkylammonum into the inter layer spaces of Na-montmorillonite has been addressed in the present investigation. Structural and microstructural characterizations of synthesized $Ni_{0.5}Cu_{0.5}Fe_2O_4$/MMT composite along with naked $Ni_{0.5}Cu_{0.5}Fe_2O_4$ have been performed using X-ray diffraction (XRD) and scanning electron microscopic (SEM) techniques. Magnetic properties such as Curie temperature, saturation magnetization, remanent magnetization, coercive field and permeability of the samples have also been investigated. Variation of DC conductivity with temperature and AC conductivity with frequency and dielectric constant of the $Ni_{0.5}Cu_{0.5}Fe_2O_4$/MMT and $Ni_{0.5}Cu_{0.5}Fe_2O_4$/MMT have also been performed.

2. EXPERIMENTAL

Samples of the Ni-Cu ferrites having the chemical formula $Ni_{0.5}Cu_{0.5}Fe_2O_4$were prepared by the standard double sintering ceramic technique using high purity oxides of CuO, NiO and Fe_2O_3. The reagent powders were weighed precisely according to their molecular weight. The oxides were thoroughly mixed in an agate mortar, heat-treated and compacted in the form of pellets and toroid. During this preparation, pre-sintering at 800°C for 3hours and powdering of the formed products was followed by final sintering at 1000°C for 6hours.Dodecylalkylammonium intercalated montmorillonite (DDA-MMT) where synthesized from Na-montmorillonite (SWy-2, CEC = 74.6 meq per 100 gm) supplied by Purdue University, USA and octadecyl amine collected from E-mark, Germany by ion exchange reaction. The details method of synthesis of DDA-MMT and their characterization has been reported elsewhere [3].In order to synthesis of $Ni_{0.5}Cu_{0.5}Fe_2O_4$/DDA-MMT composite required amount of CuO, NiO and Fe_2O_3were taken and pre-sintered at 800°C and after this stage 1wt% and 5wt% of DDA-MMT were added separately and milled 12 hours and sintered at 1000°C and desired products were obtained. We named $Ni_{0.5}Cu_{0.5}Fe_2O_4$supported with 1 and 5 wt% of DDA-MMT as $Ni_{0.5}Cu_{0.5}Fe_2O_4$/DDA-MMT (1 wt%)and $Ni_{0.5}Cu_{0.5}Fe_2O_4$/DDA-MMT (5wt%) respectively. XRD intensities of the compounds were recorded with a Philips X'Pert Pro X-ray Diffractometer (PW3040) in the Material Science Division, Atomic Energy Center Dhaka using monochromatic CuKα (λ =1.542Å) radiation. Nickel filter was used to suppress the unexpected radiations. The tube was operated at 60 kV and about 40 mA. X-ray intensities for all the samples were recorded for the range of 2θ, 15° to 75°. The step size for X-ray recording was 0.02°. In order to calculate the value of basal spacing, full width at half maximum and crystallite size, the background correction of the intensity profile was made. Powder diffraction data were analyzed using the software X'Pert High score. The Magneta Pulse Field Hysteresis Loop Tracer instrument was used for the M-H loop tracing. Curie temperature measurement was done by using Wayne Kerr Inductance Analyzer 6500B. DC resistivity of ferrites samples has been measured as a function temperature in the range from room temperature up to 300^{O}C using Keithley 6514 system electrometer. AC resistivity of ferrites samples has been measured as function of frequency in the average of 10 kHz to10^4 kHz at room temperature by Wayne Kerr Inductance Analyzer 3255B.Dielectric constant of the samples has been measured over a frequency range 250 kHz to 5×10^4 kHz.

3. RESULTS AND DISCUSSION

3.1 X-ray diffraction analysis

X-ray diffraction profiles of$Ni_{0.5}Cu_{0.5}Fe_2O_4$, $Ni_{0.5}Cu_{0.}Fe_2O_4$/DDA-MMT (1wt%) and $Ni_{0.5}Cu_{0.5}Fe_2O_4$/DDA-MMT (5wt%) have been presented in figure 1.It is observed from figure 1 that DDA-MMT supported and naked Ni-Cu ferrite showedeight reflections from the planes of (111), (220), (311), (222), (400), (422), (511) and (440) correspond to the cubic spinel phases[43]. It is also observed that peaks of DDA-MMT supported Ni-Cu ferrite are well matched with that of naked Ni-Cu ferrite indicating absence of any intermediate phase in DDA-MMT supported Ni-Cu ferrite. The values of lattice constant obtained in the present investigated have been tabulated in the table 1. It is observed that lattice parameter of 1wt% DDA-MMT supported Ni-Cu ferrite is very close to that of naked Ni-Cu ferrite and lattice parameter of 5wt% DDA-MMT supported Ni-Cu ferrite increases slightly with respect to naked Ni-Cu ferrite. The montmorillonite layer contains Mg^{2+}, Al^{3+} and Si^{4+}ions and may have the possibility to leave the MMT layers of these

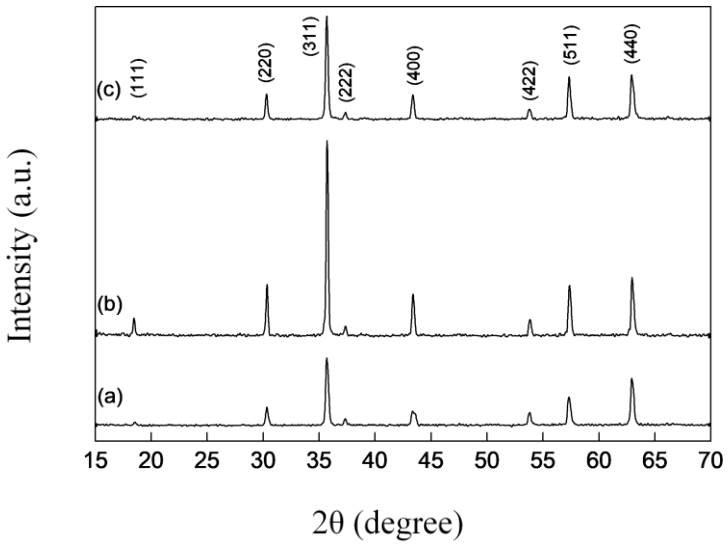

Fig. 1. X-ray diffraction profiles of (a) $Ni_{0.5}Cu_{0.5}Fe_2O_4$, (b) $Ni_{0.5}Cu_{0.}Fe_2O_4$/DDA-MMT (1 wt%) and (c) $Ni_{0.5}Cu_{0.5}Fe_2O_4$/DDA-MMT (5 wt%).

ions to some extent at the sintering temperature [1]. It appears that the concentration of these ions become more in 5 wt% DDA-MMT supported compound and some short of ionic migration between ferrite structure and the ions of MMT layers takes place which may be responsible for greater value in lattice constant for this compound. The values of X-ray density, bulk density and porosity of the naked Ni-Cu ferrite and supported with the addition of 1wt% and 5wt% DDA-MMT have been presented in table 1. It is observed from the table that bulk density decreases with the increase of DDA-MMT content in Ni-Cu ferrite. The density of DDA-MMT is lower with compare to Ni-Cu ferrite. Thus, it is expected that addition of DDA-MMT will decrease the bulk density of Ni-Cu ferrite. It is observed that X-ray density increases with the increase of percentage of DDA-MMT loading in the Ni-Cu ferrite. The porosity of the naked $Ni_{0.5}Cu_{0.5}Fe_2O_4$ was found to be 25% and that of the supported with the addition of 1% and 5% DDA-MMT was 29% and 38% respectively. DDA-MMT contains dodecyl ammonium into the interlayer spaces of montmorillonite. These interlayer species were usually expulsed by evaporation in the temperature range 300°C – 450°C [3]. It seems that in the present investigation these interlayer species removed during sintering process which finally makes the modified ferrite more porous. The crystallite size calculated from (311) reflection using Scherrer equation has been presented in the table 1. The value of crystallite size is greater in 1 wt% DDA-MMT supported Ni-Cu ferrite. Again, 5 wt% DDA-MMT supported Ni-Cu ferrite shows lower values of crystallite size with compare to 1 wt% DDA-MMT supported composite. It appears that DDA-MMT content plays an important role in crystallization of Ni-Cu ferrite especially for small amount of DDA-MMT content (1 wt%). However, increase of DDA-MMT content (5 wt%) hindered the crystallization. Similar types of results are also obtained by Wang et al. for CeO_2/Montmorillonite composite[44].

Table 1: Lattice parameter, crystallite size, bulk density, X-ray density and porosity of DDA-MMT supported and naked $Ni_{0.5}Cu_{0.5}Fe_2O_4$

Sample	Lattice Parameter (Å)	Crystallite size (Å)	Bulk Density (gm/cm^3)	X-ray Density (gm/cm^3)	Porosity (%)
$Ni_{0.5}Cu_{0.5}Fe_2O_4$	8.365	29	4.04	5.37	25
$Ni_{0.5}Cu_{0.5}Fe_2O_4$/DDA-MMT (1 wt%)	8.361	41	3.84	5.40	29
$Ni_{0.5}Cu_{0.5}Fe_2O_4$/DDA-MMT (5 wt%)	8.409	34	3.46	5.59	38

3.2 Scanning electron microscopic analysis

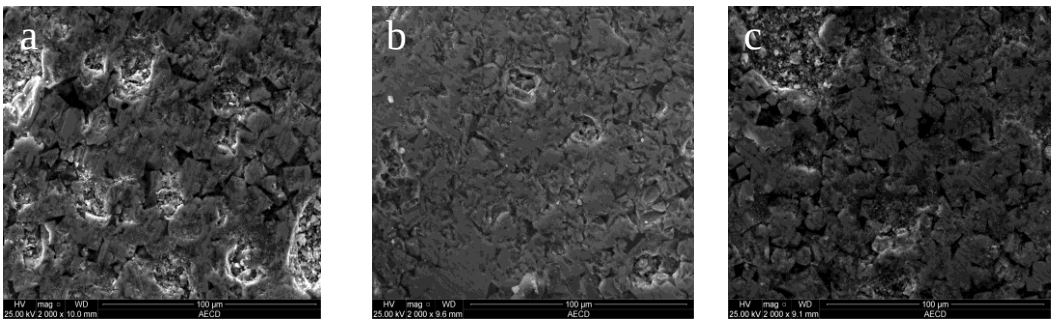

Fig. 2. SEM of (a) $Ni_{0.5}Cu_{0.5}Fe_2O_4$, (b) $Ni_{0.5}Cu_{0.}Fe_2O_4$ + 1% DDA-MMT and (c) $Ni_{0.5}Cu_{0.5}Fe_2O_4$ + 5% DDA-MMT.

Figure 2 represents SEM micrographs of naked and 1 and 5 wt% of DDA-MMT supported Ni-Cu ferrite. The micrographs explore that the grains are developed with grain boundaries and separated by pores in naked Ni-Cu ferrite. The agglomerations may be happened due to the relatively high annealing temperature and interaction between magnetic particles[45]. It is also observed from the figure that the grain size decreases for DDA-MMT supported Ni-Cu ferrite with compare to naked Ni-Cu ferrite. Again, grain boundaries are not clear in DDA-MMT supported Ni-Cu ferrites. The variation in grain size of DDA-MMT supported Ni-Cu ferrite infers that MMT layers played the role of matrix material and influences the agglomeration properties.

3.3 Magnetic properties

Figure 3 represents the M - H curve of $Ni_{0.5}Cu_{0.5}Fe_2O_4$, $Ni_{0.5}Cu_{0.5}Fe_2O_4$/DDA-MMT (1 wt%)and $Ni_{0.5}Cu_{0.5}Fe_2O_4$/DDA-MMT (5wt%) composites. The value of saturation magnetization (M_s), remanent magnetization (M_r) and coercive field (H_c) for DDA-MMT incorporated $Ni_{0.5}Cu_{0.5}$ Fe_2O_4 have been determined at room temperature and are tabulated in table 2. The value of saturation magnetization is found to be 41.7 emu g^{-1} for $Ni_{0.5}Cu_{0.5}Fe_2O_4$. Wang et al. prepared Ni-Cu ferrite by auto-combustion method and sintered at 600°C and the saturated magnetization (M_s) value of the sample was found to be 39.3 emu g^{-1}[46]. Patil and Chougule[45]synthesized $Ni_{1-x}Cu_xFe_2O_4$

sample through conventional mixed oxides method and observed that the M_s increased with increasing the Cu content and the M_s value was around 39emu g^{-1} when the Cu content was 0.2.The value of saturation magnetization obtained in the present investigation are in good agreement with the results obtained by Wang et al. [46], and Patil and Chougule[45].It is observed from the table 2 that saturation magnetization decreases with increase of DDA-MMT loading in $Ni_{0.5}Cu_{0.5}Fe_2O_4$. Usually, the value of saturation magnetization of magnetic nano particle/clay minerals (MNP/CM) nanocomposites are observed to be lower than that of individual MNP or bulk materials[8].

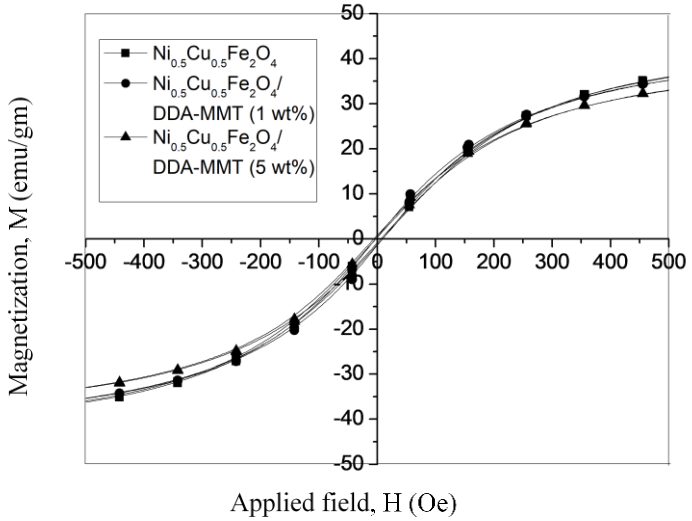

Fig. 3. Variation of magnetization with applied magnetic field (a) $Ni_{0.5}Cu_{0.5}Fe_2O_4$, (b) $Ni_{0.5}Cu_{0.}Fe_2O_4$ /DDA-MMT (1 wt%) and (c) $Ni_{0.5}Cu_{0.5}Fe_2O_4$ /DDA-MMT (5 wt%).

Table 2: Saturation magnetization (M_s), coercive field (H_c) and remanence magnetization (M_r) of DDA-MMT supported and naked $Ni_{0.5}Cu_{0.5}Fe_2O_4$.

Sample	Saturation magnetization (emu g^{-1})	Coercive field (Oe)	Remanence magnetization (emu g^{-1})
$Ni_{0.5}Cu_{0.5}Fe_2O_4$	41.7	5.4	0.89
$Ni_{0.5}Cu_{0.5}Fe_2O_4$/DDA-MMT (1 wt%)	41.1	5.1	0.94
$Ni_{0.5}Cu_{0.5}Fe_2O_4$/DDA-MMT (5 wt%)	39.1	5.9	0.97

The formation and growth of embedded magnetic particles in MNP/CM nanocomposites are mechanically and spatially constrained by the clay mineral layers. Magnetic orders are easily randomized in these embedded particles and the observed M_s of MNP are smaller than bulk magnetic materials[47-49].In addition, the anisotropy is enhanced[50, 51] due to lower grain size of MNP in MNP/CP nanocomposite leads to the reduction of M_s[8]. In the present investigation, the presence of montmorillonite layers as matrix material in the Ni-Cu ferrite lowers the grain size of DDA-MMT supported Ni-Cu ferrite as observed by SEM analysis. It infers that this smaller grain size makes a suitable environment for the randomization of magnetic order and becomes responsible for lowering the values of saturation magnetization. It is observed from the table 2 that the remanent magnetization and coercive field increases with the increase of DDA-MMT content in Ni – Cu ferrite. The increase of remanent magnetization with increase of DDA-MMT content in Ni – Cu ferrite indicates that it goes to soft magnetic to hard magnetic material and the increase of coercive field with increasing DDA-MMT concentration means the magnet becomes durable magnet with increasing concentration.

The variation of normalized magnetic initial permeability with temperature for all the samples is shown in figure 4. It is evident from figure that the magnetic initial permeability remains nearly constant over a wide range of temperature showing good thermal stability. It can be noted from figure 4 that as the temperature increases the magnetic initial permeability remains constant up to a certain temperature and increases to a peak value and then abruptly falls to a minimum value. The temperature at which this abrupt fall takes place is the magnetic Curie transition temperature (T_c). The Curie temperature obtained in the present investigation for naked and 1 wt % DDA-MMT, 5 wt% DDA-MMT supported Ni-Cu ferrite has found to be 415, 420 and 395°C respectively. It is observed that the Cuire temperature of the Ni-Cu ferrite supported with the addition of 1wt% DDA-MMT was found to be close to that of naked Ni-Cu ferrite whereas for the sample modified with 5wt% DDA-MMT is reasonably small (figure 4). The magnetic initial permeability for the material is expected to strongly depend on the microstructure, as the magnetic initial permeability represents the mobility of magnetic domain wall in response to the small applied field. It seems that in the present investigation that the mobility of magnetic domain wall is restricted by microstructure or presence of greater amount of MMT layers in 5 wt% DDA-MMT supported Ni-Cu ferrite.

The variation of initial permeability of naked Ni-Cu ferrite and that of supported with the addition of 1wt% and 5wt% of DDA-MMT as a function of frequency has been presented in figure 5. The initial permeability remains almost constant in the frequency range 500 Hz to 10^4 kHz as observed from the figure 5. It shows a decreasing trend with the increase of frequency onward the 10^4 kHz. It is interesting to note that the value of the initial permeability of Ni-Cu ferrite modified with the addition of 1 wt% DDA-MMT is observed to be lower and that of naked Ni-Cu ferrite and higher that of Ni-Cu ferrite modified with 5 wt% DDA-MMT. Almost constant value of initial permeability indicates good frequency stability of DDA-MMT supported Ni-Cu ferrite. It appears from the figure 5that frequency stability is little higher in case of DDA-MMT supported Ni-Cu ferrite. In general the variation in initial permeability is attributed to either domain wall displacement or domain rotation or both of these contributions. It seems that in the present investigation the motion of domain wall is influenced by the dispersion of MMT sheet and the defects present there in which finally become responsible for the variation in initial permeability. The XRD analysis indicates that DDA-MMT content influence the crystal growth of ferrite resulting variation in crystallite size. It appears that greater value in crystallite size for 1 wt%

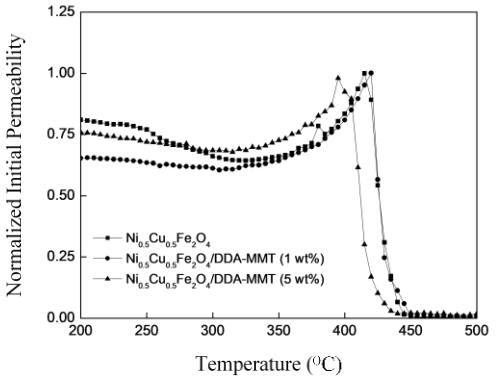

Fig. 4. Normalized initial permeability of $Ni_{0.5}Cu_{0.5}Fe_2O_4$, $Ni_{0.5}Cu_{0.}Fe_2O_4$ /DDA-MMT (1 wt%) and $Ni_{0.5}Cu_{0.5}Fe_2O_4$ /DDA-MMT (5 wt%) with temperature.

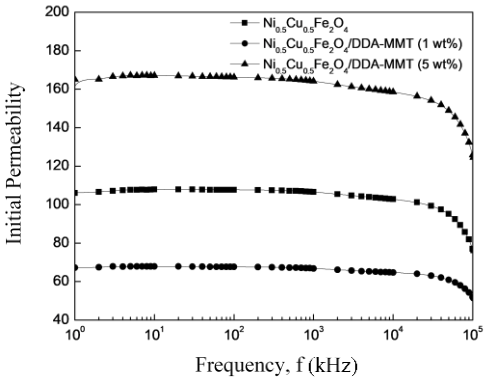

Fig. 5. Initial permeability of $Ni_{0.5}Cu_{0.5}Fe_2O_4$, $Ni_{0.5}Cu_{0.}Fe_2O_4$ /DDA-MMT (1 wt%) and $Ni_{0.5}Cu_{0.5}Fe_2O_4$ /DDA-MMT (5 wt%) with frequency.

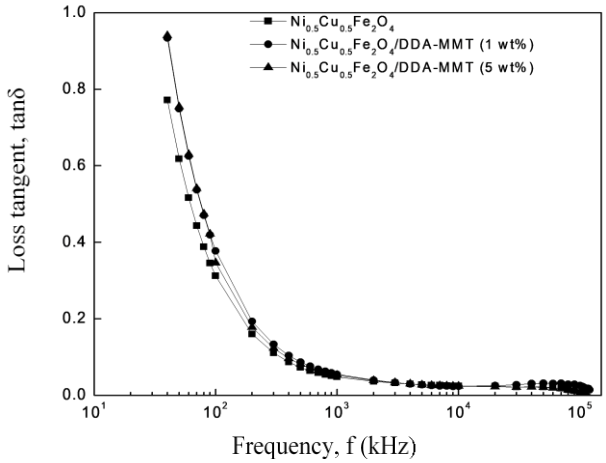

Fig. 6. Permeability loss (Loss tangent) of $Ni_{0.5}Cu_{0.5}Fe_2O_4$, $Ni_{0.5}Cu_{0.}Fe_2O_4$ /DDA-MMT (1 wt%) and (c) $Ni_{0.5}Cu_{0.5}Fe_2O_4$ /DDA-MMT (5 wt%) with frequency.

DDA-MMT supported ferrite compound creates favorable environment for easy magnetization hence shows a lower value in initial permeability. But when the DDA-MMT content increases the value of crystallite size decreases and porosity increases which makes situation harder to magnetize the material and shows higher values of initial permeability as observed in 5 wt% DDA-MMT supported ferrite compound. In general, the variation in initial permeability is attributed to either domain wall displacement or domain rotation or both of these contributions. It seems that in the present investigation the motion of domain wall is influenced by the dispersion of MMT sheet and the defects present therein which finally become responsible for the variation in initial permeability. The XRD analysis indicates that DDA-MMT content influence the crystal growth of ferrite resulting variation in crystallite size and porosity. It appears that the porosity of

DDA-MMT supported Ni-Cu ferrite increases with increase of DDA-MMT content makes situation harder to magnetize the material resulting a decrease in initial permeability is observed with increase of DDA-MMT content (figure 5). Figure 6 represents the variation loss tangent with frequency of DDA-MMT supported and naked Ni-Cu ferrite. It is observed from the figure 6 that loss tangent is higher at lower frequencies and decrease rapidly with increase of frequency becomes almost constant at the frequency around 10^3 kHz.

3.4 Electrical and dielectric properties

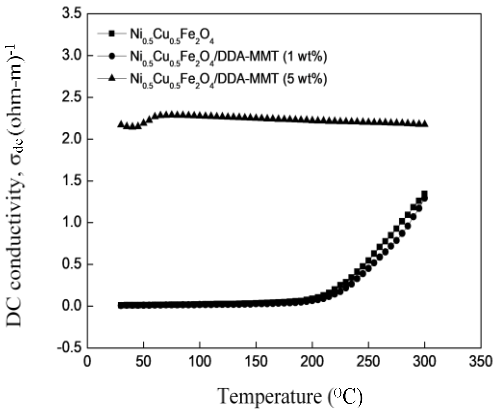

Fig. 7. DC conductivity of $Ni_{0.5}Cu_{0.5}Fe_2O_4$, $Ni_{0.5}Cu_{0.}Fe_2O_4$ /DDA-MMT (1 wt%) and $Ni_{0.5}Cu_{0.5}Fe_2O_4$ /DDA-MMT (5 wt%) with temperature.

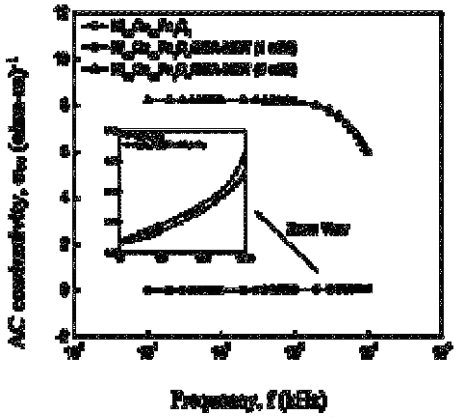

Fig. 8. AC conductivity of $Ni_{0.5}Cu_{0.5}Fe_2O_4$, $Ni_{0.5}Cu_{0.}Fe_2O_4$ /DDA-MMT (1 wt%) and $Ni_{0.5}Cu_{0.5}Fe_2O_4$ /DDA-MMT (5 wt%) with frequency.

The variation of DC conductivity with temperature of all the samples has been presented in figure 7. The DC conductivity of Ni-Cu ferrite supported with 1 wt% DDA-MMT shows almost similar nature with naked ferrite. However, the DC conductivity is found to be higher in case of the Ni-Cu ferrite supported with 5 wt% DDA-MMT (figure 7). It is also observed that DC conductivity remains almost constant up to the temperature of 200°C for naked and 1 wt% DDA-MMT supported Ni-Cu ferrite. However, Ni-Cu ferrite supported with the addition of 5wt% DDA-MMT shows almost constant value of DC conductivity up to 300°C. DDA-MMT possesses negative layer charge at MMT layer which is balanced by the intercalated dodecyl ammonium[1]. The intercalated alkyl ammonium of montmorillonite usually decomposed and expulsed from the interlayer spaces in the temperature range 300°C to 450°C [3]. This expulsion of intercalated species increases the charge density in MMT layers. It appears in the present investigation that intercalated dodecyl alkyl ammonium of DDA-MMT decomposed during the process of sintering of DDA-MMT supported Ni-Cu ferrite and it becomes more significant for 5 wt% DDA-MMT supported compound which finally helps to increase the conductivity of this. Similar type of

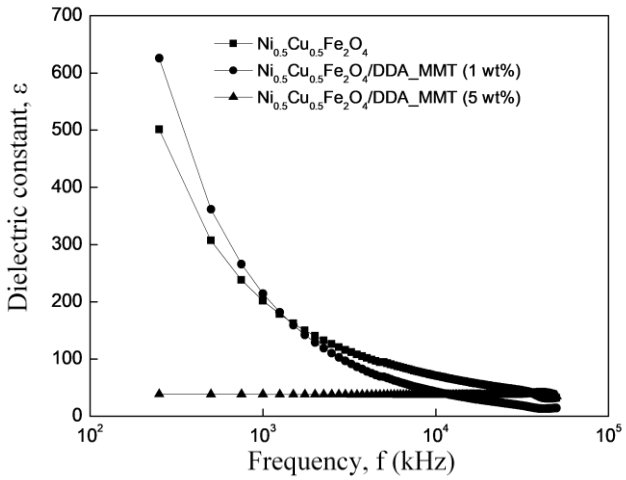

Fig. 9. Variation of dielectric constant of $Ni_{0.5}Cu_{0.5}Fe_2O_4$, $Ni_{0.5}Cu_{0.}Fe_2O_4$ /DDA-MMT (1 wt%) and (c) $Ni_{0.5}Cu_{0.5}Fe_2O_4$ /DDA-MMT (5 wt%) with frequency.

observations also made for Ni-Cu ferrite and multiwall carbon nanotube composite[46].However, some other factors such as porosity, degree of level of dispersion of individual layers of montmorillonite, nature of agglomeration of ferrite particles are also expected to play important role in the electrical transport properties. Figure 8 shows the variation of AC conductivity with frequency of naked Ni-Cu ferrite and supported with the addition of 1wt% and 5wt% DDA-MMT at the temperature of 30°C. It is observed from the figure 8 that the AC conductivity remains almost constant up to the frequency of 10^3 kHz for Ni-Cu ferrite supported with 5 wt% DDA-MMT. However, the AC conductivity was observed to be higher for the ferrite supported with the addition of 5 wt% DDA-MMT. The study on AC conductivity reveals the stability of the compound up to the frequency range 10^3 kHz. In order to clear understanding the variation of AC conductivity with frequency and DC conductivity with temperature for higher amount of DDA-MMT supported compounds requires in depth investigation and expected to perform in future. The variation of dielectric constant of both modified and unmodified Ni-Cu ferrite has been presented in figure 9. Itis observed from the figure that the dielectric constant decreases with increase of frequency and reaches a constant value at higher frequencies. This type of variation in dielectric constant with frequency is observed for other ferrite materials as well [52]. It is also observed that 1wt% DDA-MMT modified Ni-Cu shows higher values of dielectric constant at lower frequencies with respect to naked ferrite. The increase of dielectric constant of 1 wt% DDA-MMT supported Ni-Cu ferrite composites is consistent with the value obtained in Ni-Cu ferrite and MWCNTs composites [46]. The decrease in the dielectric constant with increase of frequency is the normal behavior for ferrites and can be explained on the basis of decreases in polarization with the increase in frequency. It is well known that, polarization of a dielectric material is the sum of the contribution of dipolar, electronic, ionic and interfacial polarizations. At low frequencies, all the polarizations respond easily to the time varying electric field but as the frequency of the electric field increases different polarization contributions filter out, as a result, the net polarization of the material decreases which leads to the decrease in the value of dielectric constant. The dielectric

properties of Ni-Cu ferrite supported with other matrix materials depend on the characteristics of the matrix, the property and volume fraction of the filler, the internal structure and the frequency of the electromagnetic waves[53].The variation of dielectric constant in case of DDA-MMT modified Ni-Cu ferrite may be related to the layer charges of montmorillonite, their polarizations and the interactions of MMT sheet with the ferrite structure. However, precise modeling of variation of dielectric constant with variation of DDA-MMT content in ferrite need in depth investigation.

4. CONCLUSIONS

Ni – Cu ferrites supported with dodecyl alkyl ammonium intercalated montmorillonite have been synthesized with the addition of 1wt% and 5wt% DDA-MMT content before the second sintering stage of ferrite synthesis process. Both naked and DDA-MMT supported Ni – Cu ferrites were observed to be single-phase cubic spinel structure as indicated by XRD analysis. The lattice parameters obtained for DDA-MMT supported Ni-Cu ferrites suggest some sort of ionic migration between ferrite structure and montmorillonite layers. The crystallization behavior of Ni-Cu ferrite is found to be influenced by the montmorillonite layers of DDA-MMT. The porosity of Ni-Cu ferrite is increased and less agglomeration of ferrite particles is observed when supported with DDA-MMT. The saturation magnetization and Curie temperature of 5 wt% DDA-MMT supported Ni-Cu ferrite is found to be lower than that of naked ferrite. The electrical conductivity is increased if Ni-Cu ferrite is supported with 5wt% DDA-MMT. The value of dielectric constant for 5 wt% DDA-MMT supported Ni-Cu ferrite is found to be deceased with compare to naked one. This investigation suggests that use of appropriate amount of DDA-MMT as matrix material in Ni-Cu ferrite could tailor its porosity, grain size, magnetic and electric properties which may diversify its applications.

REFERENCES

[1] P. Bala, B. K. Samantaray, S. K. Srivastava and H. Haeuseler, Zeit. Kristallogr. **215**, pp 235 (2000).

[2] M. Khajeh, S. Laurent and K. Dastafkan, Chem. Rev. **113**(10), pp 7728 (2013).

[3] P. Bala, B. K. Samantaray and S. K. Srivastava, Mater. Res. Bull. **35**, pp 1717 (2000).

[4] P. Bala, B. K. Samantaray, S. K. Srivastava and G. B. Nando, J. Appl. Polym. Sci. **92**, pp 3583 (2004).

[5] K. Yano, A. Usuki and A. Okada, J. Polym. Sci. Part A: Polym. Chem. **35**, pp 2289 (1997).

[6] R. A. Vaia and E. P. Giannelis, Macromolecules. **30**, pp 7990 (1997).

[7] D. S. Achilias, E. Panayotidou and I. Zuburtikudis, Thermochim. Acta. **514**, pp 58 (2011).

[8] L. Chen, C. H. Zhou, S. Fiore, D. S. Tong, H. Zhang, C. S. Li, S. F. Ji and W. H. Yu, Appl. Clay. Sci. **127–128**, pp 143 (2016).

[9] N. A. Frey, S. Peng, K. Cheng and S. H. Sun, Chem. Soc. Rev. **38**, pp 2532 (2009).

[10] K. C. F. Leung, S. H. Xuan, X. M. Zhu, D. W. Wang, C. P. Chak, S. F. Lee, W. K. W. Ho and B. C. T Chung, Chem. Soc. Rev. **41**, pp 1911 (2012).

[11] Y. Gao, J. P. Huang, Y. M. Liu, L. Gao, K. W. Yu and X. Zhang, Phys. Rev. Lett. **104**, pp 034501 (2010).

[12] R. K. Upadhyay, N. Soin and S. S. Roy, RSC Adv. **4**, pp 3823 (2014).

[13] I. Chourpa, L. Douziech-Eyrolles, L. Ngaboni-Okassa, J. F. Fouquenet, S. Cohen-Jonathan, M. Souce, H. Marchais and P. Dubois, Analyst. **130**, pp 1395 (2005).

[14] H. Xu, Z. P. Aguilar, L. Yang, M. Kuang, H. Duan, Y. Xiong and A. Wang, Biomaterials. **32**, pp 9758 (2011).

[15] A. K. Gupta and M. Gupta, Biomaterials. **26**, pp 3995 (2005).

[16] A. H. Lu, E. L. Salabas and F. Schüth, Angew. Chem. Int. Ed. **46**, pp 1222 (2007).

[17] D. Wang and D. Astruc, Chem. Rev. **114**, pp 6949 (2014).

[18] S. C. McBain, H. H. Yiu and J. Dobson, Int. J. Nanomedicine. **3**, pp 169 (2008).

[19] K. Kalantari, M. B. Ahmad, K. Shameli, M. Z. B. Hussein, R. Khandanlou and H. Khanehzaei, J. Nanomater. **2014**, pp 739485 (2014).

[20] A. G. Pershina, A. E. Sazonov and V. D. Filimonov, Russ. Chem. Rev. **83**, pp 299 (2014).

[21] N. Singh, G. Jenkins, R. Asadi and S. H. Doak, Nano. Rev. **1**, pp 5358 (2010).

[22] J. Liu, S. Z. Qiao, Q. H. Hu and G. Q. Lu, Small. **7**, pp 425 (2011).

[23] I. K. Herrmann, R. N. Grass and W. J. Stark, Nanomedicine. **4**, pp 787 (2009).

[24] T. Zeng, X. L. Zhang, Y. R. Ma, H. Y. Niu and Y. Q. Cai, J. Mater. Chem. **22**, pp 18658 (2012).

[25] S. Rudge, C. Peterson, C. Vessely, J. Koda, S. Stevens and L. Catterall, J. Control. Release. **74**, pp 335 (2001).

[26] S. Ko and J. Jang, Angew. Chem. Int. Edit. **45**, pp 7564 (2006).

[27] D. K. Yi, S. S. Lee and J. Y. Ying, Chem. Mater. **18**, pp 2459(2006).

[28] S. H. Hu, T. Y. Liu, H. Y. Huang, D. M. Liu and S. Y. Chen, Langmuir**. 24**, pp 239 (2008).

[29] H. Bartonkova, M. Mashlan, I. Medrik, D. Jancik and R. Zboril, Chem. Pap. **61**, pp 413 (2007).

[30] Y. H.Son, J. K. Lee, Y. Soong, D. Martello and M. Chyu, Chem. Mater. **22**, pp 2226 (2010).

[31] A. M. Derfus, G. von Maltzahn, T. J. Harris, T. Duza, K. S. Vecchio, E. Ruoslahti and S. N. Bhatia, Adv. Mater. **19**, pp 3932 (2007).

[32] R. B. N. Baig and R. S. Varma, Chem. Commun. **49**, pp 752 (2013).

[33] J. Y. Jung, J. B. Kim, A. Taher and M. J. Jin, Bull. Kor. Chem. Soc. **30**, pp 3082 (2009).

[34] Q. Zhang, H. Su, J. Luo and Y. Y. Wei, Green. Chem. **14**, pp 201 (2012a).

[35] A. S. Lubbe, C. Alexiou and C. Bergemanm, J. Surg. Res. **95**, pp 200 (2001).

[36] V. M. De Paoli, S. H. D. Lacerda, L. Spinu, B. Ingber, Z. Rosenzweig and N. Rosenzweig, Langmuir. **22**, pp 5894 (2006).

[37] F. Bergaya and G. Lagaly, Handbook of Clay Science. Developments in Clay Science, **5**. Elsevier.

[38] F. G. Liu, L. Z. Zhao, N. An, D. S. Tong, W. H. Yu and C. H. Zhou, J. Porous. Mater. **22**, pp 927 (2015).

[39] K. Peng, L. Fu, H. Yang and J. Ouyang, Sci. Rep. **6**, pp 19723 (2016).

[40] W. Mulewa, M. Tahir and N. A. S. Amin, Chem. Eng. J. **326**, pp 956 (2017).

[41] L. H. Ai, Y. Zhou and J. Jiang, Desalination. **266**, pp 72 (2011).

[42] S. Hashemian, Afr. J. Biotechnol. **9**, pp 8667 (2010).

[43] S. Anjum, A. Rashid, F. Bashir, S. Riaz, M. Pervaiz and R. Zia, IEEE. T. Magn. **50**, pp 2200504 (2014)

[44] A. Q. Wang, N. D'Souza and T. D. Golden, Appl. Clay. Sci. **42**, pp 310 (2008).

[45] D. R. Patil and B. K. Chougule, Mater. Chem. and Phy. **117**, pp 35 (2009).

[46] H. Wang, D. Zhu, W. Zhou and F. Luo, J. Mater. Sci.-Mater. El. **26**, pp 7698 (2015).

[47] J. I. Lai, K. V. P. M. Shafi, A. Ulman, K. Loos, Y. J. Lee, T. Vogt, W. L. Lee, and N. P. Ong, J. Phys. Chem. B. **109**, pp 15 (2005).

[48] W.D. Corner and P. A. Mundell, J. Magn. Magn. Mater. **20**, pp 148 (1980).

[49] R. H. Kodama, J. Magn. Magn. Mater. **200**, pp 359 (1999).

[50] F. Bødker, S. Mørup and S. Linderoth, Phys. Rev. Lett. 72, pp 282 (1994).

[51] M. Respaud, J. M. Broto, H. Rakoto, A. R. Fert, L. Thomas, B. Barbara, M. Verelst, E. Snoeck, P. Lecante, A. Mosset, J. Osuna, T. Ould Ely, C. Amiens and B. Chaudret, Phys. Rev. B. **57**, pp 2925 (1998).

[52] S. N. Rahman, S. Islam, N. Khatun, M. S. Hossain, Int. J. Inn. Tech.Expl. Eng. **3**(8), pp 48 (2014).

[53] J. Zhang, L. X. Wang and Q. T. Zhang, J. Mater. Sci.-Mater. El. **26**, pp 2538 (2015).

*Bangladesh Journal of Physics, **23 & 24**, 23-32, 2018*

DOSIMETRY OF FEW ^{60}Co TELETHERAPY UNITS USED FOR THE TREATMENT OF CANCER PATIENTS IN BANGLADESH

M. SHAMSUZZAMAN[1], MD. SHAKILUR RAHMAN[1*], M. MOSHARRAF HOSSAIN BHUIYAN[1], TANJIM SIDDIQUA[1], DEBASISH PAUL[1]AND RAKIBUL ISLAM[2]

[1]Secondary Standard Dosimetry Laboratory, Health Physics & Radioactive Waste Management Unit (HPRWMU), Institute of Nuclear Science and Technology (INST), Atomic Energy Research Establishment (AERE), Savar, Dhaka, Bangladesh

[2]Department of Physics, Khulna University, Khulna

** Corresponding author: E-mail: shakilurssdl@baec.gov.bd*

Received on 08.02.2018, Revised received on 08.06.2018, Accepted for publication on 08.07.2018

ABSTRACT

Dosimetric assessment of ^{60}Co teletherapy units employed for the treatment of cancer patients at various hospitals in Bangladesh has been performed applying International Atomic Energy Agency (IAEA) recommended protocol Technical Report Series-398 (TRS-398). In this perspective, determination of absorbed dose to water at 5 cm depth $D_w(Z_{ref})$ and the absorbed dose to water at the depth of dose maximum $D_w(Z_{max})$ was performed. The dosimetry system of Secondary Standard Dosimetry Laboratory (SSDL) was used in this study. The variation of $D_w(Z_{ref})$ and $D_w(Z_{max})$ with various field size(s) was investigated to check the linearity of dose variation with field size(s). The measured $D_w(Z_{ref})$ and $D_w(Z_{max})$ were compared with the calculated doses by the empirical relations. The % of deviation between the measured and estimated $D_w(Z_{ref})$ and $D_w(Z_{max})$ were found to be within the range of ±5% as recommended by ICRU in the case of dose deliver to the malignant tumor.

Keywords: Dosimetry, Teletherapy, Field size, Absorbed Dose to Water, Radiotherapy.

1. INTRODUCTION

In radiotherapy with Cobalt-60 (^{60}Co) teletherapy unit, ^{60}Co allows adequate dosing to the superficial tissues. Historically, great concern is expressed that 6-MV photons of linear accelerator (linac) have too large a buildup region and can potentially under dose superficial tissues [1]. In a developing country like Bangladesh, there is a strong prerequisite of radiotherapy units at the minimum costs and consistent quality. Generally, ^{60}Co modality needs low costs in comparison to advanced modern techniques (e.g. dual energy linac, linac with IMRT). In this perspective, some hospitals prefer treatment modality with ^{60}Co teletherapy machine. The additional advantage of ^{60}Co machine is its effectively constant output which reduces some of the uncertainties associated with the delivery of a specified dosage to the patient. Presently, there are about thirteen ^{60}Co teletherapy units available at the government and private hospitals in Bangladesh. Once a ^{06}Co teletherapy machine is accepted and hence placed for clinical service, it is essential to verify the standard output dose rate of ^{06}Co source in terms of D_{max} for the radiation treatment. In this regard, IAEA protocol TRS 398 was followed to conduct this dosimetric measurement. The accuracy of dose determination and dose delivery to the malignant tumor of cancer patient is a crucial issue for an effective outcome of radiation treatment. In the radiotherapy treatment procedure, recommended protocol needs to be followed so as to ensure the precision of delivered dose while

^{60}Co teletherapy machine is used. In developing countries, generally ^{60}Co teletherapy are widely used for the treatment of cancer patients. There are a good number of modeling studies that suggests that ^{60}Co may be more effective in modern radiation therapy than perceived in the past [2–4]. As good numbers of ^{60}Co teletherapy units are presently operational in different medical hospitals in all over Bangladesh, so output dose measurement of each unit is mandatory in every year as per IAEA recommendations [5] as well as nuclear safety and radiation control rules [6]. The basic principle of radiation therapy is to maximize the damage to the malignant cells and at the same time minimize the damage to the normal cells. This effectiveness of radiotherapy is generally accomplished by directing a radiation beam to the tumor from several directions so as to receive an optimized dose. It has been demonstrated that success of radiation treatment depends on the delivered absorbed dose to the tumor, provided that dose should not differ more than a few percent from the prescribed values. In this perspective, the International Commission on Radiation Units and Measurements (ICRU) recommends for an accuracy of ±5% [7]. A more complicated symptom may arise within the body of the patient, if the uncertainty of the dose delivered to the localized tumor is above 5% of that required. Moreover, healthy cells in the vicinity of the tumor may be affected due to the over exposure. On the other hand, a dose below 5% of the required one may not cure the patient satisfactorily. It is reported that therapeutic treatment with high standard accuracy of delivered dose is needed [8, 9]. Therefore, the overall uncertainties in radiation dosimetry need to be minimized so as to improve the accuracy in the determination of absorbed dose from the radiation beams used in the cancer therapy. In the present work an effort has been given to comparatively assess the output dose of four ^{60}Co teletherapy units of different hospitals in Bangladesh. The main purpose of this study is to verify whether the agreement between the experimental and calculated results is within ±5% variation. In addition, are presentative assessment of the wedge attenuation factors of two ^{60}Co units was performed since attenuation factors of various filters are essentially required to ensure the prescribed dose for the treatment of target organ. The work has been performed at National Institute of Cancer Research and Hospital (NICRH), Mymensingh Medical College Hospital (MMCH) and Dhaka Medical College and Hospital (DMCH) by using the standard dosimetric facility available at SSDL of Bangladesh Atomic Energy Commission.

2. MATERIALS AND METHODS

The dosimetric measurement of the ^{60}Co teletherapy machines were performed based on the dosimetry protocol TRS-398, published by the International Atomic Energy Agency (IAEA) [10]. In these measurements, a standard IAEA water phantom of dimension 30 cm × 30 cm × 30 cm was used for the absorbed dose to water D_w measurement of the ^{60}Co gamma beam. The dosimetry system consists of PTW Unidos electrometer-10005, S/N. 50231 and an ionization chamber TW30013, S/N.364 (0.6 cc Farmer). The chamber was calibrated at the IAEA standard laboratory in terms of absorbed dose to water of ^{60}Co gamma radiation within the required measurement accuracy. The stability of the system was periodically checked at SSDL with stand check source ^{90}Sr/^{90}Y. By recognizing the need of better accuracy to achieve a high degree of consistency, the dosimetry protocol TRS 398 was mainly followed in the present dosimetric measurements. For consistency in radiation dosimetry, IAEA published this code of practice on absorbed dose determination in photons and electron beams, where a number of physical interaction coefficients and correction factors are applied.

2.1 Technical description of ^{60}Co teletherapy units

The ^{60}Co sources of the studied ^{60}Co machines were conventionally incorporated in the treatment head of the telecobalt unit by the manufacturer. The ^{60}Co is an unstable isotope that decays continuously into ^{60}Ni with half-life of 5.27 years, thereby resulting in the decrease in its activity, and hence dose rate (output). It is, therefore, mandatory to measure the dose rate of the ^{60}Co source regularly so that the patient receives the same dose every time as prescribed by the radiation oncologist. In the present study, dosimetry of four ^{60}Co units was performed that belongs to NICRH, MMCH and DMCH. The technical description of these four ^{60}Co units is given in Table 1.

Table 1: Technical description of the studied ^{60}Co teletherapy units

Specification	Unit-1	Unit-2	Unit-3	Unit-4
Model	Elite 100	Elite 80	ATC C9	FYC 260
Manufacturer	Theratronics, Canada	Theratronics, Canada	Advanced Medical Systems Inc., USA	FYC, China
Source activity	443.6 TBq on 06/01/2012	430.2 TBq on 06/04/2012	243.8 TBq on 16/03/2012	277.9 TBq on 20/05/2004

2.2 Absorbed dose to water D_w (Z_{ref}) measurement

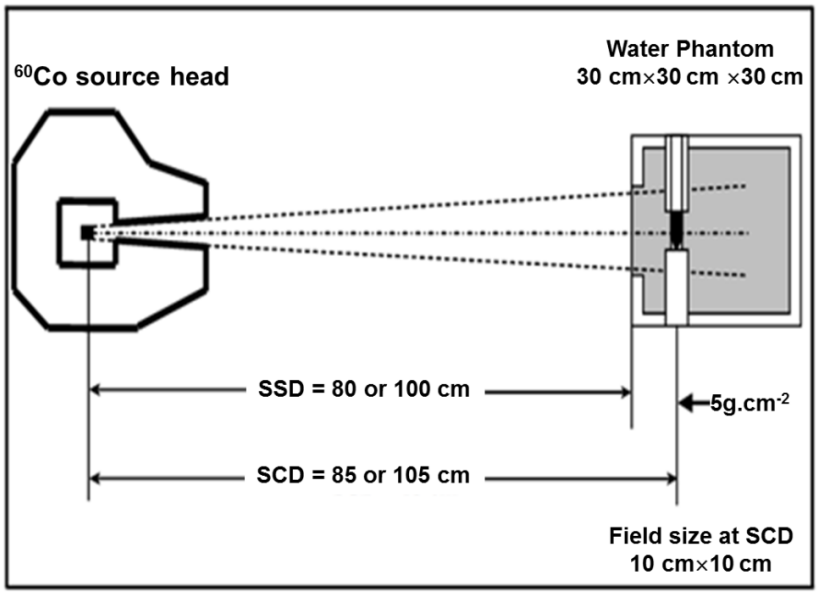

Fig. 1. Schematic diagram of experimental setup for absorbed dose measurement with reference dosimetry system of SSDL.

Absorbed dose to water was measured at the reference condition using the secondary standard ionization chamber coupled with the electrometer of earlier mentioned model. The IAEA reference

water phantom was placed on the couch of the teletherapy machine after being filled up with water. Thereafter, ionization chamber was inserted into the hole of Polymethyl methacrylate (PMMA) waterproof holder. Then, the PMMA holder was placed at 5 cm depth from the front window of the phantom. The gantry of the machine was set at 90 degree (90^0) alignment to ensure the radiation beam position as horizontal. The collimator was adjusted to maintain the field size (s) from 5 cm × 5 cm to 25 cm × 25 cm. The ionization chamber inside the holder was set at 90 degree alignment with the central axis of the beam. The couch position was adjusted to keep the source to water surface distance (SSD) at 80 cm or 100 cm respective to the machine. The schematic diagram of the experimental setup for dose measurement with reference phantom and ionization chamber is shown in Figure1.

The absorbed dose rate D_w at Z_{ref} = 5 cm depth in water was calculated by using the following equation [10].

$$D_w(Z_{ref}) = M_R \times N_{D,W} \times K_{tp} \times K_S \times K_{pol} \text{ cGy/min} \quad (1)$$

Where M_R is the electrometer reading, $N_{D,W}$ is the chamber calibration factor, K_{tp} is the pressure-temperature correction factor, K_s is the ion recombination correction factor, K_{pol} is the polarity correction factor. The calculation process of these correction factors is subsequently discussed.

The pressure-temperature correction factor K_{tp} was calculated by using the following equation.

$$K_{tp} = \frac{(273.2 + T)}{(273.2 + T_0)} \times \frac{P_0}{P} \quad (2)$$

Where T is the ambient temperature, P is the ambient pressure, T_o is the reference temperature, and P_o is the reference pressure. This correction factor is recommended for the open (vented) ionization chambers for air density correction [10].

The ion recombination correction factor K_s was calculated by using the following equation**.**

$$K_s = \frac{(V_1/V_2)^2 - 1}{(V_1/V_2)^2 - (M_1/M_2)} \quad (3)$$

Where M_1 and M_2 are the readings at two voltages V_1 and V_2, V_1 is the normally used polarizing voltage, and V_2 is a voltage reduced by a factor of at least 3. This correction factor for insufficient charge collection in the sensitive volume of the ionization chamber was measured by using the two-voltage method [10].

The polarity correction factor K_{pol} was calculated by using the following equation**.**

$$K_{pol} = \frac{M_1 + M_2}{2M_1} \quad (4)$$

Where M_1 is the positive reading obtained with the usual polarity, M_2 is the positive reading obtained with the opposite polarity. The polarity correction factor due to polarity effect depends on radiation quality [10].

The calculated values of the aforesaid correction factors for 10×10 cm^2 and 20×20 cm^2 field size (s) are given in Table 2.

Table 2: Calculated correction factors for 10×10 cm^2 and 20×20 cm^2 field size (s).

Unit Name	K_{tp}		K_{pol}		K_s	
	10×10 cm^2	20×20 cm^2	10×10 cm^2	20×20 cm^2	10×10 cm^2	20×20 cm^2
Elite 100	1.033	1.031	1.006	1.005	1.001	1.002
Elite 80	1.036	1.035	1.006	1.006	1.001	1.000
ATC C9	1.032	1.030	1.005	1.004	1.000	1.001
FYC 260	1.035	1.034	1.004	1.005	1.002	1.003

2.3 Determination of dose maximum $D_w(Z_{max})$ at the depth Z_{max}

The peak absorbed dose on the central axis of ^{60}Co beam is called dose maximum $D_w(Z_{max})$. Clinical dosimetry calculations are often referenced to the depth of dose maximum Z_{max}. This $D_w(Z_{max})$ was determined at the depth of 0.5 cm in water phantom by using equation (5) [10].

$$D_w(Z_{max}) = \frac{D_w(Z_{ref}) \times 100}{PDD} \text{ cGy/min} \quad (5)$$

Where *PDD* is the percentage depth dose for ^{60}Co beam which is usually normalized to $D_w(Z_{max})$=100% at the depth of dose maximum Z_{max} [11].

2.4 Determination of wedge attenuation factor

The wedge attenuation factor was determined with various wedge filters of different slopes. The wedge filters were placed in the path of incident beam. Gamma attenuation measurement was specified at the axial midpoint of the wedge slope. Attenuation of the incident beam by the wedge filter generally depends on the wedge angle. Attenuation increases with the increment of the wedge angle. Attenuation factors of these filters are essentially required to ensure the prescribed dose for the treatment of target organ. Attenuation factor is defined as the ratio of absorbed dose rate to water $D_w(Z_{ref})$, with and without wedge, at a point in phantom along the central axis of the beam, written as:

$$\textbf{Attenuation Factor} = \frac{\textbf{Absorbed dose } (D_w) \textbf{ with wedge}}{\textbf{Absorbed dose } (D_w) \textbf{ without wedge}}$$

3. RESULTS AND DISCUSSION

3.1 Dosimetric assessment

The absorbed dose rate to water $D_w(Z_{ref})$ at the reference depth of 5 cm, and maximum absorbed dose rate to water $D_w(Z_{max})$ refer to as D_{max} at the depth of 0.5 cm were verified for four ^{60}Co teletherapy machines. Two empirical relations were formulated based on the experimental observation of $D_w(Z_{ref})$ and $D_w(Z_{max})$, as presented by Equation 6 and Equation 7. The empirical

relations were formulated in the form of a quadratic equation by using the trendline options of the excel work sheet based on the experimental observations of depth dose variation with the field size. The experimental absorbed dose rate to water $D_w(Z_{ref})$ at 5 cm depth can be estimated with reasonable accuracy by using the following empirical relation

$$D_w(Z_{ref}) = a_1 \times F^2 + b_1 \times F + c_1 \quad (6)$$

Similarly, the measured maximum absorbed dose rate to water $D_w(Z_{max})$ at 0.5 cm depth can be estimated with satisfactory accuracy by using the following empirical relation

$$D_w(Z_{max}) = a_2 \times F^2 + b_2 \times F + c_2 \quad (7)$$

Where *a*, *b*, *c* are coefficients and *F* is the square field size. The numeric values of the coefficients for Equations (6) and (7) are given in Table 3.

Table 3: Numeric values of the coefficients (a_1, b_1,c_1 and a_2, b_2,c_2) and R^2

Unit name	$D_w(Z_{ref})$			R^2	$D_w(Z_{max})$			R^2
	a_1	b_1	c_1		a_2	b_2	c_2	
Elite 100	–0.042	2.439	94.787	0.997	0.005	0.988	137.03	0.988
Elite 80	–0.099	5.389	186.04	0.998	–0.069	3.982	259.91	0.999
ATC C9	–0.079	4.052	99.694	0.990	–0.066	2.953	153.06	0.987
FYC 260	–0.021	1.097	42.279	0.995	–0.014	0.645	61.692	0.997

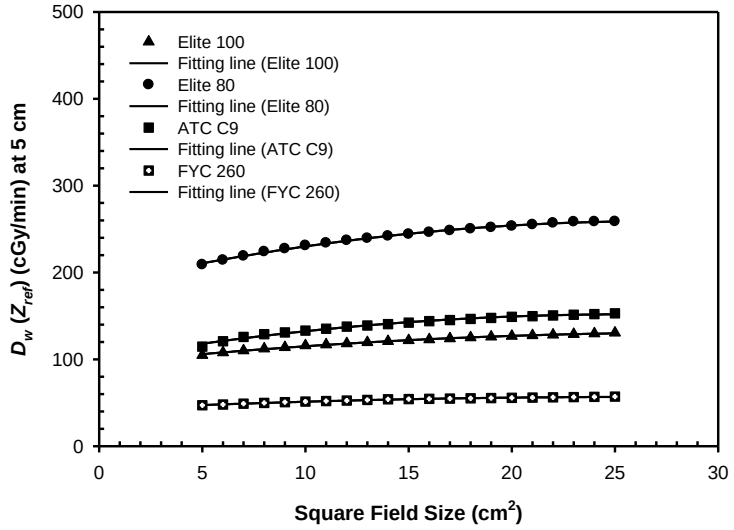

Fig. 2. Comparative variation of absorbed dose rate to water $D_w(Z_{ref})$ at the reference depth.

Table 4: Experimental and estimated $D_w(Z_{ref})$ for field size(s) 10×10 cm^2 and 20×20 cm^2

Unit name	$D_w(Z_{ref})$ for 10×10 cm^2		Relative% difference	$D_w(Z_{ref})$ for 20×20 cm^2		Relative% difference
	Experimental	Estimated		Experimental	Estimated	
Elite 100	115.86	115.03	0.72	126.78	126.96	–0.14
Elite 80	231.12	229.99	0.49	253.4	254.07	–0.26
ATC C9	133.08	132.34	0.55	148.89	149.25	–0.24
FYC 260	51.34	51.17	0.34	55.58	55.89	–0.57

Table 5: Experimental and estimated $D_w(Z_{max})$ for field size(s) 10×10 cm^2 and 20×20 cm^2

Unit name	$D_w(Z_{max})$ for 10×10 cm^2		Relative% difference	$D_w(Z_{max})$ for 20×20 cm^2		Relative% difference
	Experimental	Estimated		Experimental	Estimated	
Elite 100	144.10	147.39	–2.29	152.75	158.72	–3.91
Elite 80	293.30	292.87	0.15	311.l7	312.10	–0.29
ATC C9	168.88	176.02	–4.23	183.13	185.84	–1.48
FYC 260	65.16	69.52	–2.46	68.36	69.08	–1.05

These empirical relations rationally estimated the experimental trend of $D_w(Z_{ref})$ and $D_w(Z_{max})$ within the reasonable accuracy of ±5% as recommended by ICRU [7]. The coefficient of determinant (R^2) of the linear fitting with the experimental values of $D_w(Z_{ref})$ and $D_w(Z_{max})$ for four ^{60}Co machines were found to be satisfactory as given in Table 3. The comparative variation of $D_w(Z_{ref})$ and $D_w(Z_{max})$ for the ^{60}Co teletherapy machines are shown in Figure 2 and Figure 3. The experimental and estimated $D_w(Z_{ref})$ for field size 10×10 cm^2 and 20×20 cm^{2}are given in Table 4. From Table 4, it is seen that the minimum and maximum relative deviation between the experimental and the estimated values of $D_w(Z_{ref})$ were found to be –0.14%and 0.72% for Elite 100 machine at field size (s)10×10 cm^2 and 20×20 cm^2, respectively. In the case of $D_w(Z_{max})$, this minimum deviation was found to be 0.15% and –0.29% for Elite 80 at field size 10×10 cm^2 and 20×20 cm^2, respectively as given in Table 5. The maximum deviation of $D_w(Z_{max})$ was found to be –4.23% at field size10×10 cm^2 for ATC C9 and 3.91% at field size 20×20 cm^2 for Elite 100. Relatively good agreement was observed for $D_w(Z_{ref})$ based on the relative % difference between the experimental and estimated values at 10×10 cm^2 and 20×20 cm^2 field size (s) in comparison to $D_w(Z_{max})$ in the cases of all the studied ^{60}Co machines as presented in Table 4 and Table 5.

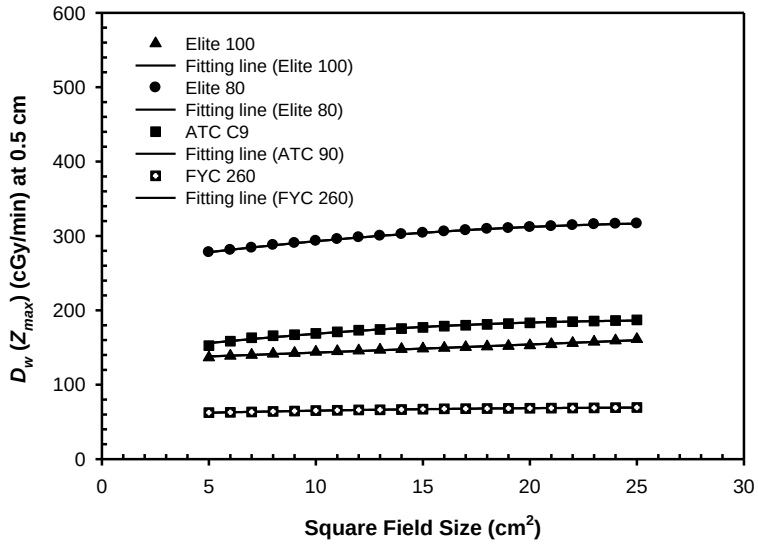

Fig. 3. Comparative variation of absorbed dose to water $D_w(Z_{max})$ at the depth of dose maximum.

3.2 Variation of wedge attenuation factors with field size

A representative assessment of the wedge attenuation factors for various field sizes and wedge dimensions of two teletherapy units (Elite 80 and FYC 260) are investigated. A wedge is a polyhedron defined by two triangles and three trapezoid faces where a wedge has five faces, nine edges, and six vertices. The structure of wedges was such that the alignments of the triangle and trapezoid faces collapsed into a line and form a regular pentagon. In this study, the place of gamma attenuation evaluation was at the axial midpoint of the wedge slope at where the measurement was done. The wedge attenuation factors corresponding to three wedge angles of the aforesaid teletherapy units are presented in Table 6. This table indicates that the decrement of the wedge attenuation factors was found to be relatively small for increment of wedge angles.

Table 6: Wedge attenuation factors at various wedge angles of Elide 80 and FYC260 ^{60}Co teletherapy machines

Wedge dimension in cm^2	Field size(s) in cm^2	Wedge angle(s) in degree	Wedge Attenuation Factors	
			Elite 80	FYC 260
6×15	6×6	30^o	0.7835	0.7852
		45^o	0.6724	0.7338
		60^o	0.5333	0.6157
8×15	8×8	30^o	0.7426	0.7329
		45^o	0.6195	0.6621
		60^o	0.4618	0.5729
10×15	10×10	30^o	0.7097	0.7285
		45^o	0.5732	0.6074
		60^o	0.4008	0.5075

The variation of the wedge attenuation factor with field size is presented in Figure 4. From this figure a descending trend of wedge attenuation factors with increment of field sizes was observed for both teletherapy machines. Thus, larger wedge attenuation factor corresponds to smaller field size. In this study, a representative measurement of wedge attenuation was performed for the two machines only for a simplified assessment. This is because for the same wedge material and wedge angle very similar trend is supposed to be found for the wedge attenuation factors which already investigated for the two machines.

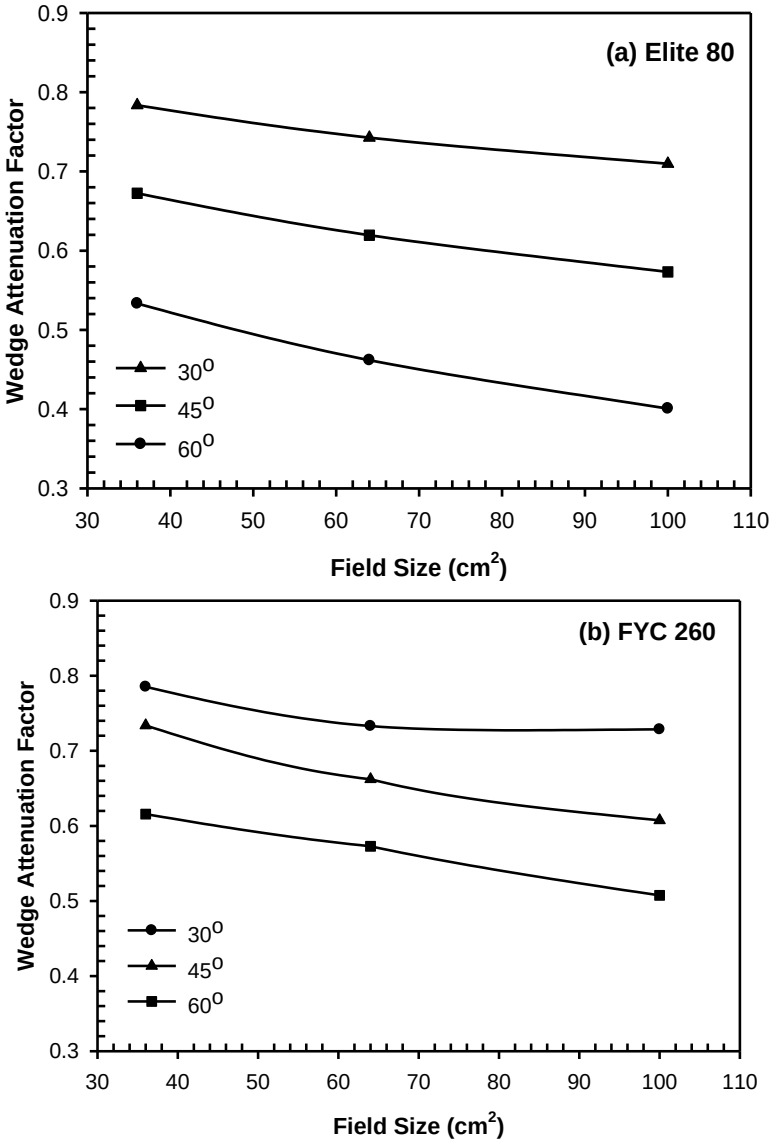

Fig. 4. Variation of the wedge attenuation factors for (a) Elite 80 and (b) FYC 260 ^{60}Co teletherapy machines.

4. CONCLUSIONS

A comparative evaluation of the dosimetric characteristic of four ^{60}Co units was performed. The absorbed dose to water $D_w(Z_{ref})$ at reference depth and dose maximum $D_w(Z_{max})$ for the ^{60}Co teletherapy units was measured. Two empirical relations were formulated that reasonably estimated the experimentally measured $D_w(Z_{ref})$ and $D_w(Z_{max})$ within the accuracy of ±5%. The coefficient of determinant (R^2) of the linear fitting with the experimentally measured $D_w(Z_{ref})$ and $D_w(Z_{max})$ indicated a good agreement between the estimated and experimental results of the studied ^{60}Co machines. Thus, the empirical relations could be a good option for the routine dosimetric QA of the ^{60}Co machines. Similar empirical relations were formulated to use in the cases of other machines as described elsewhere [12]. An assessment of the wedge attenuation factors for various field size (s) and wedge dimensions of two teletherapy units are performed. The increment of the wedge attenuation factors at various wedge angles was found to be relatively small for a particular field size and wedge dimension. In addition, a descending trend of wedge attenuation factors with increment of field sizes was observed for both teletherapy machines.

REFERENCES

[1] James D. Cox and K. Kian Ang, "Radiation Oncology", Ninth Edition, Elsevier Inc. (2010).

[2] P. Cadman, "An investigation of beam parameters for Co-60 tomotherapy", Med. Phys. **34**, 3838–3843, (2007).

[3] C. Fox, H. E. Romeijn, B. Lynch, C. Men, D. M. Aleman, J. F., "Comparative analysis of Co-60 intensity-modulated radiation therapy", Phys. Med. Biol. **53**, 3175–3188 (2008).

[4] C. P. Joshi, J. Darko, P. B. Vidyasagar, L. J. Schreiner, "Investigation of an efficient source design for Cobalt-60 based tomotherapy using EGSnrc Monte Carlo simulations", Phys. Med. Biol. **53**, 575–592 (2008).

[5] International Atomic Energy Agency, Absorbed dose determination Photon and Electron beams: An international code of practice, Technical Report Series No. 277, IAEA, Vienna, (1987).

[6] Bangladesh Gezette, Nuclear Safety and Radiation Control Rules- SRO No. 205-Law/97, (1987)

[7] M. D. Bethesda, "International Commission on Radiation Units and measurements, Determination of Absorbed Dose in a Patient Irradiated by Beams of X or Gamma Rays in Radiotherapy Procedures", ICRU Rep. 24, ICRU Publications (1976).

[8] A. Brahme, "Dosimetric Precision Requirements in Radiation Therapy", Acta. Radial. Oncol., **23**, 379-387 (1984)

[9] International Atomic Energy Agency, IAEA/WHO Network of Secondary Standard Dosimetry Laboratories comparison of calibration coefficients certificate, MAL/05/01, 05, IAEA, Vienna, (2000).

[10] International Atomic Energy Agency, "Absorbed dose determination external beam radiotherapy: An international code of practice for dosimetry based on standards of absorbed dose to water", Technical Report Series No. 398, IAEA, Vienna, (2000).

[11] E. G. A. Aird, J. E. Burns et al., "Central Axis Depth Dose Data for Use in Radiotherapy": 1996, British journal of radiology (BJR) supplementary 25, British Institute of Radiology, London (1996).

[12] M. S. Rahman, A. F. M. Rahman, A. Koddus and G. U. Ahmad, "Dosimetry of 60Co teletherapy units used for the treatment of cancer patients at various hospitals in Bangladesh", Jahangirnagar Phys. Studies, **10** (2004).

*Bangladesh Journal of Physics, **23&24**, 33-39, 2018*

SPIN-ORBIT COUPLING IN DISORDERED SYSTEM

AIN-UL HUDA[1], AFIYA AKTER PIYA[1], MAINUL ISLAM[2] AND MIZANOR RAHMAN[2]

[1]*Department of Physics, Jagannath University, Dhaka-1100, Bangladesh*

[2]*Department of Mathematics, Jagannath University, Dhaka-1100, Bangladesh*

** Corresponding author:E-mail:ainul.huda@gmail.com*

Received on 05. 07. 2018, Revised received on 18. 07. 2018, Accepted for Publication on 24. 07. 2018

ABSTRACT

In an earlier communication [1], we observed that spin-orbit coupling play significant role in alloys of the heavier elements. In the same communication, we proposed methodology for take into account the spin-orbit coupling in the recursion method for ordered system. The basis used for the representation of the Hamiltonian is the TB-LMTO[2]. Since its spareness is an essential requirement for recursion. We also extend the model for the rough surfaces. We presented some numerical examples to validate our assumption. The recursion technique [3,4] can then be extended to augmented space to deal with disordered alloys.

1. INTRODUCTION

The discussion of stability properties of alloys of heavier elements requires the inclusion of relativistic corrections to standard electronic structure calculation. It was argued by Singh [5] and Paudyalet. al [6] that unless one include at least the scalar relativistic corrections for NiPt, one cannot predict the observed low temperature ordering in the 25%, 50% and 75 % composition alloys. Scalar relativistic corrections e.g. Mass-velocity corrections and Darwin corrections are now routinely incorporated in most electronic structure calculations for both ordered compounds as well as disordered alloys. The inclusion of Spin-orbit coupling has been less common. We presented the methodology for including spin-orbit coupling in ordered system.

In many-electron systems the spin-orbit Hamiltonian [7] can be written as,

$$H_{SO} = \frac{1}{c^2}\frac{1}{r}\frac{dV(r)}{dr}\vec{L}.\vec{S} = v(r)\vec{L}.\vec{S} \tag{1}$$

As in earlier communication[8], we shall use the self-consistently compound LSDA potential in an atomic sphere for the potential V(r). We shall use the spherically averaged form as in standard LMTO approaches, although this restriction may be relaxed. We shall use the spherically averaged form, as in standard LMTO approaches, although this restriction may be relaxed. We shall also use inflated atomic spheres and neglect contributions from the interstitial regions. The use of the LSDA potential in H_{SO} has really no formal justification. Stiles et.al. [9] have argued that a more systematic approach should be incorporate, within the Hamiltonian, two-body terms of the kind introduced by Breit [10]. This would require corrections to the Hartree energy of the form;

$$E_{so} = \frac{\alpha^2 E_h a_0^3}{4}\int d^3\vec{r}\int d^3\overline{r'}\left\{n(\vec{r})\vec{d}(\vec{r}).\frac{\vec{r}-\overline{r'}}{|\vec{r}-\overline{r'}|^3} - 2\vec{j}(\vec{r}).\overline{m}(\vec{r}) \times \frac{\vec{r}-\overline{r'}}{|\vec{r}-\overline{r'}|^3}\right\} \tag{2}$$

where $\alpha \cong 1/137$, E_h =27.21 eV and a_0=0.529 nm and,

$$n(\vec{r}) = \sum_{i\ \epsilon occ,\sigma} \psi^*_{i\sigma}(\vec{r})\psi_{i\sigma}(\vec{r})$$

$$\vec{j}(\vec{r}) = i \sum_{i\epsilon occ,\sigma} \psi^*_{i\sigma}(\vec{r})\vec{\nabla}\psi_{i\sigma}(\vec{r})$$

$$\vec{m}(\vec{r}) = \sum_{i\epsilon occ,\sigma} \psi^*_{i\sigma}(\vec{r})\vec{\sigma}\psi_{i\sigma}(\vec{r})$$

$$\vec{d}(\vec{r}) = \psi^*_{i\sigma}(\vec{r})\vec{\sigma} \times \vec{\nabla}\psi_{i\sigma}(\vec{r})$$

The variational derivative of the above equation (2) with respect to the wave function would yield the effective spin-orbit term that enters the Kohn-Sham equation as H_{SO}. The first term yields the standard spin-orbit term shown by us earlier. The second term yields the so-called "spin-other orbit" Hamiltonian, which we have neglected in this work.

2. METHODOLOGY OF PRESENT WORK

The procedure mentioned in [1] for ordered and surface study may be generalized for application to disordered alloys through the augmented space technique [11]. The methodology has been described in great detail in earlier papers and the reader are referred to the review [12] for details. Operationally the augmented space theorem [12] states that: if we can represent the Hamiltonian in a countable (site labelled) basis where the disorder appears in the single site terms, we may augment the Hamiltonian by replacing the random elements by operators whose spectral densities are their probability densities. This augmented Hamiltonian in an operator in a space which is the product of the space spanned by the countable basis and the spanned by the configuration state, which, in analogy with many-body scattering theory we call the vacuum state. The configuration averaged Green function may then be obtained through the recursion method on the full augmented space.

First we rewrite the Hamiltonian as follows:

$$\begin{aligned} H \ &= \ \Delta^{1/2}[\,\tilde{C} + S - \ (C' + S)o'(C' + S) + \cdots \\ &\quad \ldots + A' + (C' + S)B' + \hat{B}',(C' + S) + \mathrm{C}'\,C'\mathrm{C}' + S\,C'S]\Delta^{1/2} \\ &= \ \Delta^{1/2}[\tilde{\mathbf{C}} + S - \mathbf{H}']\Delta^{1/2} \end{aligned} \tag{3}$$

where we have:

$$o' \ = \ o\,\Delta \qquad\qquad \tilde{\mathbf{C}} = \frac{C}{\Delta}C' = \frac{C\,E}{\nabla}$$

$$C' \ = \ \Delta^{1/2}C\Delta^{1/2}B' = \Delta^{1/2}B\Delta^{-1/2}B', = \Delta^{-1/2}B\Delta^{1/2}$$

$$A' = \Delta^{-1/2}A\Delta^{-1/2} \tag{4}$$

For a substitutional binary random alloy, the site labelled potential parameters have a binary distribution: taking values appropriate for the A and B constituents with probabilities proportional to their concentrations: $x_A$and x_B. The corresponding configuration space is isomorphic to that for an Ising model and the operator whose spectrum is the probability density is:

$$M^R = x_A P_\uparrow + x_B P_\downarrow^R + \sqrt{x_A x_B}\ (T_{\uparrow\downarrow}^R + T_{\downarrow\uparrow}^R)$$

From equation (3) we get:

$$G(z) = \left(z\, I - \Delta^{1/2}\left[\tilde{\mathbf{C}} + \boldsymbol{S} - \boldsymbol{H}'\right]\Delta^{1/2}\right)^{-1}$$

$$= \Delta^{-1/2}\left(z\,\Delta^{-1} - \tilde{C} - S + H'\right)^{-1}\Delta^{-1/2} \tag{5}$$

We shall now apply the augmented space theorem to obtain the following: for any single site labelled random Hamiltonian element $K \in \mathcal{H}$, using the augmentation transformation we obtain

$$\hat{K} = \sum_R \{\frac{A(K_R)}{A\left(\Delta_R^{-1/2}\right)^2} P_R \otimes I + \frac{B(K_R)}{A\left(\Delta_R^{-1/2}\right)^2} P_R \otimes P_\downarrow^R + \cdots$$

$$\ldots + \frac{F(K_R)}{a\left(\Delta_R^{-1/2}\right)^2} P_R \otimes (T_{\uparrow\downarrow}^R + T_{\downarrow\uparrow}^R)\}$$

For terms which are not random we have, for example,

$$\hat{S} = \sum_R \sum_{R' \neq R} S_{R\,R'} T_{RR'} \otimes I$$

where, K_R and $S_{RR'}$ are matrices $K_{R,LL'}$ and $S_{RL,R'L'}$ in angular momentum-spin indices and,

$$A(K_R) = x_A K_A + x_B K_B$$

$$B(K_R) = (x_A - x_B)(K_A - K_B)$$

$$F(K_R) = \sqrt{x_A x_B}\ (K_A - K_B)$$

The configuration averaged Green function matrix element is:

$$\ll G_{RR}(Z) \gg = \ll 1 | \left(z\,\hat{I} - \hat{H}_{eff}\right)^{-1} | 1 \gg$$

where,

$$|1 \gg = |R \otimes \{\emptyset\} > + \frac{F\left(\Delta_R^{-1/2}\right)}{A\left(\Delta_R^{-1/2}\right)} \quad | R \otimes \{R\} >$$

and,

$$\hat{H}_{eff} = [\, z\left(\hat{I} - \widehat{\Delta^{-1}}\right) + \hat{\tilde{C}} + \hat{S} - \left(\hat{C}' + \hat{S}\right)\hat{o}'\left(\hat{C}' + \hat{S}\right) + \cdots$$

$$\ldots\ldots + \hat{A}' + \left(\hat{C}' + \hat{S}\right)\hat{B}', \left(\hat{C}' + \hat{S}\right) + \hat{C}'\widehat{C'}\hat{C}' + \hat{S}\hat{C}'\hat{S}\,] \tag{6}$$

States in the configuration space are uniquely labelled by the cardinality sequence $\{R_1, R_2, \ldots\}$ which denotes the sites at which we have a configuration fluctuation (denoted by a ↓) from the average state (denoted by an ↑). The configuration averaged Green function is then obtained directly by recursion in the augmented space with $|1 \gg$ as the starting state. The averaged density of states and both the local and averaged magnetic moments may then be obtained from the averaged Green functions.

The general recursion method out a change of basis starting from a chosen state in the Hilbert space, repeatedly operating on by the Hamiltonian and subtracting project on the earlier members through a three terms recurrence relation [2]. The calculations yield the Green function as a continued fraction:

$$G_{RL,RL}(E) = \langle R, L|(E\mathbf{I} - \mathbf{H})^{-1}|R, l\rangle$$

$$= \cfrac{1}{E-\alpha_1-\cfrac{\beta_1^2}{E-\alpha_2-\cfrac{\beta_2^2}{\ddots\,\cfrac{\beta_N^2}{E-\alpha_N-T(E)}}}} \tag{7}$$

$T(E)$is the appropriate terminator obtained from the initial part of the continued function. The terminator preserves the herglotz analytic properties of the approximated Green function. We have used the terminator of Luchini and Nex [13]. To obtain the magnetic moment, we first obtain the spheridized local charge density within an atomic sphere centered at R:

$$\rho_\sigma^{(i)} = \frac{1}{4\pi}\sum_l [\, m_{Rl}^{(0)}\varphi_{l\sigma}(r_R)^2 + 2\, m_{Rl}^{(1)}\varphi_{l\sigma}\dot{\varphi}_{l\sigma} + \cdots$$

$$+ m_{Rl}^{(2)}\{\, \dot{\varphi}_{l\sigma}(r_R)^2 + \varphi_{l\sigma}(r_R)\ddot{\varphi}_{l\sigma}(r_R) \tag{8}$$

where the energy moments are

$$m_{Rl}^{(n)} = \frac{1}{\pi}\,\Im m \int_\infty^{E_F} dE\; G_{RL,RL}(E)\big(E - E_{v,Rl}\big)^n$$

The magnetization density within that sphere is:

$$M^{(i)}(r_R) = \rho_\uparrow^{(i)}(r_R) - \rho_\downarrow^{(i)}(r_R)$$

The charge and magnetization densities are then inputs into the self-consistency iterations using the LSDA. If we wish to carry out a fully self-consistent solution then the charge and magnetization densities are input into an expression of the total energy which should include a Breit like term as in equation (2). However, because of the smallness of the spin-orbit correction, one usually carries out calculation with it after convergence. In this work we have followed this procedure and left the study of the effect of full self-consistency for a later work.

The magnetic moment per atom is given by:

$$M_R^{(i)} = \int_0^{s_R} M^{(i)}(r_R) r_R^2\, dr_R$$

Also the band energy per atom is given by

$$E_{band}^{(i)} = \int_0^{S_R} \left(\rho_{\uparrow}^{(i)}(r_R) + \rho_{\downarrow}^{(i)}(r_R)\right) dr_R$$

3. COMPUTATIONAL DETAILS

For the calculation of the component projected averaged density of states of the binary alloys at different compositons; : $Ni_{25}Pt_{75}$, $Ni_{50}Pt_{50}$ and $Ni_{75}Pt_{25}$, we have used a real space cluster of 400 atoms and an augmented space shell upto sixth nearest neighbor from the starting state. Eight pairs of recursion coefficients were determined exactly and the continued fractionis terminated by the terminator proposed by Luchini and Nex [11]. For the spin-orbit coupling term, we compared our calculations with the parameters estimated by Daalderop et.al. [12].

Table 1: The value of d-state spin orbit coupling parameters for different metals and alloys

Huda et. al. Ordered calculation			Daalderop et. al. Calculation			Present calculation		
Material	A_{ll} ↑	A_{ll} ↓	Solid ↑	Solid↓	Atomic	Material	A_{ll} ↑	A_{ll} ↓
Ni	6.31	6.06	6.98	6.91	6.47			
Ni in Ni_3Pt	6.28	6.08				Ni in $Ni_{75}Pt_{25}$	5.98	5.97
PT in Ni_3Pt	14.16	13.84				Pt in $Ni_{75}Pt_{25}$	13.26	13.03
Ni in NiPt	6.15	6.15				Ni in $Ni_{50}Pt_{50}$	5.89	5.78
Ni in NiPt	14.04	14.04				Pt in $Ni_{50}Pt_{50}$	13.76	13.71
Ni in $NiPt_3$	6.19	5.96				Ni in $Ni_{25}Pt_{75}$	5.80	5.72
Ni in $NiPt_3$	14.11	13.99				Pt in $Ni_{25}Pt_{75}$	13.88	13.82

Out estimates for Ni are in good agreement with the results quoted by Daalderopet. al. [12] . It should be noted that the parameter quoted by Daalderopet. al .is only a part of the contribution of the spin-orbit term of the hamiltonian, although it is the most dominant one. Other contributions come from the off –diagonal elements of $A_{LL'}$ as well as from the $B_{LL'}$ and $C_{LL'}$.

We carry out the recursion calculations with the spin-orbit part of the Hamiltonian included. Note that we now have to calculate the majority and minority spins simultaneously becuase the presence of spin-orbit coupling leads to off-diagonal term in the Hamiltonian between the spin states.

4. RESULTS

Figure 1 displays the density of states of $Ni_{75}Pt_{25}$, $Ni_{50}Pt_{50}$and $Ni_{25}Pt_{75}$ with spin-orbit coupling. In all these cases the fermi energy of the density of states are shifted to zero. Figure 2 displays the fractional change in the spin-resolved density of states of of $Ni_{75}Pt_{25}$, $Ni_{50}Pt_{50}$and $Ni_{25}Pt_{75}$

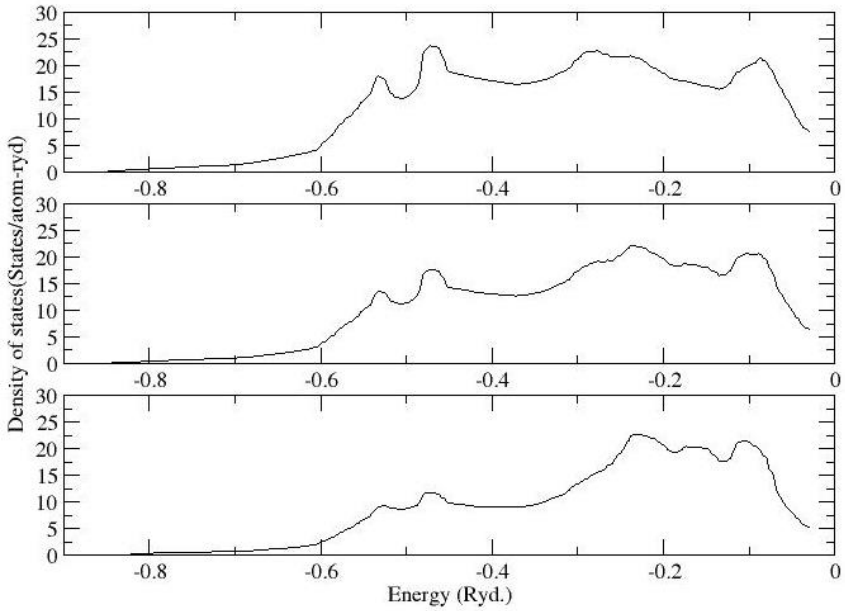

Fig. 1. Density of states for (top) $Ni_{25}Pt_{75}$, (middle) $Ni_{50}Pt_{50}$ and (bottom) $Ni_{75}Pt_{25}$ with Spin-orbit coupling included.

Table 2: Comparision between Band Energy(Ryd) and Magnetic moment(Bohr-Magneton/atom-cell) for ordered $NiPt_3$, NiPt and Ni_3Pt and disordered $Ni_{25}Pt_{75}$, $Ni_{50}Pt_{50}$ and $Ni_{75}Pt_{25}$ (a) Recursion method without LS coupling (b) With LS coupling.

Examined properties	Ordered Alloys [1]			Disordered Alloys		
	$NiPt_3$	NiPt	Ni_3Pt	$Ni_{25}Pt_{75}$	$Ni_{50}Pt_{50}$	$Ni_{75}Pt_{25}$
Band Energy (a)	4.931	4.682	4.276	4.686	4.523	4.445
Band Energy (b)	5.032	4.717	4.411	4.781	4.592	4.491
Diff(b-a)	0.130	0.090	0.070	0.095	0.069	0.046
Magnetic Moment(a)	0.190	0.000	0.413	0.232	0.334	0.465
Magnetic Moment (b)	0.203	0.005	0.422	0.277	0.355	0.476
Diff(b-a)	0.013	0.005	0.009	0.045	0.021	0.011

Table 2. represents the band energies and magnetic moments per atom per cell for the above mentioned disordered alloys. In case of Ni and Pt based alloys, the change of band energies and magnetic moments increases with the increase of heavier atom (Pt) in the disorded alloys. It is also observed earlier [1] in case of ordered alloys. So it is evident from here that in case of presence of heavier atom, inclusion of spin-orbit coupling term is necessary. Because of spin-orbit coupling term, the paramagnetic Pt possess a magnetic moment, which gives rise to non-collinearity in Pt.

5. CONCLUSIONS

In this work, we present the methodology to include spin-orbit coupling term in recursion method for the disordered system. It is found from our numerical calculation that the spin orbit coupling term is very important is important in alloys having heavier elements in case of disordered alloys just like the ordered alloys found earlier. The spin-orbit coupling has been found to be important for calculating the non-collinearity of magnetic moment and also for calculating anisotropic magneto crystalline energy. We intend to carry forward our calculation in these directions.

ACKNOWLEDGEMENT

AH like to thank University Grants Commission and Jagannath University for the financial support through the project “Electronic and Magnetic Properties of Bulk, Rough Surfaces and Interfaces”.

REFERENCES

[1] Ain-ul Huda, D. Paudyal, A. Mookerjee, M. Ahmed, *Physica B: Condens. Matter*, **351**, pp 63 (2004).

[2] O. K. Andersen ,*Phys. Rev.* B **12**, pp3060(1975) ; O. K. Andersen and O. Jepsen, *Phys. Rev. Lett.* **53**, pp 2571 (1984).

[3] R. Haydock, V Heine and M J Kelly, *J. Phys. C; Solid State Phys.* **5**, pp 2845 (1972).

[4] R. Haydock, V Heine and M J Kelly, *Surf.Sci.* **38**, pp 139 (1973).

[5] P P Singh, AGonis and P. A. E. Turchi, *Phys. Rev. Lett.* **71**, pp 1605 (1993)

[6] D. Paudyal, T. Saha-Dasgupta and A. Mookerjee, *J. Phys: Cond. Matt.* **15**, pp 1029 (2003).

[7] G Baym, *Lectures on Quantum Mechanics*, Benjamin, Reading, M.A.(1974).

[8] B. Sanyal, P. Biswas, T. Saha-Dasgupta, A. Mookerjee, A. Huda, N. Choudhury, M. Ahmed and A. Halder, *J. Phys; Cond. Matt.* **11**, pp 1833 (1999); S. Ghosh and A. Mookerjee, *J. Mag. Mag. Mat.* **214,** pp 291 (2000).

[9] M. D. Stiles, S. V. Halivov, R. A. Hyman and A Zangwill, *Phys. Rev. B.* **64**, pp 104430 (2001).

[10] G. Breit, *Phys. Rev.* **34**, pp 553(1929); *Phys. Rev.* **36**, pp 383(1930); *Phys. Rev.* **39**, pp 553 (1929).

[11] A. Mookerjee, *J. Phys.* **C6**, L 205 (1973).

[12] A. Mookerjee, in “*Electronic Structure of Alloys, Surfaces and Clusters”*, ed. Mookerjee A and Sarma D. D , Gordon and Breach (2000).

[13] M. U. Luchini and C M MNex, *J. Phys. C: Condenss: Solid State Phys.* **20**, pp 3125 (1987).

*Bangladesh Journal of Physics, **23 & 24**, 41-50, 2018*

EVALUATION OF ANNUAL EFFECTIVE DOSE FOR NATURAL RADIOACTIVITY OF GAMMA EMITTERS IN VEGETABLES SAMPLES FROM NORTHERN PART IN BANGLADESH

MD. MAHIDUL HAQUE PRODHAN[1*], MD. HOSSAIN SAHADATH[1], MD. JAFOR DEWAN[1], ALEYA BEGUM[2], JANNATUL FERDOUS[2]

[1]*Department of Nuclear Engineering, University of Dhaka, Dhaka-1000, Bangladesh*

[2]*Health Physics Division, Atomic Energy Centre, Dhaka, Bangladesh*

** Corresponding author: E-mail: prodhan@du.ac.bd*

Received on 16.04.2018, Revised received on 05.06.2018, Accepted for publication on 28.08.2018

ABSTRACT

The aim of the present work were to measure the radioactivity levels and annual effective dose as a result of the intake of vegetables samples collected from Northern part in Bangladesh. The natural radioactivity levels were identified and measured by gamma-ray spectrometry. The observed concentrations of radionuclides in vegetable samples ranged from $21.47 \pm 0.85\ Bq\ kg^{-1}\ to\ 61.99 \pm 5.11\ Bq\ kg^{-1}$ with average $36.53\ Bq\ kg^{-1}$for ^{238}U; from $3.08 \pm 0.07\ Bq\ kg^{-1}\ to\ 7.54 \pm 0.61\ Bq\ kg^{-1}$ with average $5.54\ Bq\ kg^{-1}\ for\ ^{232}Th$; The activity concentration of ^{40}K in vegetable samples ranged from $306 \pm 16.23\ Bq\ kg^{-1}\ to\ 519 \pm 43.17\ Bq\ kg^{-1}$ with average activity $407\ Bq\ kg^{-1}$. Artificial nuclide was not observed in any of the samples. Also the annual effective dose due to the ingestion of such vegetables by the population of Bangladesh was studied. The estimated total annual effective dose for the ingestion of different vegetables samples and their derived products with the long lived natural radionuclides is found to be $0.329\ mSvy^{-1}$, which is insignificantly higher than the total exposure per person resulting from ingestion of terrestrial radioisotopes $0.29\ mSv$ as proposed by the United Nations Scientific Committee on the Effects of Atomic Radiation (UNSCEAR) but this values is below the recommended limit by International Commission on Radiological Protection ($ICRP$) as the annual dose to members of the public, $1\ mSvy^{-1}$.

Keywords: Radioactivity level**,** Vegetables samples, High purity Germanium ($HPGe$) Effective dose.

1. INTRODUCTION

Radiation, a fact of our somatic biosphere of everyday life, is energy travelling through space. Exposure to radiation has origins such as medical diagnostic and therapeutic procedures [1], natural background radiation, nuclear electricity generation and accidents in Nuclear Power Plant (NPP), nuclear weapon production & testing [2]. But the natural source of radiation in surroundings is responsible for some background radiation [3]. People have potentially been exposed to natural ionizing radiation from both terrestrial and extraterrestrial origin. Total number of main natural radionuclides from three decay series namely, Uranium, Thorium and Actinium, would be around fifty having varying metabolic, chemical and physical properties. Also, Potassium-40 (^{40}K), Rubidium-87 (^{87}Rb), Indium-138 (^{138}In), Lanthanum-138 (^{138}La) and Samarium-147 (^{147}Sm) etc. are particular non-series single natural radionuclide, which subsidize to

individuals both on the inside and on the outside. Some of the exposures are fairly constant and uniform for all individuals universally, for example, the dose from ingestion of ^{40}K in foods, while other exposure such as cosmic rays depending on location [4, 5]. It is higher at higher altitude [6]. The artificial radionuclides are those which are formed as a consequence of medical and industrial uses of radioisotopes, the handling of NPPs and as by products from nuclear fuel cycle and other from mining, milling, fuel enrichment, fuel preparation for reactor use and plant operation disposal, nuclear weapon tests, nuclear accidents [7]. The airborne elements may be interrupted by plants or reappearance to the topmost soil during the discharges of radionuclides. As a result, Plants may get radioactive nuclides in the two ways: by the deposition of radioactive fallout on the plants directly and by absorption from the soil [8]. The total exposure per individual causing from ingestion of terrestrial radioisotopes was 0.29 mSv, of which 0.17 mSv was from ^{40}K and 0.12 mSv was from thorium (Th) and uranium (U) series, report by UNSCEAR. Exposure from inhalation of terrestrial radioisotopes subsidizes further 0.01 mSv [9].

The external and internal radiation dose in human body may spread the possibility of cancer and various radiation-induced problems in the body tissues and may be dangerous to the entire people [5].^{232}Th, ^{238}U, ^{210}Pb, ^{226}Ra and ^{228}Ra are present in leafy vegetables, fruit, root, bean and rice, and consequential foodstuffs like manioc flour, corn flour, wheat flour sugar, coffee and pasta etc. The annual effective dose due to the ingestion of vegetables and their consequential food stuffs with the long lived natural radionuclide is 14.5μSv [10]. In this research paper, activity concentrations of ^{40}K, ^{232}Th and ^{238}U radionuclides in different vegetable samples from Rangpur and Rajshahi Division in Northern part of Bangladesh were analyzed as a part of domestic food to launch standard data for the activity level of the radionuclides.

2. MATERIALS AND METHODS

2.1 Sample collection and preparation

Two sampling sites were selected in the Northern part of Bangladesh for the collection of vegetable samples. Fig. 1 shows the sampling sites of Rangpur and Rajshahi Division. The sampling stations are located by the geographical position of Latitude $25.8483° N$ and Longitude $88.9414° E$. The conditions for the vegetables selection are usually expended appetizing vegetables by the individuals of Bangladesh. Vegetable samples generally grown and consumed were collected in the harvesting season. To ensure sufficient representation of each area, thirty vegetable samples from the different sampling sites of both areas were collected. In order to determine the fresh weight of the sample, each sample is washed with tap water and peeled, if necessary and then dried in air. After that weight of each sample is taken. The ranges of fresh weight for vegetable samples are from $1\ kg$ to $2\ kg$. Then the samples are cut into suitable sizes for dried into a oven and burned approximately 24 h at 105 ℃. The dried samples are grinded, sieved and then reweighed. Now the weight of the sample gives the dry weight of the samples. The dry weight of the sample varies from $90\ gm$ to $278\ gm$. Each vegetable sample is sealed individually into cylindrical screw-cap plastic containers ($6.5\ cm\ dia. \times\ 7.5\ cm\ height$). Measurement of the sealed sample has been carried out after 4 weeks due to allow the establishment of radioactive equilibrium between radium and its short –lived daughter products [11].

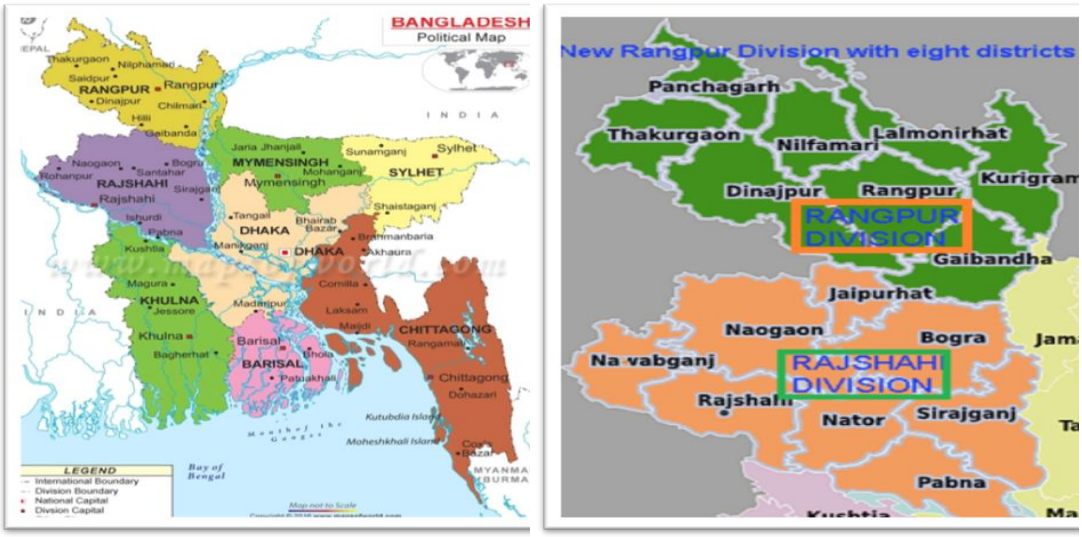

(a) (b)

Fig. 1. (a) Map of Bangladesh and (b) Map of Rangpur and Rajshahi Division.

2.2 Measurement of radioactivity

The radioactivity measurements were performed by a high-resolution gamma spectroscopic system employing a high purity germanium crystal ($HPGe$) coupled with Multichannel analyzer. This detector is a $p-type$ co-axial detector and low background to determine gamma-ray emitters. The effective volume of the detector was 83.46 cm^3 and energy resolution of the 1.33 MeV energy peak for ^{60}Co was found as 1.69 keV at full width half maximum ($FWHM$) with a relative efficiency of 19.6%. The gamma-ray spectrum of each individual sample was recorded using a PC based 4096 channel analyzer and processed by Silena Emca plus software. The bias voltage of the detector was $+3200\ volts$. In order to reduce the thermally generated charge carrier to an acceptablelevel, the detector is cooled by liquid nitrogen of temperature of $77\ K$, which is the common cooling medium of the detector. To minimize the effect of the scattered radiation from the shield, the detector is located at the center of the chamber. The detector was calibrated using gamma-ray standard point sources. The counting time for each sample was $20000\ sec$. The detector was shielded by $10\ cm$ lead on all sides with $2\ mm$ copper in inner sides and lead shielding covered by lead bricks at the top to reduce background radiation effects. The background spectra were measured frequently under the same conditions in order to correct the calculated sample activities. The characteristic gamma peaks selected for the determination of the different radionuclides were $352\ keV$ (^{214}Pb), $609\ keV$ (^{214}Bi) for ^{238}U, $238.63.0\ keV$ (^{212}Pb), $911\ keV$ (^{228}Ac) for ^{232}Th and $1461\ keV$ for the ^{40}K. Gamma ray spectrum of a vegetable sample is shown in Fig.2 [12].

In order to perform the quality control for making relevant samples, a sample with a defined activity was analyzed using the generated efficiency curve which is shown Fig. 3 [12]. The equation (i) & (ii) were used to calculate the efficiency at different energy.

$$A = A_0 e^{\lambda t} = A_0 e^{-[0.693 t / \frac{t_1}{2}]} \quad \text{.....(i)}$$

Where, A_0= the initial activity of the reference sources; A = activity of that reference source on the measurement data; λ= the decay constant of the source; t = the elapsed time; $t_{1/2}$ = half-life of the radioactive source [12].

The efficiency standardization curve was made using different energy peaks covering the range from $60\,keV$ to $2000\,keV$ to obtain the efficiency of the detector for the particular gamma ray energy of interest. The efficiency of the $HPGe$ detector for a particular reference source of particular gamma ray energy can be found from the following equation [12, 13].

$$\varepsilon = \frac{N(cps)}{p_\gamma \times A_{ref}} \times 10^4 \quad \text{.....(ii)}$$

Where, ε = efficiency; $N\,(cps)$ = net count per second; p_γ= the fraction of a particular gamma-rayenergy and A_{ref}= activity of that reference source on the measurement date. The calculation oftheconcentration of different radionuclides is based on the measured detector efficiency as a function of energy as in Fig. 3 for the same counting geometry and time.

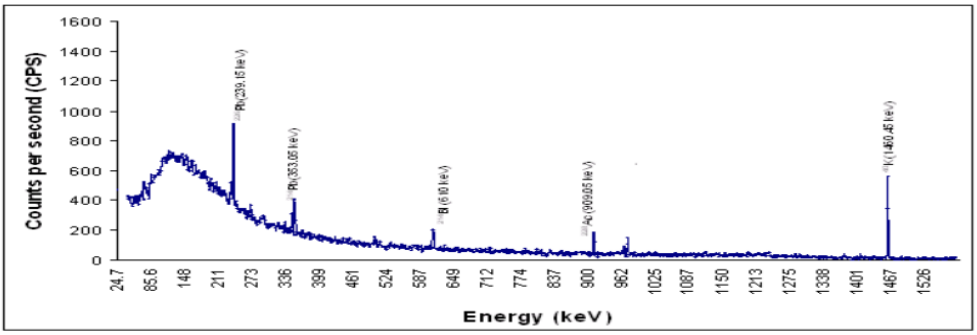

Fig 2. Gamma spectrum for a vegetable sample [12].

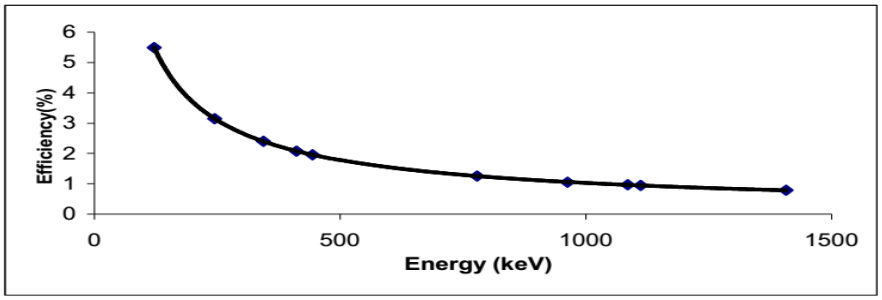

Fig. 3. Energy vs efficiency curve [12].

2.3 Data analysis

2.3.1 Activity calculation

The radioactivity concentration in the environmental samples is found by the following equation,

$$A = \frac{N(cps)}{p_\gamma \times \varepsilon \times w} \times 10^4 \dots\dots\dots\dots\dots\dots\dots\dots\dots\dots\dots\dots\dots\dots\text{(iii)}$$

Where, A = activity of the radionuclide in $Bq\ kg^{-1}$ present in the samples; $N\ (cps)$ = Net count per second; p_γ = the fraction of a particular gamma-ray energy; ε = efficiency of the detector for a particular gamma-ray energy and w = mass of sample in kilogram [12].

2.3.2 Lower Limit of Detection (LLD)

An accepted expression for LLD is given by,

$$LLD = \frac{4.66}{p_\gamma \times \varepsilon} \times S_b \dots\dots\dots\dots\dots\dots\dots\dots\dots\dots\dots\dots\dots\dots (iv)$$

Where, S_b = the standard error of the net count rate; ε = the counting efficiency of the detector for the particular gamma ray energy emitted from the particular radionuclides and p_γ = the fraction of gamma ray intensity at the particular energy [12].

3. RESULTS AND DISCUSSION

3.1 Radioactivity of ^{238}U, ^{232}Th and ^{40}K in vegetable samples of Rangpur & Rajshahi division

The Radioactivity level of ^{238}Uand ^{232}Th in each vegetable samples are shown in Table 1.The radionuclide concentrations in vegetable samples varied from 21.47 ± 0.85 *to* $61.99 \pm 5.11\ Bq\ kg^{-1}$with average $36.53\ Bq\ kg^{-1}$for ^{238}U; from 3.08 ± 0.07 *to* $7.54 \pm 0.61\ Bq\ kg^{-1}$ with average $5.54\ Bq\ kg^{-1}$for ^{232}Th,artificial radionuclide, ^{137}Cs activity is not detected at any of the sample in this research. The maximum activity of ^{238}U is found in the sample Cabbage and the maximum activity of^{232}Th is found in Asparagus. The minimum activity of ^{238}U and ^{232}Th are found in the vegetable samples Leaf amaranth and Spinach respectively.

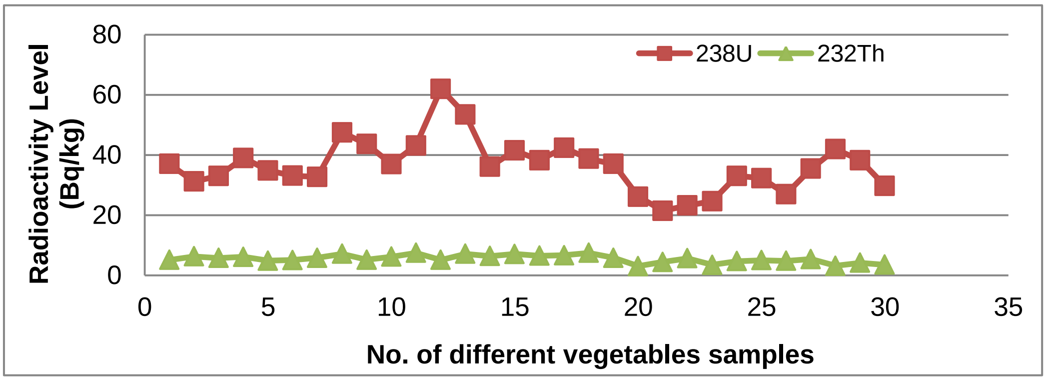

Fig. 4. Radioactivity level in different vegetable samples.

Table 1: Radioactivity level of ^{238}**U**, ^{232}**Th** and ^{40}**K** in vegetable samples

Sl. No.	Name of Vegetables	Scientific name of Vegetables	Radioactivity levels in Bqkg^{-1}		
			^{238}U	^{232}Th	^{40}K
1	Tannia	*Xanthosomaviolaceum*	37.09 ± 1.06	5.15 ± 0.98	355 ± 21.23
2	Jute leaf	*Corchoruscapsularies*	31.25 ± 2.54	6.33 ± 0.08	428 ± 32.45
3	String Bean	*Vignasesquipedalis*	33.10 ± 1.99	5.81 ± 0. 73	433 ± 25.87
4	Radish	*Raphanussativus*	39.03 ± 0.89	6.12 ± 0.81	416 ± 22.11
5	Carrot	*Daucuscarota*	44.09 ±2.12	4.89 ± 0.09	389 ± 37.06
6	Drumstick	*Moringaoleifera*	33.12± 0.87	5.11 ± 0.07	475 ± 29.09
7	Cauliflower	*Brassica oleracea var botrytis*	32.76± 0.74	5.89 ± 0.11	490 ± 29.11
8	Asparagus	*Asparagus officinalis*	47.56 ± 3.33	7.21 ± 0. 07	417 ± 35.32
9	White yam	*Dioscoreaalata*	43.67± 2.91	5.24 ± 0.08	407 ± 19.12
10	Plantain	*Musa paradisiaca*	37.01 ± 3.03	6.23 ± 0.14	445 ± 28.01
11	Brinjal	*Solanummelongena*	43.18 ± 1.09	7.49 ± 0.76	507 ± 16.56
12	Cabbage	*Brassica oleracea var capitata*	61. 99 ± 5.11	5.19 ± 0.95	471 ± 11.87
13	Bottle gourd	*Lagenariasiceraria*	53.44 ± 4.43	7.21 ± 0.91	409 ± 25.62
14	Bunching onion	*Allium fistulosum*	36.15 ± 3.77	6.47 ± 0.19	375 ± 47.23
15	Green papaya	*Carica papaya*	41.56 ± 3.47	7.12 ± 0.08	487 ± 37.34
16	Sweet gourd	*Cucurbita maxima*	38.29± 3.22	6.57 ± 0.78	509 ± 19.97
17	Sweet potato	*Ipomoea batatus*	42.43 ± 4.22	6.73 ± 0.55	417 ± 18.47
18	Water spinach	*Ipomoea aquatica*	38.76± 3.47	7.54± 0.61	436 ± 27.23
19	Baby corn	*Zea mays var. saccharata*	37.08 ± 4. 92	5.89 ± 0.08	346 ± 21.64
20	Spinach	*Ipomoea aquatica*	26.17± 3.56	3.08 ± 0.54	317 ± 27.99
21	Leaf amaranth	*Amaranthusviridis*	21.47 ± 0. 85	4.46 ± 0.07	327 ± 17.54
22	Water lily	*Nymphaea stellata*	23.24 ± 0.99	5.69 ± 0.09	306 ± 16.23
23	Stem amaranth	*Amaranthus lividus*	24.69± 0.76	3.55 ± 0.06	355 ± 27.43
24	Sweet gourd	*Cucurbita maxima*	33.06± 0.64	4.75 ± 0.79	435 ± 33.76
25	Pea	*Pisum sativum*	32.21± 2.54	5.06 ± 0.98	385 ±33.19
26	Potato	*Solanum tuberosum*	27.05 ± 2. 42	4.84 ± 0.34	408 ± 28.05
27	Cucumber	*Cucumis sativus*	35.47 ± 0. 93	5.46 ± 0.78	426 ± 31.04
28	Tomato	*Lycopersicon esculentum*	41.97 ± 2. 55	3.21 ± 0.09	329 ± 27. 98
29	Turnip	*Brassica rapa*	38.29 ± 1.91	4.23 ± 0.07	385 ± 37.99
30	Hyacinth bean	*Lablab niger*	29.81± 3.18	3.59 ± 0.95	312 ± 22.44

From the Fig.4, it is shown that the radioactivity levels of ^{238}U in all the vegetable samples are within the range $20\ to\ 700\ Bqkg^{-1}$and the radioactivity levels of ^{232}Th in all the vegetable samples are within the range $0\ to\ 10\ Bqkg^{-1}$. These values are lower than the values suggested by the $UNSCEAR$ for vegetables for the whole world [9]. It is also found that the average

radioactivity level of ^{238}U in measured vegetable samples is 8.71 times lower than world average value. Similarly the average radioactivity level of ^{232}Th in measured vegetable samples is 9.57 times lower than world average value. A comparison of average radioactivity level ($Bqkg^{-1}$) of the natural radionuclides in vegetable samples with the results of the present study is given in Table 2.

Table 2. Comparison of activity concentration ($Bqkg^{-1}$) of natural radionuclides in vegetables

Reference	Region	^{238}U	^{232}Th
UNSCEAR[5]	World Average	318	53
Present Study	Bangladesh	36.53	5.54

The uptake of radionuclides by vegetables from the soil into vegetables is highly complex and depends on several factors including vegetables species, soil conditions, the concentration of radionuclides in soil and the radionuclides availability in soil [14]. As ICRP (1999), the extra use of phosphate fertilizer may be a factor causing the increase of Radium radionuclide concentration in the vegetables samples [15].

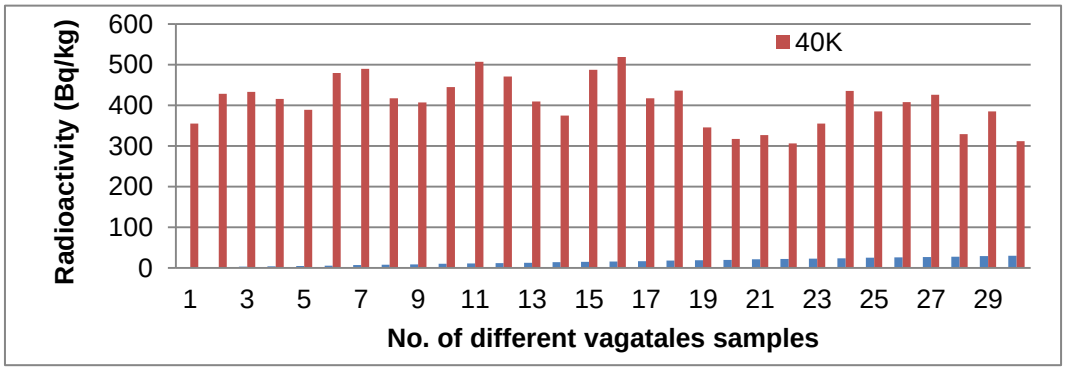

Fig. 5. The radioactivity levels of ^{40}K in different vegetables sample.

Among all the natural radioisotopes in the present study, the concentration of ^{40}K has the highest value. Similar findings have been published by the other authors [16, 17]. This may be due to the concentration of ^{40}K in the soil is high and higher transfer factor of ^{40}K than other natural radioisotopes [18]. However, ^{40}K is an essential biological element and its concentration in human tissue is under close metabolic control [19]. The activity concentration of ^{40}K in vegetable samples ranged from $306 \pm 16.23\ Bqkg^{-1}$ to $519 \pm 43.17\ Bqkg^{-1}$ with average activity $407\ Bqkg^{-1}$. As shown in Table 1, the present study revealed that the maximum activity of ^{40}K in vegetable samples is $519 \pm 43.17\ Bqkg^{-1}$, which is found in the vegetable sample Pea. The minimum

activity of ^{40}K in vegetable samples is $306 \pm 16.23\, Bqkg^{-1}$, which is found in the vegetable sample Water lily. This higher activity of ^{40}K might be attributed to the higher biological requirement of vegetables for potassium as it is a major essential nutrient elementFig. 5 shows the radioactivity levels of ^{40}K in different vegetables sample.

3.2 Dose Estimates

The annual effective dose was calculated using mean concentration of radionuclide in Bqkg-1, annual consumption rate and dose coefficient using the equation ,

$$E = C \times I \times D \ldots\ldots\ldots\ldots\ldots\ldots\ldots\ldots\ldots\ldots\ldots\ldots\ldots\ldots\ldots\ldots\ldots\ldots.. (v)$$

Where, E= Annual Effective Dose (Svy^{-1}); C= Concentration of radionuclide ($Bqkg^{-1}$); I= Annual consumption (kgy^{-1}) and D =Dose coefficient ($Sv\, Bq^{-1}$) [12].

The dose coefficient were $4.5 \times 10^{-8}\, Sv\, Bq^{-1}\, for\ ^{238}U, 2.3 \times 10^{-7} Sv\, Bq^{-1}$ for ^{232}Th and $6.2 \times 10^{-8} Sv\, Bq^{-1}$ for ^{40}K [20]. The annual consumption rate of vegetable in Bangladesh is calculated to be $60.59\, kgy^{-1}$. The annual effective dose due to each radionuclide is shown in Table 3.

Table 3: Average activity concentration and annual effective dose of different radionuclides due to consumption of vegetables by population of Bangladesh

Radionuclide	Average Radioactivity Level in $Bqkg^{-1}$	Annual Effective Dose in mSv
^{238}U	36.53	0.0996
^{232}Th	5.54	0.0772
^{40}K	407	0.153

The estimated total annual effective dose for the ingestion of different vegetable samples and their derived products with the long lived natural radionuclides is found to be $0.329\, mSvy^{-1}$, which is 1.134 times higher than the total exposure per person resulting from ingestion of terrestrial radioisotopes $0.29\, mSvy^{-1}$ as proposed by $UNSCEAR$. ^{40}K contributed the highest value to the total annual effective dose. The estimated total annual effective dose received from long lived natural radionuclides ^{238}U and ^{232}Th in daily ingestion of vegetable samples which is $0.176\, mSvy^{-1}$ and lower than the total exposure per person resulting from ingestion of terrestrial radioisotopes $0.29\, mSvy^{-1}$ as proposed by $UNSCEAR$.It is also found that the annual effective dose due to the ingestion of vegetables and their derived products with the long lived natural radionuclide is higher than daily ingestion of ^{232}Th, ^{238}U, ^{228}Ra and ^{210}Pb in vegetables by inhabitants of Rio de Janeiro city, which is $0.0145\, mSvy^{-1}$[9]. From the present study, it comprised 0.0304 % of the annual dose limit of 1mSvy^{-1}for general public [21]. The annual effective dose resulting from the studied radionuclides for the adult population in Bangladesh are found to be safe. Food is indispensable to human life, thus an important parameter of environmental science. The presence of radionuclides in vegetable samples poses a number of health hazards, especially when these radionuclides are deposited in the human body, through ingestion. The main objective of this study is to determine the radioactivity concentration of gamma emitting radionuclides e.g. ^{238}U, ^{232}Th, ^{40}K in vegetable samples. An investigation of this

nature is useful for both the assessment of public dose rates and the performance of epidemiological studies. Also, maintaining reference-data records will assist in ascertaining possible changes in environmental radioactivity due to nuclear, industrial, and other human activities.

5. CONCLUSIONS

The radioactivity concentration of different gamma emitting radionuclides e.g. ^{238}U, ^{232}Th and ^{40}K in different vegetable sample which is collected from Rangpur and Rajshahi Division in Northern part of Bangladesh analyzed in this study to establish a baseline data for the activity level of the radionuclides. The estimated total annual effective dose for the ingestion of different vegetable samples and their derived products with the long lived natural radionuclides is found to be $0.329 mSvy^{-1}$, which is 1.134 times higher than the total exposure per person resulting from ingestion of terrestrial radioisotopes 0.29 $mSvy^{-1}$ as proposed by UNSCEAR. Though, it is higher than daily ingestion of ^{232}Th, ^{238}U, ^{228}Ra and ^{210}Pb in vegetables by inhabitants of Rio de Janeiro city, which is $0.0145 mSv\ y^{-1}$. ^{40}K contributed the highest value to the total annual effective dose. The estimated total annual effective dose received from long lived natural radionuclides ^{238}U and ^{232}Th in daily ingestion of vegetable samples which is$0.176 mSvy^{-1}$ and lower than the total exposure per person resulting from ingestion of terrestrial radioisotopes 0.29 $mSvy^{-1}$ as proposed by UNSCEAR. The presence of radionuclides in vegetable samples poses a number of health hazards, especially when these radionuclides are deposited in the human body, through ingestion. According to ICRP Protection of the public in situations of prolonged radiation exposure annual dose limit for general public$1 mSvy^{-1}$. The annual effective dose resulting from the studied radionuclides for the adult population (above or equal of 18years) in Bangladesh are found to be safe. So, we can say that though, three long lived natural radionuclides are found in the collected vegetable samples but their total estimated effective dose is lower than the total exposure per person resulting from ingestion of terrestrial radioisotopes. So, these vegetables are still safer for the human health but we have to keep proper monitoring in near future. The future plan of this research is that this type of experiment will be exercised for measuring radioactivity level of different types of radionuclides in vegetables from all other parts of the Bangladesh.

REFERENCES

[1] M. Donya, M. Radford, A. ElGuindy, D. Firmin and M. H. Yacoub , Radiation in medicine: Origins, risks and aspirations, Glob Cardiol Sci Pract, **2014**(4); 437–448.

[2] D. Kyne and B. Bolin, Emerging Environmental Justice Issues in Nuclear Power and Radioactive Contamination, Int J Environ Res Public Health, 2016 Jul; **13**(7): 700.

[3] H. Liesel,Environmental Radioactivity Monitoring in Australia, Technical Report, 2005, Series **143**, pp 23.

[4] M. B. Tavakoli, E. Kodamoradi and Z. Shaneh, Assessment of gamma-dose rate in city of Kermanshah, J Educ Health Promot. 2012, **1**: 30.

[5] UNSCEAR, 1972, Ionizing Radiation Levels and Effects, A Report of the United Nations Scientific Committee (General Assembly) USA.

[6] United Nation sales publication E.82.IX.8. New-York: United Nations; 1982, UNSCEAR. Ionizing radiation: Sources and Biological effects, United Nations scientific committee on the effects of atomic radiation, 1982 Report to the general assembly with annexes.

[7] M. Thorne, Background radiation: natural and man-made, J. of Radiological Protection, 2003, **23**(1), pp 29.

[8] D. N. Avadhani., N. Karunakaea., H. M. Mahesh, Y. Narayana, H. M. Somashekarappa, K. Siddappa, Distribution and enrichment of ^{210}Poin the environment of Kaiga in South India Environmental Radioactivity, 2000, **51**(3),pp 349-362.

[9] UNSCEAR Sources and effects of ionizing radiation, A Report to the general assembly with scientific annexes (New York: United Nations) (2000).

[10] E. Santos, E. D. C. Lauria, E. C. S. Amaral, E. E. R. Rochedo,Daily ingestion of Th-232, U-238, Ra-228 and Pb-210 in vegetables by inhabitants of Riode Janeiro city, J. Envir. Radiocat., 2002, **62**(1), pp 75-86.

[11] F. P. Banzi,L. D. Kifanga,F. M. Bundala, Natural radioactivity and radiation exposure at the Minjinguphosphatemine in Tanzania J.Radiat. Prot.2041–2051, 2000

[12] M. J. Ferdous, S. Ahmed, A. Begum and Amena Begum, Measurement of ^{238}U, ^{232}Th, ^{228}Ra, ^{226}Ra and ^{40}K Activities In Vegetable Samples And Dose Assessment For Adult Population Of Bangladesh, Bangladesh Journal of Physics, **13**, 65-75, 2013

[13] G. F. Knoll., Radiation Detection and Measurement, 2nd Edition (USA: John Wileyand Sons), 1989.

[14] M. Asefi, M. M. Beitollahi, M. Ghiassi-Nejad, F. Reza-Nejad, Exposure to ^{226}Ra from consumption of vegetables in the high level natural radiation area of Ramsar, Iran Journal of Environmental Radioactivity, 2003, **66**(3), pp 215-225.

[15] ICRP Protection of the public in situations of prolonged radiation exposure, ICRP Publication 82,(Oxford: Pergamon Press) (1999).

[16] A. Catalan, J. C. Fernandez-Aldecoa, J. Hernandez-Armas, F. Hernandez, M. I. Landeras, Activity concentrations and mean annual effective dose of foodstuffs on the island of Tenerife, Spain Radiiation Protection Dosimetry, **111**, 2004, pp 205 -210.

[17] M. S. Choi,X. J. Lin, S. A. Lee, W. Kim, H. D. Kang, S. H. Doh, D.S. Kim, D. M. Lee, Daily intakes of naturally occurring radionuclides in typical Korean foods. Journal of EnvironmentalRadioactivity, **99**, 2008, pp 1319-1323.

[18] Derivation of activity concentration values exclusion, exemption and clearance, In. Safety Report Series 2005, IAEA 44, pp 1020.

[19] UNSCEAR Ionizing Radiation, Sources and biological effects, United Nations Scientific Committee on the effect of atomic radiation, United Nations, New York (1982).

[20] ICRP Protection of the public in situations of prolonged radiation exposure. ICRP Publication ICRP 68,(Oxford: Pergamon Press) (1994).

[21] IAEA International basic safety standards for protection against ionizing radiation and for the safety of radiation sources: Safety Series 115, IAEA (1996).

*Bangladesh Journal of Physics, **23 & 24**, 51-64, 2018*

LANDSLIDE SUSCEPTIBILITY ASSESSMENT BASED ON SATELLITE IMAGE PROCESSING AND BI-VARIATE STATISTICAL MODELING FOR RANGAMATI DISTRICT, BANGLADESH

DEWAN MOHAMMAD ENAMUL HAQUE[1], SHAMIM AFERDOUSI SIFA[1], TONOY MAHMUD[1] AND MARIA ABDULLAH TARIN[1]

[1]*Department of Disaster Science and Management, University of Dhaka, Dhaka-1000, Bangladesh*

[*]*Corresponding author: E-mail: dewan.dsm@du.ac.bd*

Received on 10.04.2018, Revised received on 11.07.2018, Accepted for Publication on 01.09.2018

ABSTRACT

Landslide susceptibility assessment has been performed based on 2017 landslide events in Rangamati district using the weight of evidence (woe) bivariate statistical method to identify the possible susceptible areas for future landslide occurrence. A number of landslide triggering factor maps are combined with the location of previous landslides (inventory). Landslide triggering factors such as rainfall, slope angle, slope aspect, vegetation, land use, geology, elevation, distance from the drainage and road are taken into consideration based on hazard analysis. These factor maps and landslide inventory have been derived from the satellite image processing. The offset tracking of synthetic aperture radar (SAR) images and the sub-pixel correlation of optical satellite imagery techniques were applied to prepare the inventory. These techniques utilize phase correlation and normalized cross-correlation (NCC) respectively. Finally, the landslide susceptibility information has been retrieved from the conditional probability of previous landslide occurrence on the areas of triggering factors. The landslide susceptibility map has been validated from the success rate curve plotting the percentage of landslide susceptibility index rank against the percentage of cumulative landslide occurrence. About 20% of the highly susceptible areas include 84% of the total landslide area and 30% of the highly susceptible area covers more than 99% of the total landslide areas. The study was carried out in Kawkhali, Rajasthali, kaptai, and Rangamati Sadar upazilla, among which Rangamati Sadar has been identified as the most landslide hazard-prone upazilla as 44% of its area are highly susceptible to landslide occurrence.

1. INTRODUCTION

Landslide is a common geological hazard in Bangladesh and it poses a significant threat to development [1]. However, the devastating impact of the landslides can be reduced by taking appropriate mitigation measures after identifying the susceptible hazardous areas. Landslide susceptibility mapping involves the determination of the spatial extent of a particular type of landslides, its volume, and the probability of its occurrence over a period of time and space [2], [3]. After the recent landslide occurrence of 2017, landslide susceptibility mapping of the Rangamati district has become indispensable to identify the future landslide hazard-prone areas. Rangamati, which is well known as indigenous hilly district [4] suffered highest negative consequences in its history, as the disaster claimed lives of 152 people in total, severely destroying 6,000 dwellings, roads, telecommunication system, and power supply, along with an economic loss of about USD 223 million [5]. This massive devastating event caused the slope to become unstable. As the area which has already suffered from landslides has the probability of suffering landslides again, last year's landslide events in Rangamati indicate the great threat of landslide occurrence in the future. Considering the lack of studies about landslides in that area, this area (Fig. 1) was a prime choice for producing a landslide susceptibility map.

Landslide susceptibility maps can be produced following both the quantitative and qualitative approach [6]. Qualitative maps, which is derived from landslide inventory and knowledge-driven methods, shows zoning of hazard-prone areas into different categories using descriptive terms (high, moderate, low) [7]. On the other hand, data-driven, probabilistic and deterministic methods are the quantitative methods to produce susceptibility maps. They employ computer models, programming and geospatial technologies to quantify the severity of the possible landslide areas [8]. Among quantitative methods, heuristic, statistical probabilistic and deterministic models are the most common.

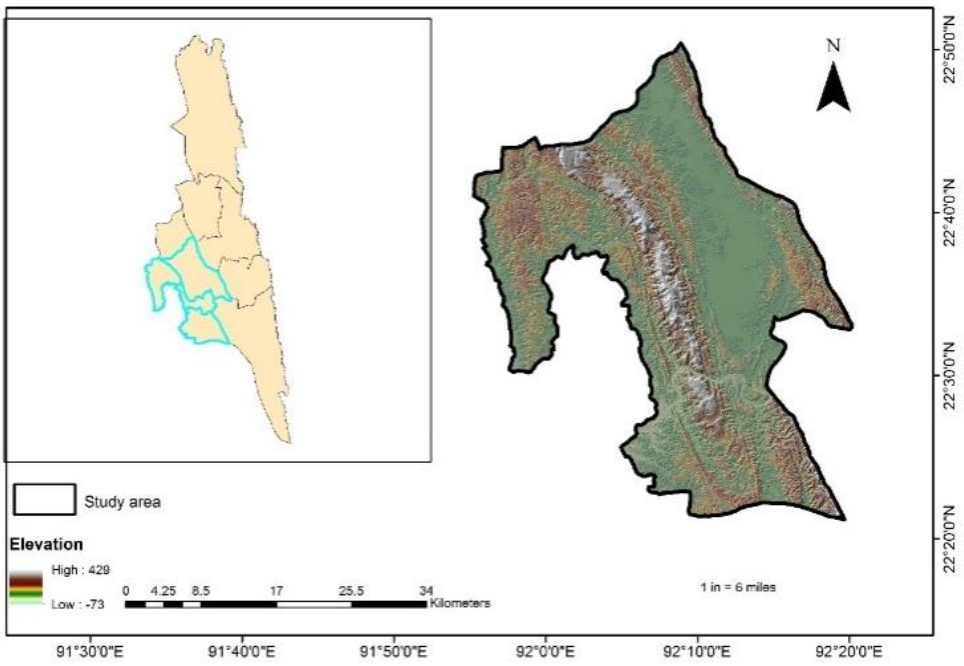

Fig. 1. The four Upazilla, Rangamati Sadar, Rajasthali, Kaptai and Kawkhali of Rnagamati District were chosen as the study area.

Despite being a complex process, the statistical analysis predicts the possible spatial distribution of landslides with high accuracy and validation rates [9], [10]. Most commonly used methods of statistical analysis, are multivariate and bivariate statistical analysis [11]. Bivariate statistics process is based on calculating locations of the previous landslides (inventory) [12] with the factor maps. All the landslide triggering factor maps can be categorized, overlaid and weighted [13] using some of the methods such as information value method, weight-of-evidence modeling [14] and landslide nominal susceptibility factor (LNSF) etc. [15]. Among other statistical-probabilistic approaches, weights-of-evidence (WoE) has been used due to the simplicity and higher accuracy of the process [16], [17]. This process is also effective in dealing with a large region with the heterogeneous ground condition.

The bivariate statistical modeling combines the landslide inventory with landslide triggering factor maps. There exist multiple in-situ approaches for the generation of landslide inventory. However,

earth observation techniques are more convenient and capable of accurately investigate the whole area. Among other earth observation methods, the combination of offset tracking of synthetic aperture radar (SAR) images and subpixel correlation of optical imagery were employed. The offset track provided the spatial extent of the landslides and the sub-pixel correlation provided the direction of landslide displacement. Multiple factor maps based on detail hazard analysis have also been produced from satellite image processing.

2. DATA AND METHODOLOGY

Landslide hazard analysis results show the association of different factor classes with the previous landslides. With the help of available high-resolution DEM and SAR offset tracking and optical image sub-pixel correlation, 420 landslide events have been identified and mapped. This past landslide occurrence, which causes the slope to become unstable, has the potentiality to cause future landslide in the presence of similar conditioning factors based on an assumption that "past and present are keys to the future". A bivariate statistical probabilistic approach known as weights of evidence was used to determine the susceptible areas and carry out the hazard assessment. In this method, the prior and conditional probability was used to assign weights to each class of the triggering factors and determine the degree of correlation and spatial relationships of the factors in causing landslide hazard. Later, the results were validated from the gradient of the susceptibility index rank and cumulative landslide occurrence curve.

A number of earth observation data were used for factor map creation and inventory production. Offset tracking employed to two SAR single look complex (SLC) images sensed on 6 June 2017 and 18 June 2017, which gave a 12 days window. The pixel size of the images is 10 meter. For sub-pixel correlation, ASTER images were used. The acquisition date of the pre-event image is 18th March and post-event is 2015 to 2nd January 2017. The VNIR 3N band was utilized for analysis. To produce the factor maps, 12.5m ALOS PALSAR digital elevation model and 30 meters Landsat 8 optical images were used. The rainfall data is collected from the Bangladesh Meteorological Department.

2.1 Weight of evidence model

In this method, WoE, the prior probability is calculated based on past landslides. It assumes that it will trigger future hazardous event due to the unstable nature of the slope. When additional information about the factors are not available, prior probability give a good estimation about the possibility of landslide occurrence by dividing the number of pixels having landslides with a total number of pixels in the map [18].

$$\text{Pprior} = \text{P}\{\text{S}\} = \frac{\text{Area(Slide)}}{\text{Area (Total)}}$$

However, when information such as presence or extent of causal factors of landslides is available, then the prior probability is further modified to obtain a conditional probability. This is done by producing a binary map ~~(B)~~ for that particular factor depending on the presence and absence of the variable in the map. A relationship is then established between the binary maps with the landslide inventory, to calculate the conditional probability for a certain condition. According to [18], the

factors are conditionally independent of each other, and the conditional probability of occurring a landslide given that a particular landslide triggering factor is present is expressed is thereby expressed as:

$$P\{S|B\} = \frac{P\{S \cap B\}}{P\{B\}}$$

$$= \frac{Npix\{S \cap B\}}{Npix\{B\}}$$

In the equation, S and B denote landslide and factor variables respectively. Pixel area in each map is used in the analysis to find out the four possible combinations of probability (Fig. 2). Which are; when landslides occur in presence of a potential conditioning factor (Npix1) or absence of it (Npix2) when there is no landslide in the map area but the factor is present (Npix3) and absence of both landslide and that particular factor (NPix4). This is obtained by crossing the inventory of landslides with each factor map to calculate:

$$Npix1 = nslclass$$

$$Npix2 = nslide - nslclass$$

$$Npix3 = nclass - nslclass$$

$$Npix4 = nmap - nslide - nclass + nslclass$$

The above variables thereby mean
nslide =Number of pixels with landslides in the map
nclass= Number of pixels in the class
nslclass= Number of pixels with landslides in the class
nmap= Total number of pixels in the map

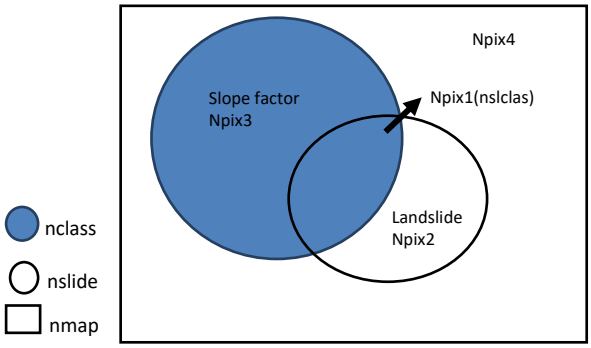

Fig. 2. Principle of Weight of Evidence model.

Both positive and negative weighted values of each variable are then estimated to find a degree of correlation in the presence or absence of the factor using the formula describes by [19], [20]:

$$W^{+} = \ln\left(\frac{P\{B|S\}}{\{B|\bar{S}\}}\right)$$

$$W^{+} = \ln((Npix1 * (Npix3 + Npix4)/((Npix1 + Npix2) * Npix3)$$

$$W^{-} = \ln\left(\frac{P\{\bar{B}|S\}}{\{\bar{B}|\bar{L}\}}\right)$$

$$W^{-} = \ln((Npix2 * (Npix3 + Npix4)/((Npix1 + Npix2) * Npix4)$$

In presence of factor (B) in landslide areas (S) gives a positive weighted value (W^{+}), defining the correlation between them. On the other hand, a negative weight (W^{-}) indicates the absence of the factor. Then a Weighted Contrast factor (C) is obtained to see how much the conditioning factor is spatially associated with the landslides. A final susceptibility map (LSI) hence, is produced by combining the weighted map of each factor through an overlay operation.

$$C = W^{+} - W^{-}$$

$$Wmap = W^{+} - W^{-} + \Sigma W^{-}$$

$$LSI = \Sigma Wmap$$

Form the above methodology it's transparent that the WOE necessitates landslide inventories and landslide triggering factor maps.

2.2 Landslide inventory preparation

Inventory is one of the two types of input needed for Weights of Evidence model to work. The location of the previous landslides was determined by offset tracking and the direction of those landslides was drawn from the sub-pixel correlation of optical imagery.

Optical Image Sub-pixel Correlation Technique

Subpixel correlation uses phase correlation based on furrier shift theorem [21]. It tends to give better and more robust results than traditional cross-correlation [22], [23]. It is performed on both spatial and frequency domain [24]. The difference in phase indicates a relative displacement between two similar overlapping images and that displacement can be derivative of the phase difference of Fourier transform (Leprince et al., 2007). [21], [25] mentioned the equation for correlation.

Let i_1 and i_2 be two images that differ only by a displacement (Δx, Δy) such that

$$i_2(x, y) = i_1(x - \Delta_x, y - \Delta_y)$$

Let us denote I_1 and I_2 as their Fourier transform from Fourier shift theorem. This brings us the relation

$$I_2(\omega_x, \omega_y) = I_1(\omega_x, \omega_y) e^{-j(\omega x \Delta x + \omega y \Delta y)}$$

In the above relation ω_x and ω_y is the frequency variables for column and row i.e. amplitude of respective frequencies in x and y-direction. The normalized cross spectrum of the images i_1 and i_2 relation is

$$C_{i_1 i_2}(\omega x, \omega y) = \frac{I_1(\omega x, \omega y) I_2^*(\omega x, \omega y)}{I_1(\omega x, \omega y) I_2^*(\omega x, \omega y)} = e^{j(\omega x \Delta x + \omega y \Delta y)}$$

The relative displacement based on Fourier shift theorem can be obtained by

$$F^{-1}\{e^{j(\omega x \Delta x + \omega y \Delta y)}\} = \sigma(x + \Delta_x, y + \Delta_y)$$

The subpixel correlation can achieve an accuracy of the $1/20^{th}$ pixel as it does not require any in situ information like GPS measurement [25]. This method only depends on the topographic data and the satellite ancillary data.

SAR Offset Tracking Technique

Offset tracking provides displacement information parallel to SAR satellite track (Azimuth offset) and the track perpendicular (range offset) [26]. The window patch intensity is measured to find the motion or displacement between two images of the same area [27]. First, the master (pre-event) and slave image (post-event) are co-registered using a Digital Elevation Model (DEM). Afterward, to calculate the offset, a Ground Control Point (GCP) grid is specified for the master image. The displacement is measured by matching frequency peaks of a patch of pixels in master and slave image. If two corresponding window gives the same frequency peaks, they are considered stable [28]. Each applied to offset a correlation value is computed, thus permitting calculation of the corresponding matching correlation surface (MCS), whose ith and jth element for the generic pixel of range and azimuth coordinates (x, y) is the following: [29], [30].

$$MCS(i,j) = \frac{\sigma MS_{i,j}}{\sigma M \sigma S_{i,j}}$$

Where

$$\sigma_M = \sqrt{\frac{\sum_{x=1,y=1}^{X,Y} |M(x,y)|^2}{XY} - \mu_M^2}$$

$$\sigma S_{i,j} = \sqrt{\frac{\sum_{x=1,y=1}^{X,Y} |S(x+i, y+j)|^2}{XY} - \mu_{S_{i,j}}^2}$$

are the standard deviation values for the master and slave amplitude images, respectively, computed on the matching window pixels. The normalized cross-correlation between the master and slave image amplitudes is computed. This gives the quality of the calculation.

$$NCC = \frac{\sum_{i=1}^{i_x} \sum_{j=1}^{j_y} [(i_1(i,j) - \overline{i_1}).(i_2(i,j) - \overline{i_2}]}{\sqrt{\sum_{i=1}^{i_x} \sum_{j=1}^{j_y} (i_1(i,j) - \overline{i_1})^2} \sqrt{\sum_{i=1}^{i_x} \sum_{j=1}^{j_y} (i_2(i,j) - \overline{i_2})^2}}$$

The study faced a limitation in inventory production as the freely available SAR image utilizes C band (5-6cm) wavelength. It is hard for C band wavelength to penetrate vegetation cover, resulting in some decorrelation.

2.3 Landslide triggering factor map preparation

Factor maps were produced from high-resolution Digital Elevation Model (DEM) and Optical image analysis. The DEM is of 12.5meter resolution and is acquired from ALOS PALSAR Satellite. Slope and aspect maps were prepared from elevation difference using DEM. Slope values for each cell from the raster DEM were calculated using the surface tool in Arc map which uses the average maximum technique. The slope represents the maximum rate of change in elevation which can be expressed either as a percent of slope or degree of slope. Here, the slope values have been represented as the degree of slope. Slope aspect is the direction or azimuth of the slope where the rate of change of altitude is maximum (true gradient) with respect to the north [31] and is thereby derived from DEM. The value of each cell in the aspect dataset represents the direction of the slope of that cell. Aspect is measured clockwise and in degrees ranging from zero (due north) to 360 (again due north). Flat areas are assigned value -1 as they have no downslope direction. Amount of vegetation cover (biomass or canopy) in the study area is determined by using Normalized Difference Vegetation Index (NDVI) method which involves consideration of the difference between band 5 (infra-red) and band 4 (red) of Landsat 8 image. The spectral reflectance curve for vegetation [32] shows that the maximum absorption by the chlorophyll pigment in the plant is in the range of 0.636 to 0.673 micrometer (red band), whereas the leaf structure highly reflect infra-red wave having a wavelength of range 0.51-0.879 micrometers [33]. Land use and land cover classification maps were also produced from Optical image analysis using Maximum Likelihood algorithm based supervised classification tool, which involves the process of converting multi-band raster imagery into a single band raster with several categorical classes to represent different land covers. Four major classes have been identified- waterbody, vegetation cover, bare land and built up the area by compositing the bands 4, 3 and 2 as these three bands are visible in the EM spectrum and easily differentiate objects. Distance from waterbodies and distance from roads were shown in maps, which have been produced by digitizing waterbodies from GeoEye satellite image provided by ESRI. Annual average rainfall is computed from the available data acquired from the Bangladesh Meteorological Department and the calculated value is used to estimate rainfall values in other regions of the study area based on the elevation [34]. The geological formation of the study area was digitized from the geological map of Bangladesh produced by [35]

3. RESULTS AND DISCUSSION

The factor maps which contribute to landslide occurrence and the spatial extent of the previous landslide has been produced and mapped from the satellite image processing. Hazard analysis has been carried out to define the degree of association of these landslide triggering factors with past landslides of 2017, which was summarized below in Table 1.

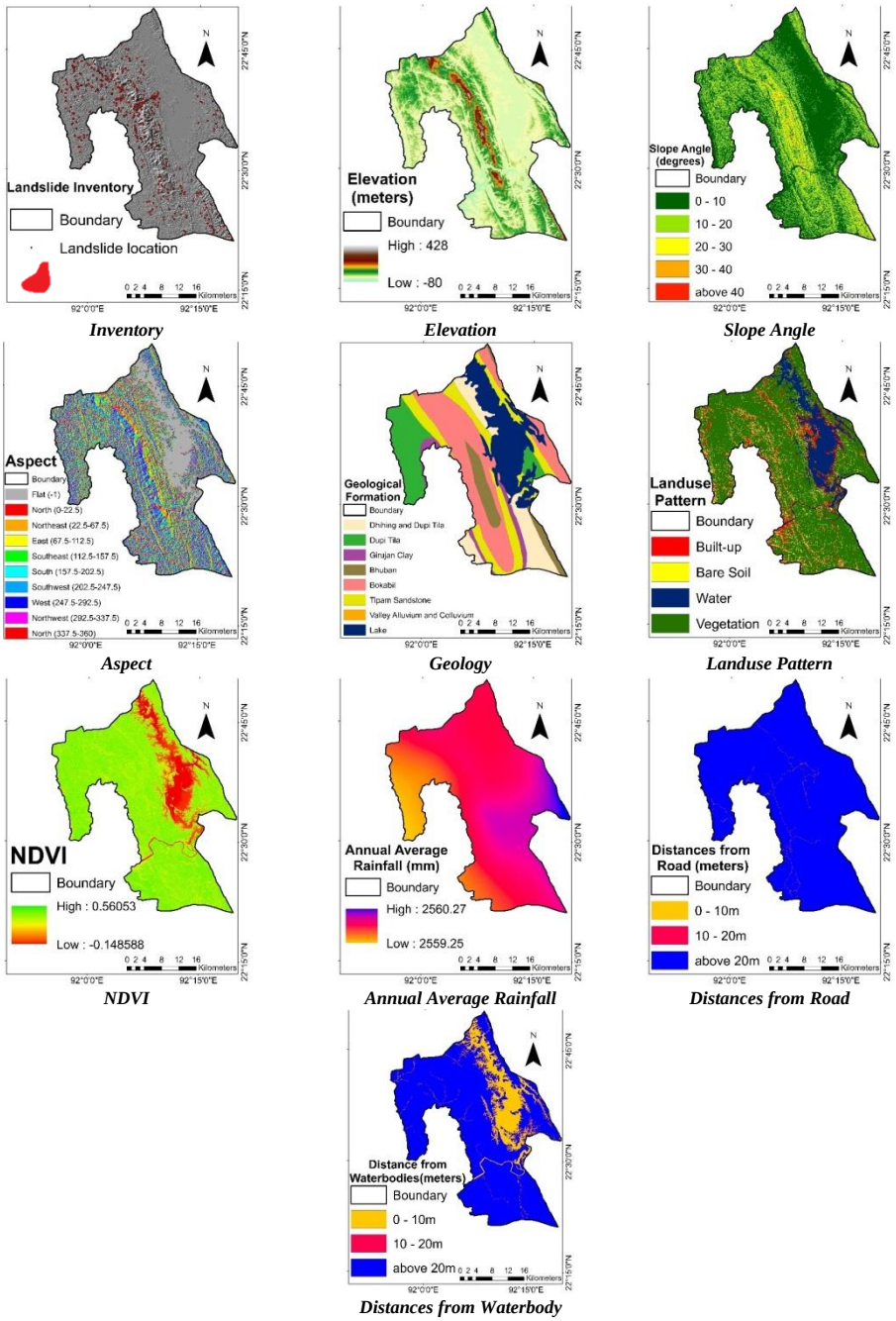

Inventory ***Elevation*** ***Slope Angle***

Aspect ***Geology*** ***Landuse Pattern***

NDVI ***Annual Average Rainfall*** ***Distances from Road***

Distances from Waterbody

Fig. 3. Landslide triggering factor maps.

Table 1: Table showing the hazard analysis results summary

Factors	**Major Findings**
Rainfall	*The threshold value 270 mm*
Slope angle	*40-45° (38% slides)*
Slope aspect	*West facing (43% slides)*
Land use	*Densely vegetated area*
Vegetation	*Shallow-rooted vegetation (indiscriminate logging)*
Geology	*Bokabil formation*
Distance from road	*2% within 10 m*
Distance from water bodies	*3% within 10 m*
Groundwater level	*Highest on the landslide day (8.20 m)*

The spatial relationship between the landslides and triggering factors (Fig. 3) such as slope, elevation, aspect, geology, waterbodies, road, vegetation, land use pattern, and most importantly rainfall has been analyzed through this research. Table 1 shows that slope greater than 40 degrees have higher susceptibility towards failing than lower slope angle. The higher is the slope gradient, the greater is the shear stress acting on the slope. The slope angle ranging between 20 to 30 degrees have a second highest probability of landslide occurrence among the other classes of slope factor. The slopes which are dominantly west facing have greater weight as they have a greater amount of precipitation. Since the area has an elevation up to 428 meters, it is also considered as a factor to find out how much the elevation is associated with landslide occurrence. It has been found that the highest elevated regions have lower susceptibility due to its compactness and resistant to weathering processes. Another reason can also be that those regions tend to be less accessible due to its greater relief and are thereby subjected to less modification. Geology of the study area is also an important factor. Bhuban and Bokabil formation have the highest susceptibility value. Both have a positive contrast factor (calculated from WoE) showing positive spatial association with a landslide. This is because there is an alteration of sandstone and shale in their lithology. Water drains out easily from the sandstone and gets interrupted by the impermeable clayey layer resulting in the decrease of friction force in the sand particles causing the layer to fail. Tipam and DupiTila formations are also present in the study area but have relatively lower susceptibility than the above formation.

In the case of Land use pattern and Vegetation Index (NDVI), both factors show that areas with higher vegetation value have a greater probability of landslide occurrence. Upper class (0.396459 - 0.56053) of Vegetation Index got higher positive weight value and the same goes for the vegetation classes of land use pattern (table 1). This indicates the influence of heavy rainfall which makes even the vegetated area unstable. Another reason can be indiscriminate logging practice. Population modified the slope and carry out agricultural activities in the slope of the hilly areas. Apart from vegetation, bare soil and built up area was also classified to determine the contribution of these land use changes in landslide occurrence. Bare soil remains exposed for a long time and are subjected to erosion and weathering processes, increasing the susceptibility to slope failure. As assumed, the regions where the built-up areas are present have been classified as high hazard prone. However, the weighted value for the built-up area is low compared to other land use classes because the extent of urbanization in the study area is still low. Distances from the road and water bodies show little correlation with landslide occurrence as few landslides occurred closer to the road or water bodies; rather the events were more distributed (Fig. 3). Rainfall is found as the most

important landslide triggering factor. Water from the rainfall increases the pore water pressure and decreases the shear strength of the soil. Moreover, runoff accelerates erosional activity and thus makes the slope susceptible to fail. In 2017, Rangamati district experienced around one-third of its annual rainfall within a five days period before the landslides. The model also found that the rainfall is exhibiting the highest weight value.

It is logical to think that instead of one single factor rather than a combination of triggering factors plays a significant role in landslide occurrence. The spatial relationship of an individual factor cannot alone describe the degree of contribution of its particular classes to landslide hazard initiation. The hazard results from the complex interaction of all these factors together, so factor classes having lower weighted value does not necessarily imply that it does not have any association with the hazard occurrence. In this respect, WoE is an important model to account for this complex interaction of all potential landslide triggering factors with the previous landslides.

The landslide susceptibility map produced from the statistical probabilistic model is given in Fig. 4 where future landslide-prone areas are quantified into high, moderate, low and very low as shown by different color representation in the map.

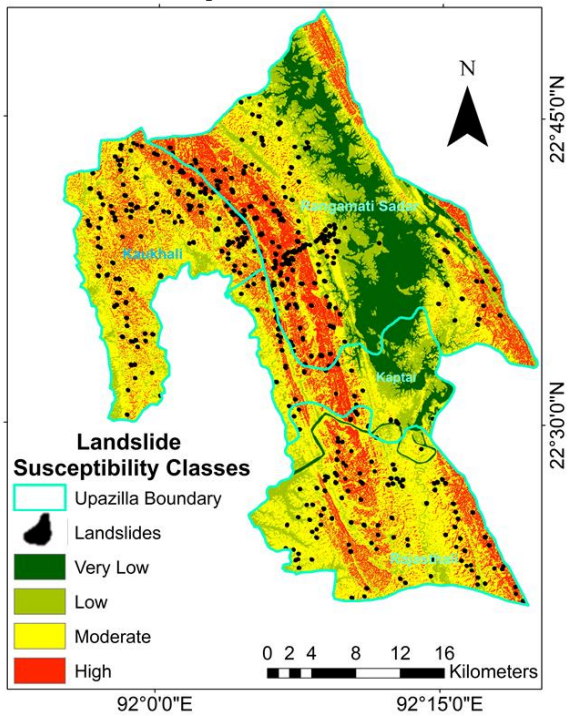

Fig. 4. Susceptibility Map of Rangamati District produced from Weights of Evidence model.

4. VALIDATION

In order to determine the degree of accuracy, the model needs to be validated to see how well the susceptible classes are defined by the weights of evidence model (WoE). A statistical method thereby was used to validate the results obtained. 75% of the polygons were used in the analysis to training the dataset to produce the susceptibility map. Later, the area of each susceptible hazard

class was divided further into 32 classes and the percentage of hazard-prone areas was computed from the overall hazard map. The percentage of landslide susceptibility index rank was then plotted against the percentage of cumulative landslide occurrence to produce the success rate curve. The validation was carried out from the gradient of the success rate curve. About 20% of the highly susceptible areas include 84% of the total landslide area and 30% of the highly susceptible area covers more than 99% of- the total landslide areas (Fig. 6).

The landslide susceptibility map that was produced from 2017 landslide events was classified into high to very low susceptible classes, summarized in table 2. About 21.7%, 47%, 18.9% and 12.4% of the study area fall in high, moderate, low and very low landslide hazard-prone classes respectively (Fig. 5).

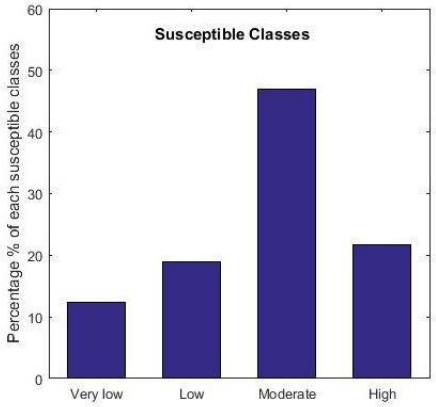

Fig. 5. Bar chart showing susceptible classes.

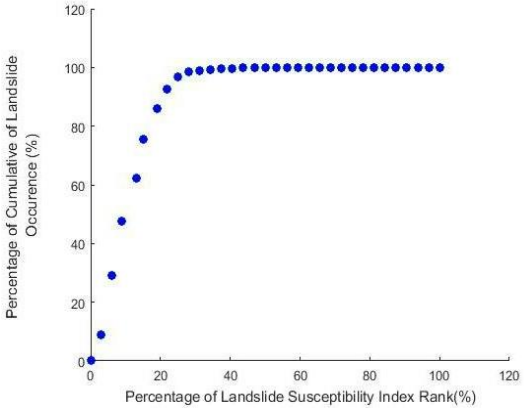

Fig. 6. The graph shows the success rate of the model used.

The table below shows how much of each upazilla of the study area is susceptible to landslide hazard. From Table 2 and Fig. 7, it can be perceived that Rangamati Sadar has highest and Kaptai upazilla has the lowest landslide susceptibility compared to other upazillas.

Table 2: Upazilla-wise area and percentage of landslide susceptible classes

	Very Low		**Low**		**Moderate**		**High**	
	Area (Sq.meter)	**Percentage %**	**Area (Sq.meter)**	**Percentage %**	**Area (Sq.meter)**	**Percentage %**	**Area (Sq.meter)**	**percentage %**
Rangamati Sadar	108033125	22.96	108244218.8	23.009	149407656.3	31.75	104745312.5	22.26
Rajasthali	3784218.75	1.40	38423593.75	14.23	168187812.5	62.30	59532968.75	22.05
Kawkhali	0	0	26488750	11.65	146109062.5	64.30	54625625	24.04
Kaptai	23962187.5	18.78	34094375	26.72	51025625	39.99	18504843.75	14.50

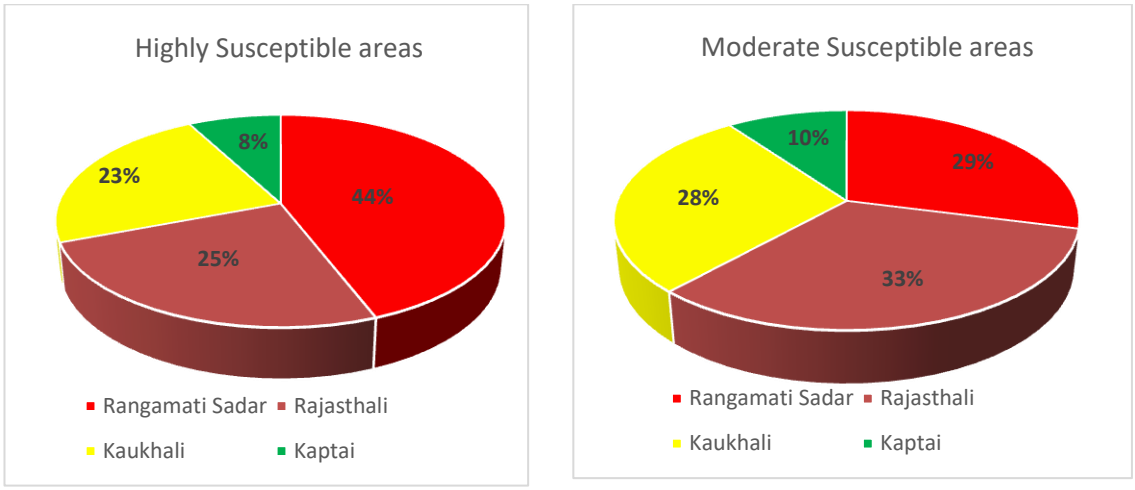

Fig. 7. Pie chart shows the high and moderate susceptible areas.

5. CONCLUSIONS

The number of 2017 landslide in Rangamati was staggering which has motivated to conduct this study to identify the future susceptible areas. The study used a bivariate Weights of Evidence model where landslide inventory and conditional factors such as rainfall, slope angle, slope aspect, vegetation, land use, geology, elevation, distance from the drainage and roads, were used. The majority of the factor maps were produced from digital elevation model and optical satellite image analysis and the landslide inventory was produced from SAR image analysis, namely, offset tracking and from the sub-pixel correlation of optical imagery. These techniques are based on Fourier shift theorem. The sub-pixel correlation works on both spatial and frequency domain. The normalized cross-correlation (NCC) is used in both techniques to find out the quality of the correlation result. The combined method enabled to identify the previous landslides required for the susceptibility mapping. Finally, the landslide susceptibility information has been retrieved from the conditional probability of previous landslide occurrence on the areas of triggering factors. The Weight values which define the spatial relationships of the factors in occurrence of landslides shows that higher slope (>45 degrees), elevation greater than 89 meters, hills predominantly facing in West direction, geological formation having alteration of sandstone and shale (Bhuban and Bokabil), presence of vegetated and bare area has higher contribution to landslide occurrence than other classes of the respective triggering factor. Rainfall has been observed to be the main causal factor as it received the highest weight value among the other conditioning factors. Drainage and road have little relation to the occurrence of landslide since the events were widely distributed over the area. The landslide susceptible areas are then divided into several classes from very low to high hazard prone. From the analysis, it has been observed that Rangamati Sadar has the highest and Kaptai upazilla has the lowest susceptibility towards landslide hazard occurrence. The method was validated from the success rate curve. It plots the percentage of landslide susceptibility index rank against the percentage of cumulative landslide occurrence. The produced susceptibility map can later be utilized by the policymakers to manage the severity of devastating landslide occurrence in future by taking appropriate advance mitigation strategy.

REFERENCES

[1] B. Pradhan and S. Lee, "Environmental Modelling & Software Landslide susceptibility assessment and factor effect analysis : backpropagation artificial neural networks and their comparison with frequency ratio and bivariate logistic regression modelling," *Environ. Model. Softw.*, **25**(6), pp. 747–759, 2010.

[2] R. & W. C. Soeters, "Slope instability Recognition, analysis and zonation (PDF Download Available)," Washington, D.C, 1996.

[3] D. M. Cruden and D. J. Varnes, "Landslide types and processes," *In: Turner AK, Schuster, RL (eds) Landslides investigation and mitigation, special report*, **247**, no. 1982. pp. 36–75, 1996.

[4] B. Ahmed, "Community Vulnerability to Landslides in," University College London (UCL), 2017.

[5] UN RC, "Bangladesh: HCTT Response Plan (June-December 2017) - Bangladesh | ReliefWeb," *reliefweb*, 2017. [Online]. Available: https://reliefweb.int/report/bangladesh/bangladesh-hctt-response-plan-june-december-2017. [Accessed: 01-Nov-2017].

[6] S. Park, C. Choi, B. Kim, and J. Kim, "Landslide susceptibility mapping using frequency ratio, analytic hierarchy process, logistic regression, and artificial neural network methods at the Inje area, Korea," *Environ. Earth Sci.*, **68**(5), pp. 1443–1464, Mar. 2013.

[7] A. Carrara, M. Cardinali, R. Detti, F. Guzzetti, V. Pasqui, and P. Reichenbach, "GIS techniques and statistical models in evaluating landslide hazard," *Earth Surf. Process. Landforms*, 16(5), pp. 427–445, Aug. 1991.

[8] L. N. Thanh and F. de Smedt, "Application of an analytical hierarchical process approach for landslide susceptibility mapping in A Luoi district, Thua Thien Hue Province, Vietnam," *Environ. Earth Sci.*, **66**(7), pp. 1739–1752, 2012.

[9] C.J. Van Westen, "The Modelling Of Landslide Hazards Using Gis (PDF Download Available)," *Surv. Geophys.*, (21), pp. 241–255, 2000.

[10] I. V. I. F. Dănuț Petrea, Ștefan Bilașco, Sanda Roșca, "The determination of the Landslide occurence probability by spatial analysis of the Land Morphometric ...," *Carpathian J. Earth Environ. Sci.*, **9**, pp. 91–102, 2014.

[11] A. S. Dhakal, T. Amada, and M. Aniya, "Landslide Hazard Mapping and the Application of GIS in the Kulekhani Watershed, Nepal," *Mt. Res. Dev.*, **19**(1), p. 3, Feb. 1999.

[12] B. Ahmed, "Landslide susceptibility modelling applying user-defined weighting and data-driven statistical techniques in Cox???s Bazar Municipality, Bangladesh," *Nat. Hazards*, **79**(3), pp. 1707–1737, 2015.

[13] H. Shahabi, B. B. Ahmad, and S. Khezri, "Evaluation and comparison of bivariate and multivariate statistical methods for landslide susceptibility mapping (case study: Zab basin)," *Arab. J. Geosci.*, **6**(10), pp. 3885–3907, 2013.

[14] B. Ahmed and A. Dewan, "Application of Bivariate and Multivariate Statistical Techniques in Landslide Susceptibility Modeling in Chittagong City Corporation , Bangladesh," *Remote Sens.*, no. May 2014, 2017.

[15] M. Adhikari, "Bivariate Statistical Analysis of Landslide Susceptibility in Western Nepal," University of Oslo, 2011.

[16] B. Neuhäuser, "Landslide Susceptibility and Climate Change Scenarios in Flysch Areas of the Eastern Alps," 2014.

[17] D. P. Kanungo, M. K. Arora, S. Sarkar, and R. P. Gupta, "Landslide Susceptibility Zonation (LSZ) Mapping - A Review," *J. South Asia Disaster Stud.*, **2**(1), pp. 81–106, 2009.

[18] G. F. Bonham-Carter, *Geographic Information Systems for Geoscientists, Modeling with GIS*. Oxford: Pergamon Press, 1994.

[19] D. F. Bonham-Carter, G.F., Agterberg, F.P. & Wright, "Weights of evidence modelling: A new approach to mapping mineral potential.," *Stat. Appl. Earth Sci.*, **89**(9), pp. 171–183, 1989.

[20] G. F. Bonham-Carter, "Geographic information systems for geoscientist: Modelling with GIS.," pp. 302–334, 2002.

[21] H. Foroosh, J. B. Zerubia, and M. Berthod, "Extension of phase correlation to subpixel registration," *IEEE Trans. Image Process.*, **11**(3), pp. 188–199, 2002.

[22] R. E. Crippen and R. G. Blom, "Measurement of Subresolution Terrain Displacements Using Spot Panchromatic Imagery," in *[Proceedings] IGARSS'91 Remote Sensing: Global Monitoring for Earth Management*, 1991, **3**, pp. 1667–1670.

[23] N. Van Puymbroeck, R. Michel, R. Binet, J. P. Avouac, and J. Taboury, "Measuring earthquakes from optical satellite images.," *Appl. Opt.*, **39**(20), pp. 3486–94, 2000.

[24] M. Yaseen and S. Anwar, "Sensitivity analysis of sub-pixel correlation technique for measuring coseismic displacements using a pair of ASTER images," *J. Asian Earth Sci.*, **62**, pp. 349–362, 2013.

[25] S. Leprince, S. Barbot, F. Ayoub, and J. P. Avouac, "Automatic and precise orthorectification, coregistration, and subpixel correlation of satellite images, application to ground deformation measurements," *IEEE Trans. Geosci. Remote Sens.*, **45**(6), pp. 1529–1558, 2007.

[26] Y. Fialko, D. Sandwell, M. Simons, and P. Rosen, "Three-dimensional deformation caused by the Bam, Iran, earthquake and the origin of shallow slip deficit," *Nature*, **435**(7040), pp. 295–299, 2005.

[27] J. Lu, "Sentinel-1 Toolbox Offset Tracking Tutorial," August, 2016.

[28] E. Pathier, E. J. Fielding, T. J. Wright, R. Walker, B. E. Parsons, and S. Hensley, "Displacement field and slip distribution of the 2005 Kashmir earthquake from SAR imagery," *Geophys. Res. Lett.*, **33**(20), pp. 1–5, 2006.

[29] L. Sun and J. P. Muller, "Evaluation of the use of sub-pixel offset tracking techniques to monitor landslides in densely vegetated steeply sloped areas," *Remote Sens.*, **8**(8), 2016.

[30] F. Casu, A. Manconi, A. Pepe, and R. Lanari, "Deformation time-series generation in areas characterized by large displacement dynamics: The SAR amplitude pixel-offset SBAS technique," *IEEE Trans. Geosci. Remote Sens.*, **49**(7), pp. 2752–2763, 2011.

[31] A. S. Goudie, "Encyclopedia of Geomorphology," *Encyclopedia of Geomorphology*, **1**. Routledge, p. 1156, 2004.

[32] USGS, "Remote Sensing Phenology," *USGS*. [Online]. Available: https://phenology.cr.usgs.gov/ndvi_foundation.php. [Accessed: 16-Dec-2017].

[33] J. Barsi, K. Lee, G. Kvaran, B. Markham, and J. Pedelty, "The Spectral Response of the Landsat-8 Operational Land Imager," *Remote Sens.*, **6**(10), pp. 10232–10251, Oct. 2014.

[34] E. Özşahin, "Using Geographic Information System And Analytical Hierarchy Process In Landslide Susceptibility Analysis In Tekirdağ Province," *Cent. East. Eur. Online Libr.*, pp. 137–144, 2014.

[35] Geological Survey of Bangladesh, "Description of Map Units," p. 2001, 2001.

*Bangladesh Journal of Physics, **23 & 24**, 65-81, 2018*

EFFICIENCY ENHANCEMENT OF WIDE BANDGAP SOLAR CELL BY PROPERLY TUNED INDIUM GALLIUM NITRIDE QUANTUM DOTS

SADIA SULTANA[1] AND JAMAL UDDIN AHAMED[2*]

[1]*Department of Information and Communication Technology, Comilla University, Comilla*

[2]*Department of Electrical & Electronic Engineering, University of Chittagong, Chittagong 4331, Bangladesh*

** Corresponding author: E-mail: ahamed.jamal@cu.ac.bd*

Received on 01.07.2018, Revised received on 02.09.2018, Accepted for Publication on 05.09.2018

ABSTRACT

The recent surge in the utilization of semiconductor nanostructures for solar energy conversion has led to the development of high-efficiency solar cells. Some of these recent advances are in the areas of synthesis of new semiconductor materials and the ability to tune the electronic properties through size, shape, and composition and to assemble quantum dots as hybrid assemblies. The emergence of quantum dot-sensitized solar cells has provided an alternative way to harvest sunlight for energy conversion. In this paper, InGaN-based quantum dot intermediate band solar cell model has been proposed. Insertion of quantum dots leads to the formation of an intermediate band between the conduction and valence band which contribute relatively higher short circuit current and open circuit voltage because of wide bandgap GaN host material. Performance of the solar cell has been investigated under a wide variety of intensities, wavelengths and series resistances. Our mathematical simulation showed that the cell has a short circuit current of 44.6 mA, open circuit voltage of 1.3304 V and 84.06% Fill Factor under 116 mW/cm^2 light intensity. Consequently, relatively higher power conversion efficiency of about 43% has been achieved which is much higher than the literature value reported elsewhere. MATLAB version 7.10.0499 (R2010) software has been used for the necessary calculation and simulation involved in this procedure.

Keywords: Efficiency, Enhancement, Quantum dots, Bandgap, Solar cells, Intermediate band.

1. INTRODUCTION

Researchers all over the world are making numerous efforts to produce wide spectrum solar cells which can use of most of the solar spectra. The most promising candidate to realize this goal is Quantum Dot Intermediate Band Solar Cell. The intermediate band solar cell concept was proposed to overcome the limitations of conventional silicon based single junction solar cells whose conversion efficiency is limited by various factors like charge carrier recombination, non-radiative intrinsic losses, material bandgap etc [1]. They have a limited operation range because they convert light energy from a small part of AM 1.5 solar spectra [2] and most of sun's energy goes unused. The aim of third generation photovoltaics is cost effective, environment friendly power generation. In 1997, Luque and Marti proposed that efficiency of ideal solar cells can be increased by photon induced transitions at intermediate levels [3]. Intermediate bands can be formed by using Quantum Dots (QD). Quantum dots (QD) are nano sized semiconductor particles, typically in the range of 2 to 10 nms. Carrier movements in these nanoparticles are confined in all three spatial dimensions by potential energy barriers. So their electrical and optical properties can be tuned as desire by varying their size [4]. In a p-i-n structured solar cell, quantum dots are embedded into the intrinsic region with spacing close enough to form a miniband. It is also found from the literature reports that if quantum dots (QDs) are stacked densely; they will electrically couple along the stacking direction and form minibands [5]. Since, carriers that are excited into the superlattice minibands spatially separate in an internal electric field of a solar cell, the electron–

hole recombination rate for the photoexcited carriers decreases, and consequently, the electron lifetime in the miniband increases [5]. It creates a narrow band of states in the middle of the bandgap of a photovoltaic material. Unlike conventional solar cells, where the incident photon energy must be greater than the bandgap energy of the material to conduct current; in a quantum dot solar cell, a relatively low energy photon can excite an electron from valence band to intermediate band. Later, it can be moved from intermediate band to conduction band by another low energy photon. Thus, the addition of embedded quantum dots in the solar cell material makes it possible to utilize photons with lower energy than the material's bandgap. Number of intermediate bands can be one or more. If there is only one intermediate band, the solar cell is called single intermediate band solar cell. If the number of intermediate band is more than one, the solar cell is called a multiple intermediate band (MIB) solar cell [6]. To design a multiple intermediate band solar cell, one must use different sized quantum dots in the intrinsic. If quantum dots of only one size and one particular bandgap are used, the solar cell will have single intermediate band. Single intermediate band solar cells can reach a maximum power conversion efficiency of 63.1% with concentrated sunlight [3]. This significantly overcomes the Shockley Quiesser limit [3]. Quantum dot solar cells have been claimed as 'The next big thing in Photovoltaics' by researchers [7]. Several combinations of dot material and solar cell material have been tried out by researchers. Cadmium Selenide (CdSe), Lead Sulphide (PbS), Lead Selenide (PbSe), Indium Arsenide (InAs) and Indium Gallium Nitride (InGaN) have been viewed by researchers as appropriate dot materials [7-12]. The photovoltaic materials in which QDs are embedded are called host materials. Several combination of dot-host materials have been tried out by scientists. CdSe QD with Titanium Dioxide (TiO_2), InAs QD on Gallium Arsenide (GaAs) has shown good performance [13-18]. Insertion of QDs increase light absorption and hence the short circuit current of the solar cell but reduces the open circuit voltage. Quantum dot solar cells made of narrow bandgap semiconductors, have open circuit voltage typically below 1 V. This problem can be overcome if a wide bandgap photovoltaic material is used as the host material. InGaN dot on GaN has been proposed by researchers for improved performance because of larger bandgap energy to compensate phonon relaxation loss, greater effective mass for easy confinement, increased number of possible intermediate bands, high transition rate of electrons etc. [19-22]. Previously, Gallium Nitride (GaN) based Indium Gallium Nitride (InGaN) quantum well solar cells have been reported to have notable performance [23-24]. By using Quantum Dots, the performance of GaN based solar cells can be further enhanced. Both wurtzite and zinc blende Indium Gallium Nitride quantum dots provide a wide range of tunable bandgap and wavelength [23-25].

The effect of incorporating InGaN QDs in the absorber region increases photon absorption. Because of using low bandgap QDs, they can absorb even photons which have lower energy than GaN's bandgap energy. The tunable bandgap, expected high radiation resistance, and strong absorption coefficient of the $In_xGa_{1-x}N$ material system are promising for high-efficiency photovoltaic systems [26]. $In_xGa_{1-x}N$/GaN based materials have played an influential role and become promising challenger in the ultramodern fabrication technology because of some of their notable features [27]. In this paper, we have used the minimum obtainable bandgap of the wurtzite $In_{0.99}Ga_{1-0.99}N$ quantum dots [28] to increase the photon absorption of a single intermediate band solar cell. These solar cells are 10 nm in radius and have a bandgap of 0.79 eV [28]. In order to calculate the photocurrent, one needs to consider the absorption cutoff wavelength of the base material. The total absorption range is extended over the absorption wavelength interval of the QD and base material regions [29]. The absorption cutoff wavelength of GaN is 365 nm. So, with GaN

as the base material, the resulting absorption range is 365 nm to 1565 nm [28]. So we have studied the device performance under different intensities & wavelengths and derived the different performance parameters; such as open circuit voltage, short circuit current, fill factor and power conversion efficiency. The effect of series resistance was also studied at different wavelengths. MATLAB version 7.10.0499 (R2010) software has been used for necessary calculation and simulation involved in this procedure.

2. THEORETICAL FRAMEWORK

2.1 Choosing an appropriate model

Several analytical models have been proposed by researchers to determine the performance of quantum dot solar cells. We have used the model proposed by Aroutionian, Petrosyan and Khachatryan [30]. The cell has a $p^+ - i - n^+$ structure. Dimensions of the cell are similar to those used in ref. [24]. InGaN quantum dots have a radius of 10 nm and are embedded into the intrinsic region between p and n type GaN region as shown in Fig. 1.

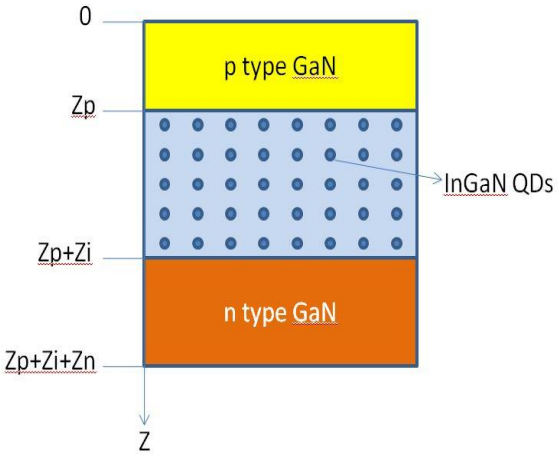

Fig. 1. Structure of quantum dot solar cell.

2.2 Governing equations

2.2.1 Photocurrent calculation

If the wavelength of the incident light is λ, and flux F(λ), the electron-hole generation rate at a depth 'z' is given as-

$$G_p(\lambda, z) = \alpha(\lambda)[1 - R(\lambda)]F(\lambda)\exp[-\alpha(\lambda)z] \tag{1}$$

Here, $R(\lambda)$ is the surface reflection coefficient and $\alpha(\lambda)$ is the light absorption coefficient of GaN. These coefficients were obtained from ref. [31-33]. The solar spectrum model described by black body curve has been used here with AM1.5, 1 sun condition. So, the spectral distribution of solar flux incident on the cell surface is provided by the following equation:

$$F(\lambda) = 3.5\times10^{21}\lambda^{-4}\left[\exp\left(\frac{hc}{kT_1\lambda}\right)-1\right]^{-1}\ \frac{photon}{cm^2.s.\mu m} \tag{2}$$

Where, 'h' and 'k' are Planck's constant and Boltzmann constant respectively, 'c' is the velocity of light and T_1=5760K. Photo generated electron current density at z=$z_p$is given as

$$j_n(\lambda) = \alpha(\lambda)eF(\lambda)[1-R(\lambda)]\frac{\alpha_n(\lambda)}{\alpha_n(\lambda)^2-1}\beta_n[b_n+\alpha_n(\lambda)-\exp\left(-\frac{z_p\alpha_n(\lambda)}{L_n}\right)[[b_n$$
$$+\alpha_n(\lambda)]\cosh\left(\frac{z_p}{L_n}\right)+[1+b_n\alpha_n(\lambda)]\sinh\left(\frac{z_p}{L_n}\right)]] \tag{3}$$

Here, *e* denotes the absolute value of electronic charge and

$$\beta_n = [\cosh\left(\frac{z_p}{L_n}\right)+b_n\sinh\left(\frac{z_p}{L_n}\right)]^{-1}$$

$b_n = \frac{S_nL_n}{D_n}$ and $\alpha_n(\lambda)=\alpha(\lambda)L_n$.

The total photocurrent collected by *p* type can be calculated as-

$$J_n^p = \int_0^{\lambda_1} j_n(\lambda)d\lambda \tag{4}$$

Here, λ_1 is the absorption cutoff wavelength of GaN (≈ 365 nm). Photocurrent collected by *n* type region can be estimated in a similar manner taking into account the attenuation of light through the *p* type and intrinsic region. For the QDs inside the intrinsic region, rate of photocarrier generation is-

$$G_D(\lambda,z)=\alpha_D(\lambda)[1-R(\lambda)]F(\lambda)\exp[-\alpha_D(\lambda)\times(z-z_p)] \tag{5}$$

Where, $\alpha_D(\lambda)$ is the absorption coefficient of the QD ensemble and was estimated using the data from ref. [34] for InGaN alloys.

The photocurrent collected from the QDs is given as-

$$j_D(\lambda)=e\int_{z_p}^{z_p+z_i}G_D(\lambda,z)dz \tag{6}$$

Photocurrent collected from the GaN barrier regions within the intrinsic region is-

$$j_B(\lambda)=e\int_{z_p}^{z_p+z_i}G_B(\lambda,z)dz \tag{7}$$

Where, the photocurrent generation rate in the barrier region is given as-

$$G_B(\lambda,z)=[1-R(\lambda)]F(\lambda)\exp[-\alpha(\lambda)z_p]$$
$$\times(1-n_DV_D)\alpha(\lambda)\times\exp[-(1-n_DV_D)\alpha(\lambda)(z-z_p)] \tag{8}$$

Here, V_D is the volume of a single quantum dot and n_D is the volume density of QDs.
Total photocurrent collected from the intrinsic region is-

$$J_i = e\left[\int_0^{\lambda_1} j_B(\lambda)d\lambda + \int_{\lambda_1}^{\lambda_2} j_D(\lambda)d\lambda\right] \tag{9}$$

Where, λ_2 is the absorption cutoff wavelength of the quantum dots (≈ 1569 nm).

Taking into account the recombination losses for the intrinsic region, the short circuit current density of the cell is given as-

$$J_{SC} = f_i(J_n^p + J_p^n + J_i) \tag{10}$$

Here, f_i is the transport factor, in other words, the mean probability that a charge carrier will cross the intrinsic region without being captured or recombined.
The total current density of the cell is-

$$J = J_{SC} - J_0\left[\exp\left(\frac{eV}{kT}\right) - 1\right] \tag{11}$$

Here, the reverse saturation current of the junction, J_0 has two components. One is due to minority carriers generated at the edges of the depletion layer and given as-

$$j_{s1} = A\exp(-\frac{E_{gB}}{\nu kT}) \tag{12}$$

Where, $A = eN_cN_v\left(\frac{D_p}{N_DL_p} + \frac{D_n}{N_AL_n}\right)$

N_c and N_v are the effective density of states in GaN, D_n and D_p are the electron and hole diffusion constants respectively, N_D is the donor concentration in the n type region and N_A is the acceptor concentration in the p type region. E_{gB} is the bandgap value of bulk GaN and ν is the ideality factor.
Another component of reverse saturation current is constituted by minority carriers generated in the interior of the intrinsic region by thermal excitation. It is given as-

$$j_{s2} = A^{eff}\ \exp(-\frac{E_{eff}}{\nu kT}) \tag{13}$$

Here, $E_{eff} = [1 - n_DV_D]E_{gB} + n_DV_DE_{gD}$.

E_{gD} is the bandgap of the quantum dots used in this research, which is 0.79 eV. It was calculated for $In_{0.99}Ga_{1-0.99}N$ alloy using the Brus equation [28, 34].

$$A^{eff} = e4\pi n^2kT / c^2h^3E_{eff}^2 \tag{14}$$

Where, n is the average refractive index of the intrinsic region.

2.2.2 Calculation of open circuit voltage

Open circuit voltage of the cell was calculated using the following equation:

$$V_{OC} = \left(\frac{kT}{q}\right) \times 2.303 \log\left(\frac{J_{SC}}{J_0} + 1\right) \tag{15}$$

2.2.3 Efficiency and Fill Factor calculation

Efficiency of the solar cell at the maximum power point can be can be calculated as-

$$\eta = \frac{V_{opt} J_{opt}}{P_0} = \frac{kT}{e} t_{opt} [J_{SC} - J_0 (e^{t_{opt}} - 1)] / P_0 \tag{16}$$

Where, $P_0 = 116 mw / cm^2$ is the incident solar flux for 1 sun, AM 1.5 condition. t_{opt} is defined by the following equation:

$$e^{t_{opt}} (1 + t_{opt}) - 1 = \frac{J_{SC}}{J_0} \tag{17}$$

Fill factor of the cell is determined using the relation given bellow:

$$FF = \frac{P_{\max}}{I_{SC} V_{OC}} \tag{18}$$

Where, $P_{\max}$ is the output power obtained at maximum power point.

Average annual solar radiation arriving at the top of the Earth's atmosphere is roughly136.1 mW/cm^2 [35]. The Sun's rays are attenuated as they pass through the atmosphere, leaving maximum normal surface irradiance at approximately 100 mW/cm^2 at sea level on a clear day. When 136.1 mW/cm^2 is arriving above the atmosphere (when the sun is at the zenith in a cloudless sky), direct sun is about 105 mW/cm^2, and global radiation on a horizontal surface at ground level is about 112 mW/cm^2. The latter figure includes radiation scattered or reemitted by atmosphere and surroundings. The actual figure varies with the Sun's angle and atmospheric circumstances. Therefore, it is unlikely that a solar cell will receive radiation greater than 116mW/cm^2; hence, we did not use solar intensity more than this value in our mathematical simulation.

3. PARAMETERS AND SIMULATION

Parameters for the calculations have been obtained from different sources that documented either theoretical or practical values. Interpolation formula has been implemented to obtain some of the parameter values. Necessary calculation and simulations have been performed with MATLAB version 7.10.0499 (R2010a) software.

Simulation was carried out for wavelengths of 370, 400, 459, 516, 620, 729 and 826 nm respectively with the intensities fixed at 116 mW/ cm^2 and *I-V* curve were obtained for intensities of 116, 100, 70, 50, 30 and 10 mW/ cm^2 respectively.

Table 1: List of Parameters

Parameter name	Value [24, 28, 33]	Units
Acceptor atom concentration, N_A	1.00×10^{24}	m^{-3}
Donor atom concentration, N_D	1.00×10^{24}	m^{-3}
Volume of QD (V_D)	4.25×10^{-18}	cm^3
Volume density of QDs	1.731017×10^{17}	cm^{-3}
Bandgap of GaN, E_{gB}	3.42	eV
Bandgap of QDs, E_{gD}	0.79	eV
Surface recombination velocity for electrons, S_n	1.00×10^3	cm/s
Surface recombination velocity for holes, S_p	1.00×10^3	cm/s
Diffusion length of electrons, L_n	125×10^{-6}	cm
Diffusion length of holes, L_p	79×10^{-6}	cm
Diffusion constant of electrons, D_n	25	cm^2/s
Diffusion constant of holes, D_p	9	cm^2/s
Transport factor, f_i	0.12	
Effective density of states in conduction band, N_c	2×10^{18}	cm^{-3}
Effective density of states in valence band, N_v	1×10^{19}	cm^{-3}
p-region length, Z_p	0.1	μm
i-region length, Z_i	0.25	μm
n-region length, Z_n	0.15	μm

4. RESULTS AND DISCUSSION

We have studied the performance of our proposed solar cell under different solar intensities and wavelengths. The effect of series resistance on the cell efficiency was also studied at different wavelengths. At first, we have deremine the I-V characteristics curves of the proposed model for different wavelengths at different intensities. Figure 2 shows the current versus voltage curve of the proposed cell for different intensities at 370 nm wavelength. It is found from this figure that the maximum short circuit current of 44.6 mA was obtained when the light intensity was 116 mW/ cm^2 and the open circuit voltage at this intensity was found to be 1.3304 V. It is also noticed from our mathematical simulation that both short circuit current and open circuit voltage were found to decrease at lower intensities. For the intensities of 100, 70, 50 and 30 mW/ cm^2; short circuit current was 38.45, 26.91, 22.7, and 11.53 mA, and open circuit voltage was 1.323, 1.304, 1.287, 1.261 V respectively. When the intensity was reduced to 10 mW/ cm^2, both the short circuit current and open circuit voltage were found to decrease to 3.85 mA and 1.2 V, respectively.

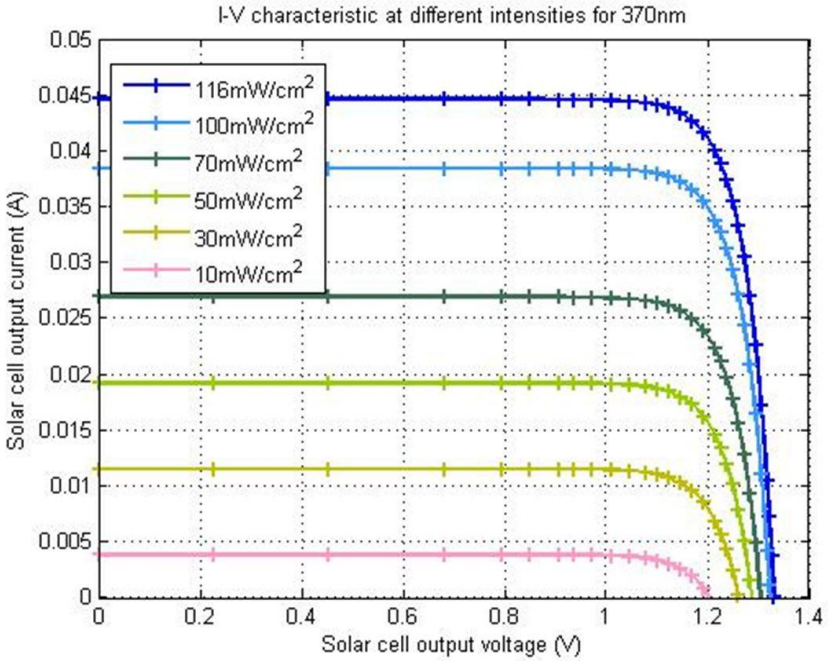

Fig. 2. I-V curves for different intensities at 370 nm wavelength.

Figure 3 shows that at 400 nm wavelength, with an intensity of 116 mW/cm^2, the cell showed maximum short circuit current of 36 mA and an open circuit voltage of 1.3249 V. At lower intensities, the value of short circuit current and open circuit voltage was reduced. Under 100, 70, 50, 30 and 10 mW/cm^2 intensity, short circuit was 31.03, 21.72, 15.52, 9.31, 3.1 mA and open circuit voltage was 1.317, 1.299, 1.281, 1.255 and 1.198 V, respectively.

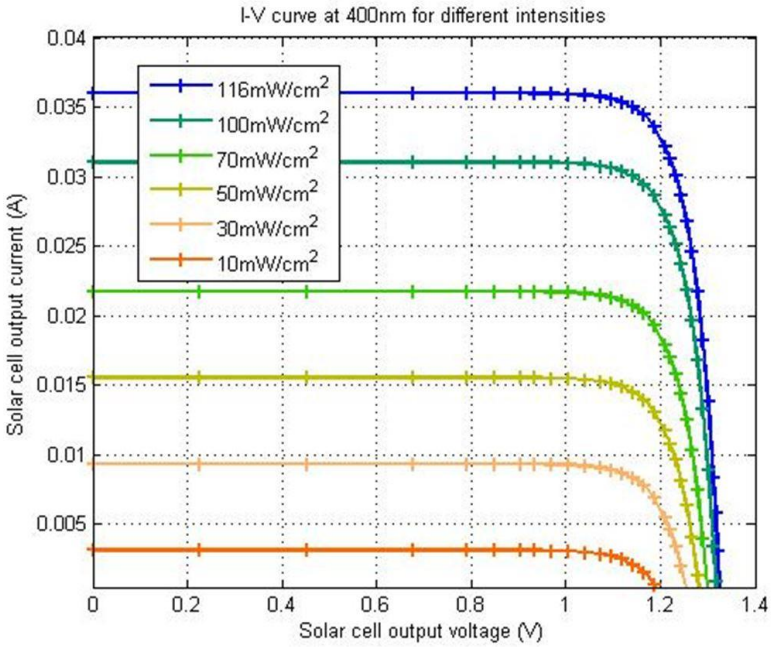

Fig. 3. I-V characteristics for different intensities at 400 nm wavelength.

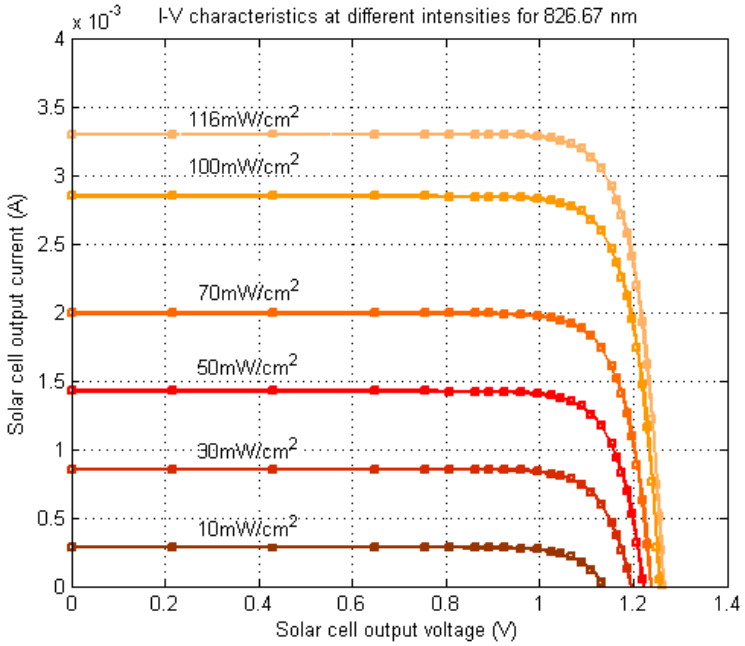

Fig. 4. I-V characteristics for different intensities at 826 nm wavelength.

It is found from the Fig. 4 that when the intensity of light was used as 116 mW/cm^2, the cell has a short circuit current of 3.3 mA and open circuit voltage of 1.2635 V at a particular wavelength of 826 nm. It is clear from this figure that both the short circuit current and open circuit voltages are decreasing with the decrease in light intensity. Hence, it can be concluded from Fig. 2, Fig. 3 and Fig.4 that the cell has a maximum short circuit current and open circuit voltage at a particular wavelength and intensities of 370 nm and 116 mW/cm^2, respectively.

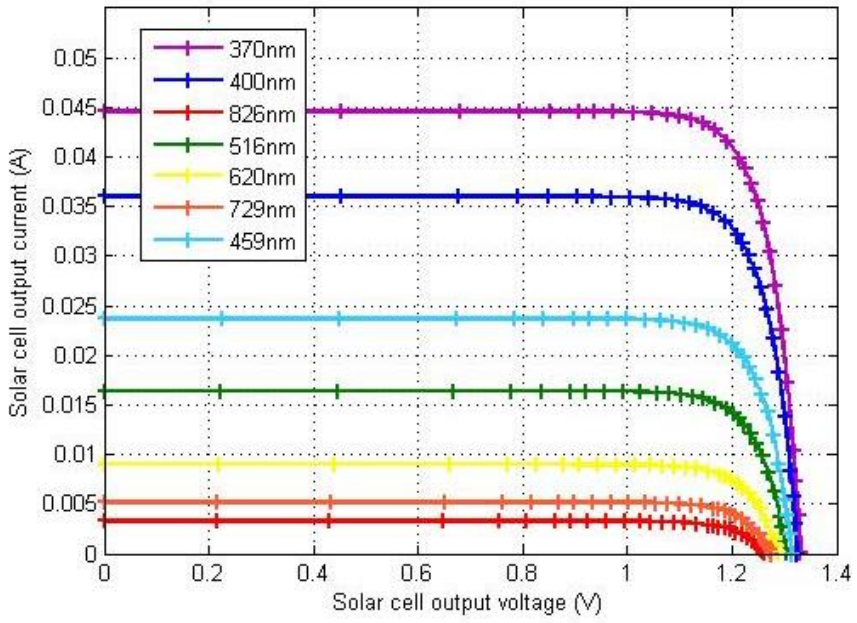

Fig. 5. I-V characteristics for different wavelengths at fixed intensity of 116 mW/ cm^2 .

Here, we have derived the I-V characteristics curve by varying the wavelengths and keeping the intensities fixed at 116 mW/ cm^2 . Figure 5, shows the I-V characteristics curve at different wavelength ranging from 370 to 826 nm at a fixed intensity of 116 mW/ cm^2 . Parameters derived from this characteristics curve are listed in Table 2.

Table 2: Performance Parameters at different wavelengths

λ **(nm)**	J_{SC} **(mA/cm^2)**	V_{OC} **(V)**	$P_{\max}$ **(W)**	η **%**	**FF (%)**
370	44.6	1.3304	0.04988	43	84.06
400	36	1.3249	0.04007	34.54	84.01
459	23.7	1.3142	0.02614	22.53	83.93
516	16.4	1.3047	0.01794	15.47	83.84
620	9	1.2893	0.00971	8.37	83.68
729	5.2	1.2752	0.00554	4.78	83.53
826	3.3	1.2635	0.00348	3	83.41

It is evident from Table-2 that the solar cell demonstrated the utmost efficiency of 43%, open circuit voltage of 1.3304 V, short circuit current of 44.6 mA, and fill factor of 84.06% at the particular wavelength of 370 nm. It is also noticed from this table that the efficiency, open circuit voltage, short circuit current, and fill factor of the cell is found to decrease with the increase of wavelength. It can be concluded here that with increase of wavelength, photon energy capture by the solar cell is decreased. Hence, open circuit voltage, short circuit current and therefore output power of the cell is reduced. When the wavelength is increased to 826 nm, the efficiency of the cell is reduced to 2.7% but the fill factor of the solar cell is not reduced remarkably over the entire range of wavelength.

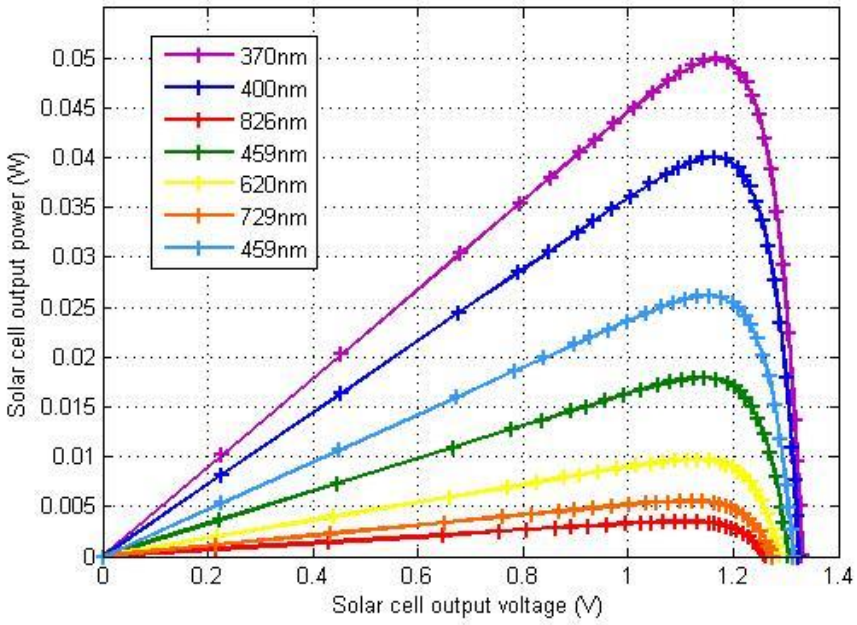

Fig. 6. P-V curve of the solar cell for different wavelengths of light.

Now, we derive the P-V characteristics curve of the solar cell for different wavelengths of light. Here, the P-V curve have been obtained for an intensity of 116 mW/ cm^2 . From the P-V curve shown in figure 6, it is evident that the solar cell delivers more power at shorter wavelengths. This is because at shorter wavelength the intensity of the incident photons is high; hence, more short circuit current is generated. Here, also noticed that peak power delivered by the cell is 0.04988 W/ m^2 for the wavelength of 370 nm.

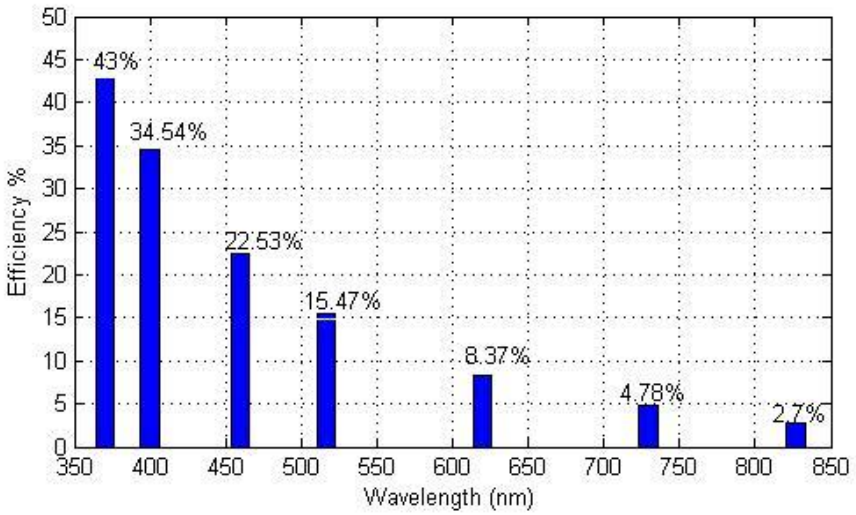

Fig. 7. Solar cell efficiency at different wavelengths.

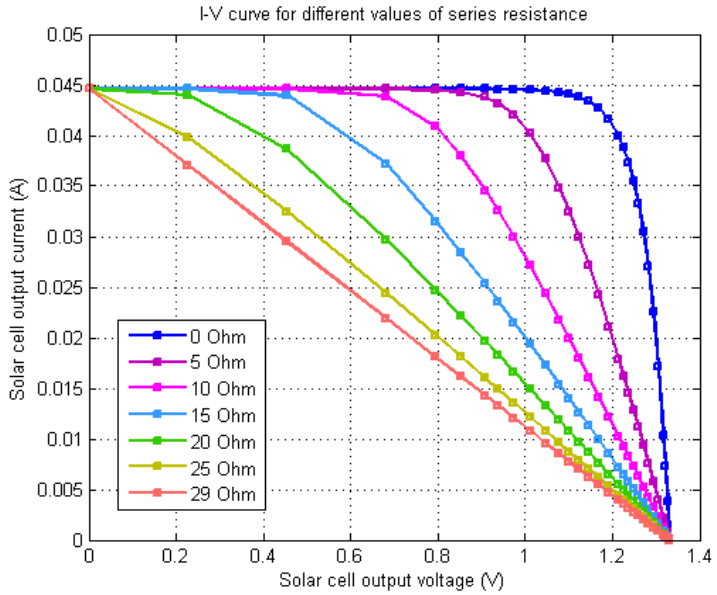

Fig. 8. Effect of series resistance for 370 nm wavelength.

Here, we estimate the solar cell efficiency at different wavelengths while keeping the solar intensity fixed at 116 mW/cm^2. It is evident from Fig. 7 that the maximum efficiency offered by this cell is 43% for a particular wavelength of light of 370 nm. It is known that at higher

wavelengths, photons have less energy, and the amount of photon absorption is reduced. Consequently, the efficiency of the solar cell is decreased with the increase in wavelength.
Finally, we have studied the effect of series resistance on the solar cell performance for different wavelengths. It is clear from the Fig. 8 that the efficiency of the solar cell drops to lower value from 35.27 to 27.98 to 21.81 to 17.42 to 14.31, and to 12.85%, respectively, when the series resistance increased from 5 to 10 to 15 to 20 to 25, and to 29 ohm, respectively, for the particular wavelength of 370 nm. The corresponding fill factors were 68.96%, 54.70%, 42.64%, 34.05%, 27.89% and 25.12%, respectively. It is evident from Fig.8 that the maximum value of series resistance without reducing the maximum short circuit current is 29 Ohm. If the series resistance is increased beyond this limit, it will cause a drop in the maximum value of short circuit current and it will be less than 44.6 mA.

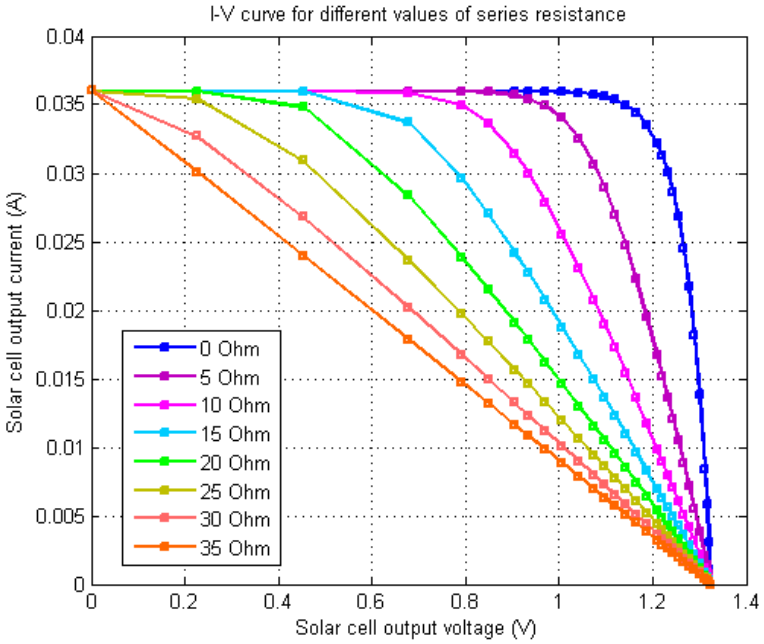

Fig. 9. Effect of series resistance at 400 nm wavelength.

Now, we examine the effect of series resistance for the particular wavelength of 400 nm. It is clear from the Fig. 9 that with increasing the series resistance from 5 to 10 to 15 to 20 to 25 to 30, and to 35 ohm, respectively the corresponding efficiency of the solar cell drops from 29.49 to 24.60 to 20.22 to 16.58 to 13.83 to 11.80, and to 10.43%, respectively for this wavelength. The corresponding fill factors were 71.33%, 59.83%, 49.17%, 40.32%, 33.65%, 28.71% and 25.36%, respectively. The maximum value of series resistance that doesn't cause a drop in maximum value of short circuit current is 35 ohm. If series resistance becomes more than 35 ohm, the cell will have lower maximum short circuit current than 36 mA.

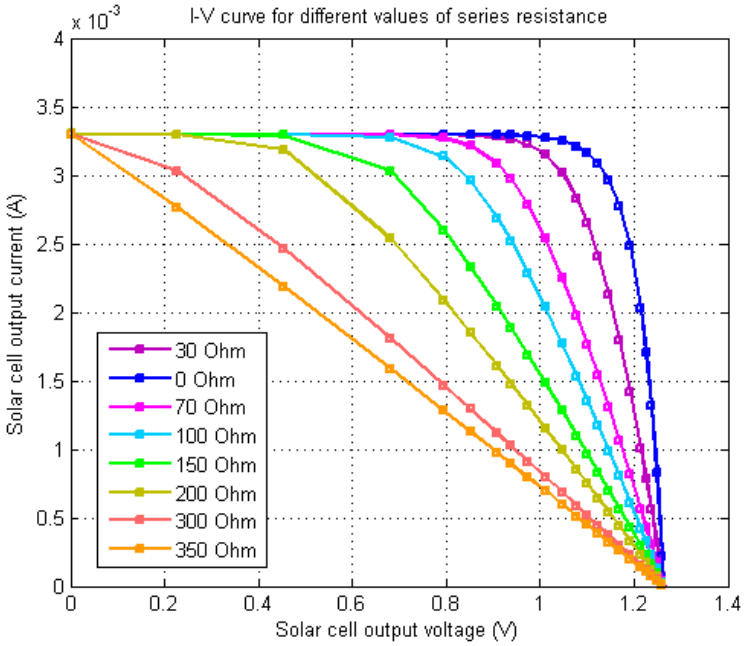

Fig. 10. Effect of series resistance at 826 nm wavelength.

Last of all, we examine the effect of series resistance on the solar cell performance for the particular wavelength of 826 nm. It is found from the Fig. 10 that with changing the series resistance from 30 to 70 to 100 to 150 to 200 to 300, and to 350 ohm, respectively, the corresponding efficiency drops from 2.74 to 2.41 to 2.16 to 1.8 to 1.48 to 1.06, and to 0.93%, respectively. The corresponding fill factors were 76.33%, 66.93%, 60.22%, 50.08%, 41.28%, 29.61% and 25.98%, respectively. The maximum value of series resistance that doesn't cause a drop in maximum value of short circuit current is 350 ohm in this case. If series resistance becomes more than 350 ohm, the cell will have lower maximum short circuit current than 3.3 mA. It is concluded here from the Fig. 8, Fig. 9 and Fig. 10 that the increase in series resistance affects the fill factor of the solar cell. It is also found that at shorter wavelengths, the fill factor is much affected by a certain value of series resistance.

Finally, we have compared the efficiency of our proposed solar cells with the previously reported results. Thosar et al. have demonstrated the GaN/InGaN solar cell and studied the efficiency of their proposed model [36]. Their proposed model showed the short circuit current and open circuit voltage of 3.40 mA /cm^2 and 1.98 Volt, respectively by using Ga-face p-GaN/n-InGaN heterostructure solar cell. Ramizy et al. [37] characterize the GaN/p-Si solar cell prepared by simple technique. They have found from their simple GaN based solar cell that open circuit voltage ranging from 0.45 to 0.7V, short circuit current from 16 to 16.6 mA, Fill Factor from 0.26 to 0.30 and efficiency from 4.8 to 8.8% depending on annealing temperature from 373K to 573K. Recently, researchers have enhanced the solar cell conversion efficiency of InGaN/GaN Multiple

Quantum Wells (MQW) by piezo-phototronic effect [38]. Their solar cell produced 1.17 mA/cm^2 short circuit current due to enhanced optical absorption and open circuit voltage was below 1.1 V. The conversion efficiency of the InGaN/GaN MQW solar cell was 1.24%, where FF was found to be 56.7%. Though the measurement technique is different, our simulated results showed that the cell has a short circuit current of 44.6 mA, open circuit voltage of 1.3304 V, Fill Factor of 84.06% and power conversion efficiency of about 43% which are much better than the literature value reported elsewhere.

5. CONCLUSIONS

Proper theoretical treatment is prerequisite to realize high efficiency single intermediate band Quantum Dot solar cells in practice. Here, we have studied the performance of a single intermediate band quantum dot solar cell based on theoretical model. We have studied the performance parameters of the solar cell under a wide variety of intensities, wavelengths and series resistance. In order to increase the photocurrent of a wide band gap solar cell, we have used very low bandgap (0.79eV) Quantum Dots in the intrinsic layer of the p-i-n structure. This leads to the formation of an intermediate band between conduction band and valence band. Due to the formation of intermediate band at this particular level, the device has achieved high short circuit current. At the same time, the proposed solar cell maintains a high open circuit voltage because of wide bandgap of the host material of GaN. In this design, we have used 10 nm sized $In_{0.99}Ga_{1-0.99}N$ quantum dots. With 44.6 mA short circuit current, 1.3304 V open circuit voltage and 84.06% Fill Factor, the cell showed 43% efficiency which has crossed the Shockley Queisser limit. This is the highest value of theoretical calculated efficiency for this type of solar cell than previously reported literature value. The proposed solar cell has shown promising results as a wide spectrum solar cell.

ACKNOWLEDGEMENT

This work was supported by the ICT Fellowship under the Information & Communication Technology Division, Government of The People's Republic of Bangladesh.

REFERENCES

[1] A. Richter, M. Hermle, S. W. Glunz, "Reassessment of the Limiting Efficiency for Crystalline Silicon Solar Cells," IEEE Journal of Photovoltaics, **3**, (2013) 1184-1191.

[2] American Society for Testing and Materials (ASTM) Terrestrial Reference Spectra for Photovoltaic Performance Evaluation, ASTM G-173-03.

[3] A. Luque and A. Martı, "Increasing the Efficiency of Ideal Solar Cells by Photon Induced Transitions at Intermediate Levels," Physical Review Letters, **28**, (1997) 5014-5017.

[4] C. P. Poole and F. J. Owens, Introduction to nanotechnology, Published by John Wiley & Sons, Inc., Hoboken, New Jersey (2003) 226-234.

[5] S. Watanabe et al., "Two-step photocurrent generation enhanced by miniband formation in InAs/GaAs quantum dot superlattice intermediate-band solar cells," Appl. Phys. Lett. **110**, (2017) 193104.

[6] L. Sang et al. "A Multilevel Intermediate-Band Solar Cell by InGaN/GaN Quantum Dots with a Strain-Modulated Structure," Advanced Materials, **26** (2014) 1414–1420.

[7] P. V. Kamat, "Quantum Dot Solar Cells. The Next Big Thing in Photovoltaics," The Journal of Physical Chemistry Letters, **4** (2013) 908−918.

[8] A. Kongkanand et al., "Quantum Dot Solar Cells. Tuning Photoresponse through Size and Shape Control of CdSe-TiO2 Architecture," Journal of American Chemical Society, **130** (2008) 4007-4015.

[9] L. Chang et al., "Low-Temperature Solution-Processed Solar Cells Based on PbS Colloidal Quantum Dot/CdS Heterojunctions," Nano Letters, **13** (2013) 994−999.

[10] K. Inuk and W. Frank, "Electronic structure and optical properties of PbS and PbSe quantum dots," Journal of the Optical Society of America B, **14** (1997) 1632-1646.

[10] Y. Pingrong et al., "Nanocrystalline TiO2 Solar Cells Sensitized with InAs Quantum Dots," J. Phys. Chem. B, **110 (**2006) 25451-25454.

[11] J. H. Bang and P. V. Kamat, "Quantum Dot Sensitized Solar Cells. A Tale of Two Semiconductor Nanocrystals: CdSe and CdTe," ACSNANO, **3** (2009) 1467–1476.

[12] S. Sultana et al., "Confinement effects and Tunability of Quantum Dots within Strong Confinement Regime," Proc. 2015 IEEE International WIE Conference on Electrical and Computer Engineering (WIECON-ECE), pp. 31-34.

[13] V. G. lez-Pedro et al., "Modeling High-Efficiency Quantum Dot Sensitized Solar Cells," ACS Nano, **4** (2010) 5783-5790.

[14] R. B. Laghumavarapu et al., "Improved device performance of InAs/GaAs quantum dot solar cells with GaP strain compensation layers," Applied Physics Letters, **91** (2007) 243115-1 – 243115-3.

[15] Denis Guimard et al., "Fabrication of InAs/GaAs quantum dot solar cells with enhanced photocurrent and without degradation of open circuit voltage," Applied Physics Letters, **96** (2010) 203507-1 – 203507-3.

[16] C. G. Bailey et al. "Near 1 V open circuit voltage InAs/GaAs quantum dot solar cells," Applied Physics letters, **98** (2011) 163105-1 – 163105-3.

[17] A. Rizk, K. Islam and A. Nayfeh , "Modeling of InAs/GaAs Quantum Dot Solar Cells," Proc. 2013 European Modelling Symposium, 2013, issn : 978-1-4799-2578-0/13 , pp. 677-680.

[18] B. Dong et al. "Modeling and Simulation of InAs/GaAs Quantum Dot Solar Cells In SILVACO TCAD," Proc. 40th IEEE Photovoltaic Specialists Conf., 2014, issn: 978-1-4799-4398-2/14 , pp. 476-478.

[19] W. C. Lai et al., "Efficiency Improvement of Short-Period InGaN/GaN Multiple-Quantum Well Solar Cells With H_2 in the GaN Cap Layer," Journal of Display Technology, **9** (2013) 953-956.

[20] N. Cavassilas et al., "Transport modeling of InGaN/GaN multiple quantum well solar cells," Proc. 40th IEEE Photovoltaic Specialists Conf., 2014, issn: 978-1-4799-4398-2/14, pp. 2875 – 2877.

[21] F. W. Huang et al., "Linear photon up-conversion of 450 meV in InGaN/GaN multiple quantum wells via Mn doped GaN intermediate band photodetection," Optics Express, A1211, **19** (2011) S6.

[22] N. G. Young et al., "High performance thin quantum barrier InGaN/GaN solar cells on sapphire and bulk (0001) GaN substrates," Applied Physics Letters, **103 (**2013) 173903-1- 173903-5.

[23] K. C. Wang, and Y. R. Wu, "Transition Rate in the InGaN Quantum Dot Intermediate-Band Solar Cell," Proc. 38th IEEE Photovoltaic Specialists Conf., 2012, pp. 822-825.

[24] M. L. Hossain et al., "Efficiency Enhancement of InGaN Based Quantum Well and Quantum Dot Solar Cell," Proc. 2nd International Conference on Informatics, Electronics & Vision, 2013, pp. 1-5.

[25] S. Sultana et al., “Tunable Bandgap and Wavelength Range of Zinc Blende Indium Gallium Nitride Quantum Dots,” proc. 18th International Conference on Computer and Information Technology (ICCIT), 21-23 December, 2015, pp. 550-553.

[26] A. G. Bhuiyan et. al., “InGaN Solar Cells: Present State of the Art and Important Challenges”, IEEE JOURNAL OF PHOTOVOLTAICS, **2 (**2012) 276-293.

[27] I. U. I. Chowdhury et al., “Performance analysis of high efficiency $In_xGa_{1-x}N$/GaN intermediate band quantum dot solar cells”, Results in Physics **9** (2018) 432-439.

[28] S. Sultana et al., “Optimization of Indium Gallium Nitride Quantum Dots for absorbing light from Solar Spectra,” Proc. International Conference on Electrical Information and Communication Technology, 2015, pp. 394-398.

[29] V. Aroutiounian et al., “Quantum dot solar cells,” in Journal Of Applied Physics, **89 (**2001) 2268-2271.

[30] J. F. Muth et al., “Absorption coefficient, energy gap, exciton binding energy, and recombination lifetime of GaN obtained from transmission measurements,” Applied Physics Letters, **71** (1997) 2572-1-2572-4.

[31] S. Adachi, “Optical Constants of Crystalline and Amorphous Semiconductors”, Kluwer Academic Publishers, Boston/Dordrecht/London, 101 Philip Drive, Assinippi Park, Norwell, Masachusetts 02061 USA., Springer Science & Business Media, 1999., pp. 182-185.

[32] W. R. L. Lambrecht, and B. Segall, “UV Reflectivity of GaN: Theory and Experiment,” Physical Review B, 1995, pp. 51 13516 – 51 13532.

[33] G. F. Brown et al., “Finite element simulations of compositionally graded InGaN solar cells,” Solar Energy Materials & Solar Cells **94** (2010) 478-483.

[34] L. E. Brus, “Electron-electron and electron-hole interactions in small semiconductor crystallites: The size dependence of the lowest excited electronic state,” J. Chem, Phys. **80** (1984) 4403-4409.

[35] O. Coddington et al., "A Solar Irradiance Climate Data Record", Bulletin of the American Meteorological Society. **97** (2016) 1265–1282.

[36] M. Thosar, M. Mathew, “Modeling for high efficiency GaN/InGaN solar cell,” IOSR Journal of Electrical and Electronics Engineering (IOSR-JEEE), **4** (2013) 1-4.

[37] A. Ramizy et al., “Characterization of GaN/p-Si solar cell prepared by simple technique,” Optik, **126** (2015) 3125–3128.

[38] C. Jiang et al., “Enhanced Solar Cell Conversion Efficiency of InGaN/GaN Multiple Quantum Wells by PiezoPhototronic Effect,” ACS Nano, **11** (2017) 9405–9412.

*Bangladesh Journal of Physics, **23 & 24**, 83-94, 2018*

FITTING PROCEDURE OF DPF DEVICES IN LEE MODEL CODE

M. R. HAQUE*, M. K. ISLAM, M. M. H. PRODHAN[1], M. A. MALEK AND M. S. S. CHOWDHURY

Plasma Physics Division, Atomic Energy Center, Dhaka, Bangladesh

[1]Department of Nuclear Engineering, University of Dhaka, Dhaka, Bangladesh

** Corresponding author:E-mail:reaz050.haque@gmail.com*

Received on 27.05.2018, Revised received on 01.08.2018, Accepted for Publication on 12.09.2018

ABSTRACT

Lee model code is a computation tool which can simulate and calculate all gross properties of a Dense Plasma Focus (DPF) device. The code can also be used to design efficient device and to predict the properties of the new device. In this paper detailed procedure is given to fit a DPF device into the Lee code. Types of parameters and their details are given. Manipulation of four model parameters (f_m, f_c, f_{mr} and f_{cr}) are discussed elaborately to fit a device by matching the computed total current profile with the experimental total current profile of the device. This paper is helpful for researchers those have started to use Lee model code for DPF study.

Keywords: Dense plasma Focus, Fusion neutron, Lee code

1. INTRODUCTION

The Dense Plasma Focus (DPF) took attention in the scientific community in the early 1960s as it produces intense burst of fusion neutrons operated in Deuterium/Deuterium-Tritium gas. It is a hydrodynamic coaxial plasma accelerator [1,2]. It was discovered by N. V. Filippov [1] and J. W. Mather [2]. It was then considered as an efficient pulsed fusion device. It is also a compact powerful source of multi-radiation [3].

When operated in deuterium, the fusion neutron burst contains typically 10^{15} neutrons per second over duration of tens of nanosecond [4]. The x-ray emission power peaks at 10^{9}W over a period of nanoseconds. Though the power of this device can be varied from mega-joule to sub-kilojoule, but every machine emits same energetic particles and radiations. Thus it becomes an experimental tool for fundamental and applied research related to fusion, neutron production, hard x-ray and high brightness soft x-ray production and astrophysical phenomena [5].The device is used for various medico-biological and industrial applications such as lithography (using 0.9–1.5 keV photons), radiography, microscopy (using 0.25–2.5 keV radiations), and micromachining (using 4 keV photons) [6].

To study and predict the properties of DPF device by numerical experiment, Lee model code is developed to simulate and predict all gross focus properties combining electrical circuit with plasma focus dynamics, thermodynamics and radiation. The basic model, described in 1984 [7], was successfully used to assist several projects [8–10]. Radiation coupled dynamics was included in the five-phase code, leading to numerical experiments on radiation cooling [4]. The vital role of

a finite small disturbance speed discussed by Potter in a Z-pinch situation was incorporated together with real gas thermodynamics and radiation-yield terms [11]. Then plasma self-absorption was included in 2007, improving the Soft X-Ray (SXR) yield simulation [12,13]. The code has been used extensively in several machines including UNU/ICTP PFF [14-17], NX2 [17-20], and NX1 [18,21] and has been adapted for the Filippov-type plasma focus DENA [22]. A recent development is the inclusion of the neutron yield Y_n(neutron yield) using a beam–target mechanism [23-27], incorporated in recent versions of the code (versions later than RADPFV5.13) [4], resulting in realistic Y_n scaling with I_{pinch} (Pinch current) [23,24]. Extensive numerical experiments have been carried out systematically resulting in the uncovering of neutron [23,24] and SXR [28-35] scaling laws over a wider range of energies and currents. The numerical experiments also gave insight into the nature and cause of neutron saturation [32,36,37]. It has also led to design and predict the properties of new devices.

At present research works are being conducted using Lee model code in the following related areas of DPF devices. Measurements of model parameters versus gas pressure [38], effects of pressure variation on neutron yields [39], electron beam properties on deuterium plasma focus [40], parametric optimization for neutron production [41], material testing for plasma facing wall in thermonuclear fusion reactor [42].

In this paper, we have demonstrated the procedure of conducting numerical experiment using Lee model code for any plasma focus device. The code that has been used for this investigation is RADPFV5.15de.xls [4]. This code is written using Microsoft Excel Visual Basic language. The user interface is an MS Excel window.

The procedure of numerical experiment depends on current profile matching of a device. The standard practice is to fit the computed total current waveform to an experimentally measured total current waveform using four model parameters representing the mass swept-up factor f_{m}, the plasma current factor f_{c} for the axial phase and mass factor f_{mr} and current factor f_{cr} for the radial phases. Because it has been found that the current profile/wave form of the plasma focus is one of the best indicators of gross performance of the device [4]. The axial and radial phase dynamics and the crucial energy transfer into the focus pinch are among the important information that is quickly apparent from the current trace [42]. These parameters determine the axial and radial dynamics, specifically the axial and radial speeds of the plasma sheaths which in turn affect the profile and magnitudes of the discharge current. The detailed profile of the discharge current during the pinch phase also reflects the Joule heating and radiative yields [42].

The paper is targeted to researchers or learners who are new in the arena of dense plasma focus research. Construction and working principle of the Dense Plasma Focus device with Lee model is discussed in this paper. Later on fitting procedure for any DPF device in the code is being discussed elaborately. Numerical experiment procedure has been presented with methodical approach.

This paper is divided into five sections. Section 1 is an introduction that contains brief overview including contributions and results of several groups around the world in the last few years. Then following topics are discussed elaborately in rest of the sections accordingly: Description of DPF device (Sec. 2), Lee model with system model equations (Sec. 3), fitting procedure of DPF devices in Lee model code (Sec. 4) and summary of the work (Sec. 5).

2. DESCRIPTION OF DPF DEVICE

DPF is constructed with two co-axial electrodes (anode and cathode) separated by an insulator in a vacuum chamber. The device uses the power stored in bank of capacitors. Generally, the device is filled with gases like Helium, Neon, Argon, Xenon, Nitrogen, Hydrogen, Deuterium etc. The filling pressure of the vacuum chamber is generally few mbar (Torr). When a shot is fired in this device, electric current starts to flow from anode to cathode which generates current sheath around the anode and hence a powerful azimuthal magnetic field is produced (Fig. 1).

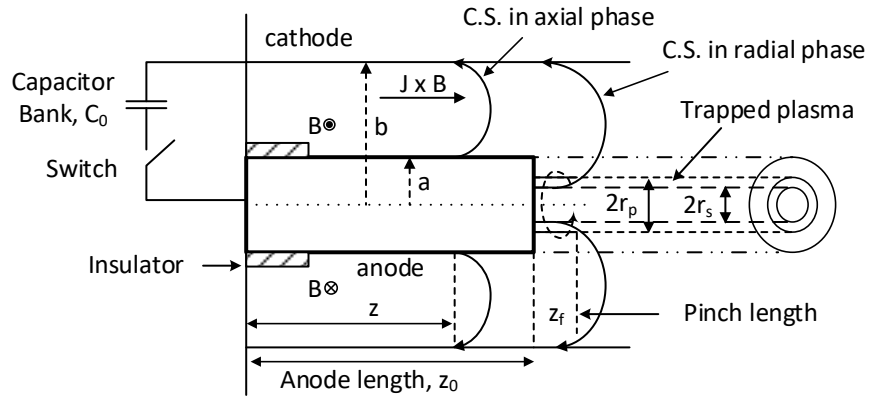

Fig. 1. Schematic of DPF device with axial and radial phase. [Here z is the position of current sheath (C.S.) at any time t, a & b are the radius of anode and cathode, r_p & r_s are the radius of magnetic piston and current sheath shock front in radial phase].

During operation, two phases develops in this device. The first one is the axial phase where the current sheath is accelerated along the anode due to the JxB force, where J is the current flowing through the plasma sheath and B is the magnetic field. The second one is the radial phase where the moving current is collapsed into the pinch phase at the end of the anode length [43]. During the operation, in axial phase current is allowed to increase at peak value as the capacitor is discharged to its peak at first half cycle. Then the current suddenly decreases as the moving sheath undergoes into the radial phase. The JxB force squeezes the current sheath to a pinch plasma column where burst of multi radiation occurs in a scale of nanoseconds [43]. The sequence of events in pinch phase is depicted below where the variation of plasma sheath in radial phase with time is represented with the maximum compression at t=0 ns (Fig. 2).

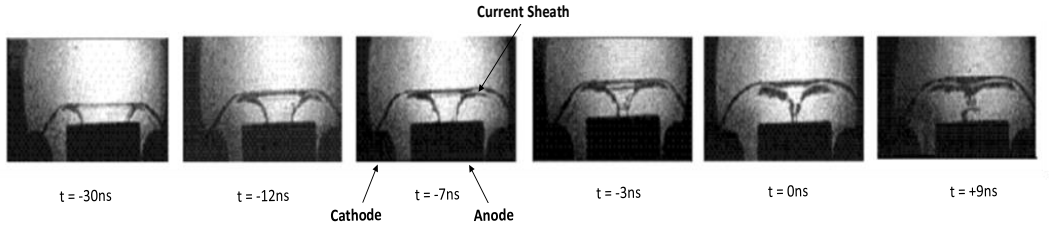

Fig. 2. Shadow graphic sequence of plasma column compression in radial phase in UNU/ICTP PFF at 4.0 mbar deuterium pressure [4].

3. THE LEE MODEL

The Lee model couples the electrical circuit of the DPF device with Plasma Focus dynamics, thermodynamics, and radiation enabling a realistic simulation of all gross focus properties [4]. This Model composed of axial and radial phases primarily. The radial phase is then composed of another four phases such as- radial inward shock phase, radial reflected shock phase, slow compression (radiative) phase and expanded column axial phase. The axial phase is described via snowplow model and radial phases are described via elongating slug model [4].

For axial phase, system model equations consists of equation of motion of the plasma sheath and circuit equation of the device [4].

The equation of motion of the plasma sheath which is obtained using snowplow model is given by

$$\rho_0\pi(c^2-1)a^2 f_m \frac{d}{dt}\left(z\frac{dz}{dt}\right) = \frac{\mu f_c^2}{4\pi}(\ln c)I^2. \quad (1)$$

Where $c = \frac{b}{a}$, I total current of the circuit, ρ_0 density of filling gas

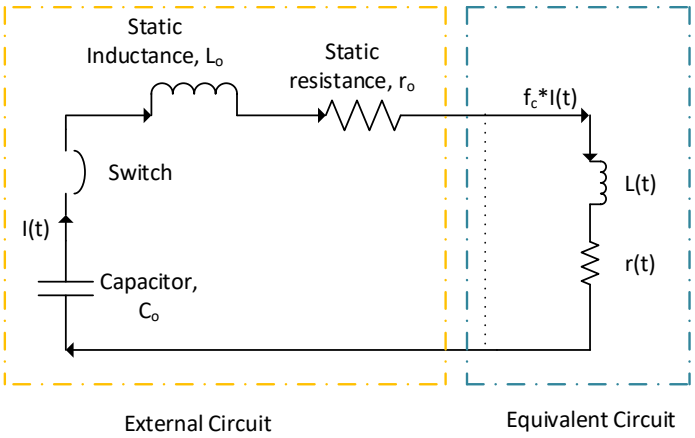

Fig. 3: Schematic electrical circuit diagram for DPF device in Lee Model. [Here $I(t)$ is the circuit current, $L(t)$ & $r(t)$ are dynamic inductance and dynamic resistance respectively.]

The device can be represented with a circuit diagram. The Circuit equation of the model comes from this circuit (Fig. 3). The equation is simply the voltage law of Kirchhoff in C_0-L_0-$L(t)$-r_0 loop.

$$\frac{d}{dt}[(L_0 + Lf_c)I] + r_0 I = V_0 - \int \frac{Idt}{C_0} \quad (2)$$

Where V_0 is the capacitor voltage, L_0 is the static inductance, r_0 is the static resistance of the circuit, $L(t)$ and $r(t)$ are dynamic inductance and resistance and $L = \frac{\mu}{2\pi}(\ln c)z$.

Equation (1) & (2) are the generating equations of the model. They contain the physics built into the model. They are coupled equations. The equation of motion is affected by the electric current

I. The circuit equation is affected by the current sheath motion dz/dt and position z. They can be integrated to get the instantaneous values of I and z.

The radial phase (Fig. 1, right side) is described via four coupled equations [4]. In this phase, less mass loss occurs due to compression configuration, so radial mass swept-up factor f_{mr} is introduced in this phase.

The first equation computes the radial inward shock speed from the driving magnetic pressure which is given by-

$$\frac{dr_s}{dt} = -\left\{\frac{\mu(\gamma+1)}{\rho f_{mr}}\right\}^{1/2} \frac{f_c I}{4\pi r_p} \tag{3}$$

The second equation computes the axial elongation speed of the column.

$$\frac{dz_f}{dt} = \frac{2}{\gamma+1}\frac{dr_s}{dt} \tag{4}$$

The third equation computes the speed of the current sheath (magnetic piston), allowing the current sheath to separate from the shock front by adiabatic approximation [4].

$$\frac{dr_p}{dt} = \frac{\frac{2}{\gamma+1}\left(\frac{r_s}{r_p}\right)\frac{dr_s}{dt} - \frac{r_p}{\gamma I}\left(1-\frac{{r_s}^2}{{r_p}^2}\right)\frac{dI}{dt} - \frac{1}{\gamma+1}\frac{r_p}{z_f}\left(1-\frac{{r_s}^2}{{r_p}^2}\right)\frac{dz_f}{dt}}{\frac{\gamma-1}{\gamma}+\frac{1}{\gamma}\frac{{r_s}^2}{{r_p}^2}} \tag{5}$$

The fourth equation is the circuit equation for radial phase.

$$\frac{d}{dt}[(L_0 + Lf_c)I] + r_0 I = V_0 - \int \frac{Idt}{C_0} \tag{6}$$

Where, r_p radial piston position, r_s radial shock front position, z_f axial piston position, γ specific heat ratio for filling gas and $L = \frac{\mu}{2\pi}(\ln c)z_0 + \frac{\mu}{2\pi}\left(\ln\frac{b}{r_p}\right)z_f$.

Equation (3)-(6) can be integrated to find the instantaneous values of r_p,r_s,z_f and I. Based on the system model equations (1)-(6) all plasma focus properties are calculated and determined by the code.

4. FITTING PROCEDURE OF DPFS IN LEE CODE

The Code is configured in such a way that it can work for any plasma focus device. This is done by inserting some parameters into the code. To fit a plasma focus device in Lee Model Code one has to able to input and manipulate four kinds of parameters as given in Table 1 with classification. These parameters are-

a. Bank Parameters, b. Tube Parameters, c. Operation Parameters, d. Model Parameters

Table 1: Parameters and their classifications

Bank Parameters	**Operational Parameters**
Capacitance of the capacitor banks, C_0	Charging voltage of capacitor banks, V_0
External or Static inductance, L_0	Fill pressure of the filling gas, P_0
Circuit resistance, r_0	Atomic number of filling gas, A
	Molecular Weight, MW
	Dissociation number, $At-1\ mol-2$
Tube Parameters	**Model Parameters**
Outer electrode or cathode radii, b	Axial mass swept-up factor, f_m
Inner or anode radii, a	Axial current factor, f_c
Anode length, z_0	Radial mass swept-up factor, f_{mr}
	Radial current factor, f_{cr}

At first, a discharge current waveform for a specific DPF machine is collected from laboratory experiment. Then the code is configured with the bank, tube and operational parameters of that machine. Secondly model parameters are varied to fit the computed total current profile to the measured total current profile. Because it has been found that the current profile/waveform of the plasma focus is one of the best indicators of gross performance of the device [4]. Fitting of the current profile is followed by two steps: fitting of axial phase and fitting of radial phase. The axial phase is fitted by maintaining three points on the measured current profile such as current rise slope, topping profile and peak value (Fig. 3). The radial phase is fitted by the matching of two points, slope of dip and bottom of dip in the measured current profile (Fig. 3).

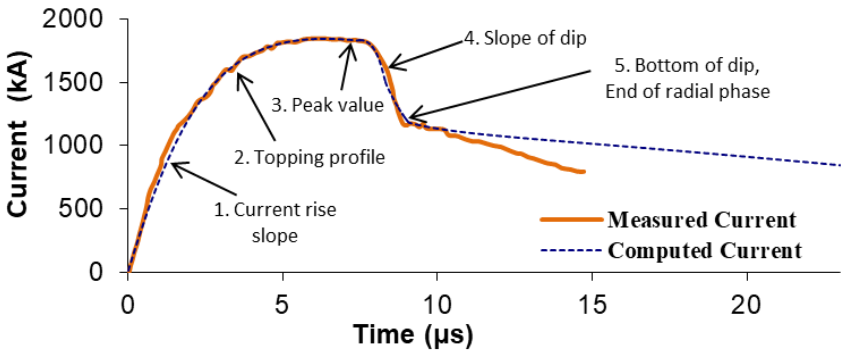

Fig. 3: The 5-point fitting of computed current profile to measured current profile. [4]

4.1 Fitting of axial phase

The axial phase starts from the bottom of the anode where plasma sheath starts to move in axial direction and is finished when the current sheath reaches to the end of the anode. Maximum

energy will transfer into the focus pinch, when the current rises to I_{peak} at the anode top (Fig. 3). Therefore to get an exact fitting of axial phase in current profile, manipulation of f_m and f_c is required as necessary. By varying these two parameters one needs to observe the changes that appear on the total current (I_{total}) profile. In this case, the current rise-time, rising shape and peak current (I_{peak}) are observed and compared with the profile of measured I_{total} (Fig.3). But manipulation of these two model parameter has intrinsic significance. Without understanding the internal plasma dynamics, it is not possible to fit the computed I_{total} profile with the measured profile of I_{total}. In the following subsection fitting procedure using model parameters is discussed.

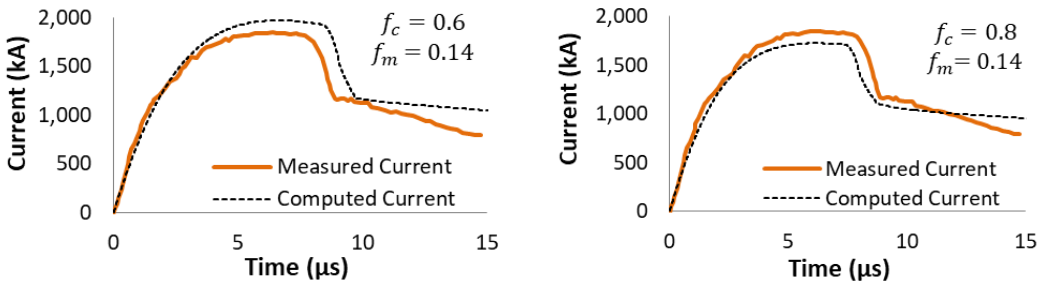

Fig. 4: Effect of f_c in computed total current profile, keeping f_m constant.

4.1.1 Change of f_c

Change of f_c means the change of the fraction of current which actually moves with the moving current sheath in the axial phase. If f_c increases by keeping f_m constant, the amount of current flow increases. It means that tube inductance also increases. Thus the current rising slope flattens and the axial phase duration decreases (Fig. 4). The decrement of f_c has reverse effects as stated above.

4.1.2 Change of f_m

Change of f_m means the change of the fraction of mass of the filling gas which actually moves with the moving current sheath in the axial phase. A decrease in f_m will show the similar effect in increasing f_c and vice versa (Fig. 5). But changing f_m does not incorporate any tube inductance. Hence, increasing f_c and decreasing f_m at the same time will not produce a current profile same as previous.

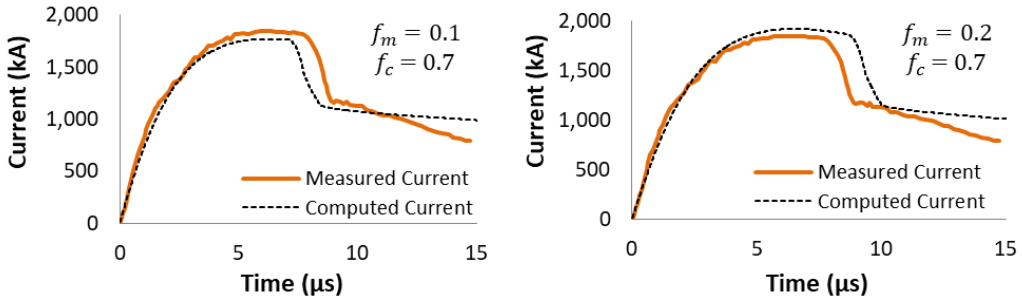

Fig. 5: Effect of f_m in computed total current profile, keeping $f_c$constant.

4.2 Fitting of the Radial Phase

The termination of the axial phase is initiation of the radial phase. It means that when the current raises its peak value then it starts to fall down and the radial phase begins. Radial phase includes shocking and compression of current sheath. These phenomena start the rolling over of current sheath. Dipping and sharp dipping in the current profile are found as the focus dynamics enters the pinch phase. Hence, fitting of the radial phase includes the fitting of the current dipping slope and the end of the dip (Fig. 3). This is done by changing the model parameters f_{mr} and f_{cr} as given in the following subsection. The two model parameters f_{m} and f_{c} related with axial phase will be kept constant at $f_m = 0.14$ and $f_c = 0.7$ during the fitting in radial phase. These values of f_m and f_c are obtained during fitting current profile in axial phase.

4.2.1 Change of f_{mr}

Change of f_{mr} affects the slope of the current dip. Increase in f_{mr} decreases the slope and vice versa (Fig. 6). In this case, f_{cr} is kept constant at the value of 0.7. This decrement occurs due to the velocity of the radial phase decreases with the increase of f_{mr}. As the velocity decreases the inductive load of the radial phase also decreases.

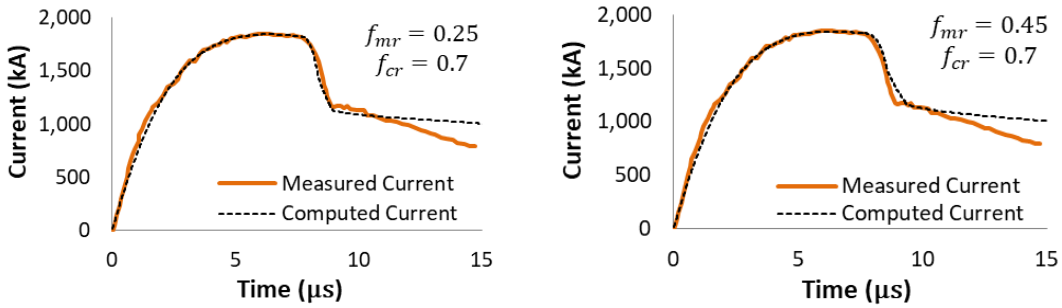

Fig. 6: Effect of f_{mr} in computed total current profile, keeping f_{cr} constant.

4.2.2 Change of f_{cr}

During the radial phase fitting, increasing f_{cr} decreases the end time of radial phase and vice versa. This means by increasing f_{cr} one is able to deepen the bottom of the dip and by decreasing flatten the bottom of the dip of the current profile (Fig. 7). This can be explained as such if the amount of current passing through the pinch (I_{pinch}) is relatively low then most of the remaining current goes unaffected by the pinch. Thus the dip of I_{total} profile becomes flatten. Increase of f_{cr} also increases I_{pinch} which works on the dip of I_{total} profile other way around.

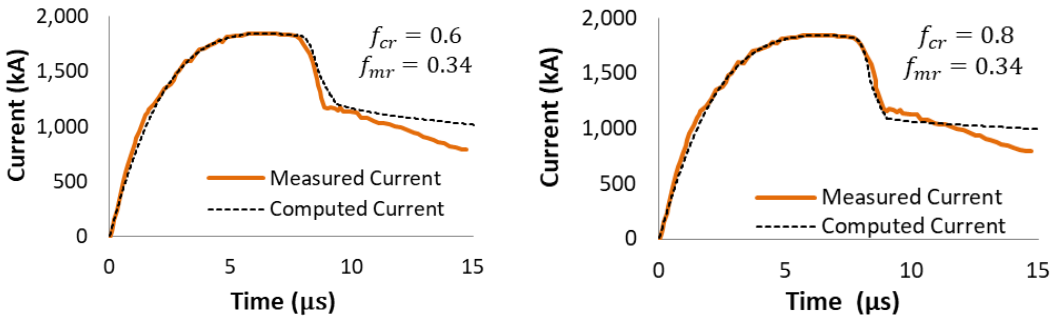

Fig. 7: Effect of f_{cr} in computed total current profile, keeping f_{mr} constant.

Based on the fitting principle by model parameters f_m,f_c,f_{mr} and f_{cr} a concise table is developed for fitting computed I_{total} with the measured I_{total}.

Table 2: Change of model parameters and associated actions

Model parameters	Actions
f_m increase	➢ Axial speed decrease. ➢ Dynamic resistance of the tube decrease. ➢ Current flow increase due to low resistance. ➢ Axial speed tends to increase due to current increase. ➢ Overall current rise slope decrease. ➢ Time of axial phase end or radial initiation increase.
f_c increase	➢ Current flow increase. ➢ Axial speed increase. ➢ Time of radial initiation decrease.
f_{mr} increase	➢ Radial phase speed decrease. ➢ Dip slope steepness decrease. ➢ Computed dip arrival time increase.
f_{cr} increase	➢ Radial phase speed increase. ➢ Computed dip arrivals time decrease. ➢ Bottom of the dip deepens.

5. SUMMARY

Dense plasma focus is a compact, powerful device for high energy particles and radiations. It has numerous applications such as- material modification, substance detection, neutron activation analysis, medical neutron therapies, lithography, micromachining and so on. To predict and simulate the properties of this device Lee code is used. Numerical experiment can be carried out using this code by fitting any DPF device.

The paper presents the description of DPF device and Lee code. Then fitting procedure of any DPF device in the code has been presented with a systematical approach. To fit, four types of parameters such as f_m,f_c,f_{mr} and f_{cr} are needed to insert and manipulate in the code. For a specific machine, bank, tube and machine parameters are used for a specific operational condition. Then model parameters are varied sequentially until a best match is found between computed and measured total current profile of the machine. Thus, the Lee code is configured and made ready to run numerical experiment for a specific machine.

This paper is a preliminary documentation for those who are new in the area of dense plasma focus research. It will work as a quick guide for fitting any DPF device in Lee code for any research purpose. Further study requires the manipulation of bank, tube and operation parameters for any new device design and simulation. Future work will be aimed at optimization of neutron production for the application of the neutron in radio isotope production.

REFERENCES

[1] N. V Filippov, T. I. Filippova and V. P. Vinogradov, Nucl. Fusion, **2**, 577(1962).

[2] J. W. Mather, Phys.Fluids, **8**, 366 (1965)

[3] S. Lee, Plasma focus model yielding trajectory and structure. In Radiations in Plasmas, McNamara, B.,Ed.; World Scientific, Singapore:; Volume II, pp. 978–987, (1984).

[4] S. Lee, Radiative Dense Plasma Focus Computation Package: RADPF http://www.plasmafocus.net

http://www.plasmafocus.net/IPFS/modelpackage/File2Theory.pdf

http://www.plasmafocus.net/IPFS/modelpackage/File1RADPF.htm

[5] L. Soto,Plasma Phys. Control. Fusion **47**,A361–A381, (2005).

[6] S. Lee, R. S. Rawat, P. Lee, and S. H. Saw,JOURNAL OF APPLIED PHYSICS **106**, 023309-1, (2009).

[7] S. Lee, Plasma focus model yielding trajectory and structure. In Radiations in Plasmas, McNamara, B., Ed.; World Scientific, Singapore: (1984); Volume II, pp. 978–987.

[8] S. Lee, S. P. Moo, C. S. Wong, A. C. Chew. Twelve Years of UNU/ICTP PFF- A Review. IC/98/231, ICTP Preprint, International Centre for Theoretical Physics, Trieste, Italy (1998), 101 pages

[9] J. M. Koh, R. S. Rawat, A. Patran, T. Zhang, D. Wong, S. V. Springham, T. L. Tan, S. Lee and P. Lee, Plasma Sour. Sci. Tech., **14**, 12 (2005).

[10] S. Lee, T. Y. Tou, S. P. Moo, M. A. Eissa, A. V. Gholap, K. H. Kwek, S. Mulyodrono, A.J. Smith, Suryadi,W.Usala, M. Zakaullah. A simple facility for the teaching of plasma dynamics and plasma

nuclear fusion. Amer J. Phys., USA, **56**, 62-68 (*1988)*.

[11] D. E. Potter, The formation of high-density z-pinches. Nucl. Fusion**, 18**, 813–823, (1978).

[12] S. Lee, 2000–2007. [Online]. Available: http://ckplee.myplace.nie.edu.sg/ plasmaphysics/

[13] S. Lee, P. Lee, G. Zhang, X. Feng, V. A. Grinkov, M. Liu, A. Serban, T.Wong, IEEE Trans. Plasma Sci. **26**, 135 (1998).

[14] Muhammad ShahidRafique. PhD thesis (in preparation) NTU, Singapore

[15] S. Lee and A. Serban A, "Dimensions and lifetime of the plasma focus pinch," IEEE Trans. Plasma Sci., **24**(3), 1101-1105, (*1996)*.

[16] M. H. Liu. Soft X-Rays from Compact Plasma Focus. PhD thesis. NTU, Singapore, (1997).

[17] S.Lee, P.Lee, G.Zhang, X. Feng, V.Gribkov, M.Liu, A.Serban& T.K.S. Wong. High Repetition High Performance Plasma Focus as a Powerful Radiation Source- IEEE Trans Plasma Science **26**(4) 1119- 1126 (1998).

[18] G.X.Zhang. Plasma Soft x-ray source for Microelectronics lithography. PhD thesis, NTU, Singapore (1999).

[19] S. Lee, V. Kudryashov, P. Lee, G.Zhang, A. Serban, X. Feng, M. Liu, and T. K. S. Wong. Lithography Using a Powerful Plasma Focus Soft X-ray Source. International Congress on Plasma Physics, Prague, Czech Republic, (1998).

[20] D. Wong, P. Lee, T. Zhang, A Patran, T. L. Tan, R. S. Rawat and S. Lee, "An improved radiative plasma focus model calibrated for neon-filled NX2 using a tapered anode," Plasma Sources Sci. Technol. **16**, , pp. 116-123, (2007).

[21] E. P. Bogolyubov, V. D. Bochkov, V. A. Veretennikov, L. T. Vekhoreva, V. A. Gribkov, A. V. Dubrovskii, Yu P Ivanov, A. I. Isakov, O. N. Krokhin, P. Lee, S. Lee, V. YaNikulin, A Serban, P. V. Silin, X. Feng and G. X. Zhang, "A powerful soft x-ray source for x-ray lithography based on plasma focusing" Phys. Scripta., **57**, 1998, pp. 488-494, (1998).

[22] V. Siahpoush, M. A. Tafreshi, S. Sobhanian and S. Khorram, "Adaptation of Sing Lee's model to the Filippov type plasma focus geometry," Plasma Phys. Control. Fusion **47**, pp. 1065-1072, (2005).

[23] S. Lee and S.H. Saw "Neutron scaling laws from numerical experiments," J. Fusion Energy, **27**(4), pp. 292–295, (2008).

[24] S. Lee "Current and neutron scaling for megajoule plasma focus machines," Plasma Phys. Control. Fusion, **50**(10), p. 105 005 (14pp), (2008).

[25] S. Lee and S. H. Saw "Pinch current limitation effect in plasma focus," Appl. Phys. Lett., **92**(2), p. 021 503, (2008).

[26] S. Lee S, P. Lee, S. H. Saw and R.S. Rawat, "Numerical experiments on plasma focus pinch current limitation," Plasma Phys. Control. Fusion, **50**(6), 065 012 (8pp), (2008).

[27] V. A. Gribkov, A. Banaszak, S. Bienkowska, A.V. Dubrovsky, I. Ivanova-Stanik, L. Jakubowski, L. Karpinski, R.A. Miklaszewski, M. Paduch, M.J. Sadowski, M. Scholz, A. Szydlowski and K. Tomaszewski "Plasma dynamics in the PF-1000 device under fullscale energy storage: II. Fast electron and ion characteristics versus neutron emission parameters and gun optimization perspectives," J. Phys. D,Appl. Phys., **40** (12), 3592–3607, (2007).

S. Lee, S. H. Saw, P. C. K. Lee, R. S. Rawat and H. Schmidt, "Computing plasma focus pinch current from total current measurement," Appl. Phys. Lett. **92** , 111501, (2008).

[28] M. Akel, Sh. Al-Hawat, S. Lee "Pinch Current and Soft x-ray yield limitation by numerical experiments on Nitrogen Plasma Focus". J. Fusion Energy DOI 10.1007/s10894-009-9238-6. First

online 21 August, (2009).

[29] S. H. Saw, P. C. K. Lee, R. S. Rawat& S. Lee 'Optimizing UNU/ICTP PFF Plasma Focus for Neon Soft X-ray Operation' IEEE Trans on Plasma Sc, 37, 1276-1282, (2009).

[30] S. H. Saw and S. Lee "Scaling laws for plasma focus machines from numerical experiments". Invited paper: IWPDA, Singapore 2&3 July (2009).

[31] S. H. Saw and S. Lee "Scaling the plasma focus for fusion energy considerations". Tubav Conferences: Nuclear & Renewable Energy Sources, Ankara, Turkey, 28 & 29 September (2009).

[32] S. Lee "Nuclear fusion and the Plasma Focus", Invited paper Tubav Conferences: Nuclear & Renewable Energy Sources Ankara, Turkey, 28 & 29 September (2009).

[33] S. Lee, S. H. Saw, P. Lee & R. S. Rawat, "Numerical Experiments on Neon plasma focus soft x-rays scaling", Plasma Physics and Controlled Fusion, 51, 105013 (8pp) , (2009).

[34] M. Akel, Sh. Al-Hawat, S. Lee "Numerical Experiments on Soft X-ray Emission Optimization of Nitrogen Plasma in 3 kJ Plasma Focus SY-1 Using Modified Lee Model", J Fusion Energy DOI 10.1007/s10894-009-9203-4 First online, May 19, (2009).

[35] S. Lee, R. S. Rawat, P. Lee, S. H. Saw, Soft x-ray yield from NX2 plasma focus, JOURNAL OF APPLIED PHYSICS, 106, 023309, (2009).

[36] S. Lee Diagnostics and Insights from Current waveform and Modelling of Plasma Focus. Keynote address: IWPDA, Singapore, (2009).

[37] S. Lee "Neutron Yield Saturation in Plasma Focus-A fundamental cause" APPLIED PHYSICS LETTERS, 95, 151503 published online 15 October, (2009).

[38] P. Gautam, R. Khanal, S. H. Saw and S. Lee. IEEE Trans Plasma Sci, Vol 45 Issue 8, 2292-2297 (2017)

[39] A. Singh, S. Lee, S. H. Saw IEEE Trans Plasma Sci Vol 45 issue 8 2286-6691 (2017)

[40] M. Akel , S. H. Saw , S. Lee, IEEE Trans Plasma Sci, Vol 45 issue 8, 2303-2307 (2017)

[41] L. K. Lim, S. L. Yap, L. H. Lim, Y. S. Neoh, M. Z. Khan, S. K. Ngoi, S. S. Yap, S. Lee J Fusion Energy, Volume 35, Issue 2, pp 274–280 DOI 10.1007/s10894-015-0014-5 (2016)

[42] M. Akel, S. Alsheikh Salo, Sh. Ismael, S. H. Saw, and S. Lee, J Fusion Energy , 35(4) 694-701 DOI 10.1007/s10894-016-0092-z, 2016. first online 21 April (2016).

[43] J.A. Bittencourt, Fundamentals of Plasma Physics. Springer. p. 1. ISBN 9780387209753 (2004).

*Bangladesh Journal of Physics, **23 & 24**, 95-104, 2018*

ANALYSIS OF NEUTRONS AND GAMMA RAYS DOSES OF A FISSION REACTOR WITH DIFFERENT THERMAL POWERS

M. S. HOSSAIN[1], A. S. MOLLAH[2], MEHERUN NAHAR[3], M. N. ISLAM[1] AND A. K. M. F. HOQUE[4]

[1]*Department of Physics, Bangladesh Army University of Engineering & Technology (BAUET), Qadirabad Cantt. Natore, Bangladesh*

[2]*Department of Nuclear Engineering and Technology, Military Institute of Science and Technology, Dhaka, Bangladesh*

[3]*Bangladesh Atomic Energy Regulatory Authority, Dhaka, Bangladesh*

[4]*Department of Physics, Tejgaon College, Farmgate, Dhaka, Bangladesh*

** Corresponding author: E-mail: dfhoque@gmail.com, drsazzad.bauet@gmail.com*

Received on 09.01.2018, Revised received on 06.09.2018, Accepted for publication on 29.09.2018

ABSTRACT

Neutrons and gamma rays flux and dose values have been calculated for PWRs and BWRs using a visual basic computer programme developed for the purpose. Calculations are made considering standard core volume and power density of the core but varying thermal powers within the range 600 MW to 1800 MW. Flux and dose values both for PWRs and BWRs are obtained from the calculation of fission rate of ^{235}U. In the present work, several volumes of the core and multilayer combinations give the option to choose the suitable combination for any nuclear power reactor. The calculations so performed will be, in general, useful for calculation of the biological shielding of a power reactor.

1. INTRODUCTION

A nuclear reactor is a prolific copious source of potentially dangerous nuclear radiation [Fig. 1]; it is unavoidable too, since most of the radiation released originates with the emission process itself. In addition to the energetic neutrons and gamma rays that are emitted simultaneously with the fission event, the fission fragments formed are highly radioactive nuclides that emit α, β and γ radiation. There are several sources of radiation to be considered [1,2]. These are prompt fission neutrons, delayed fission neutrons, prompt fission γ-rays, fission product decay γ-rays, inelastic γ-rays, capture γ-rays and activation γ-rays. That nuclear radiation can be injurious to man is beyond dispute, and to enable personnel to work in the vicinity of an operating reactor, it is necessary to absorb the nuclear radiation released in a thick shield surrounding the core, in order to reduce the radiation dose level to a tolerable level in the region beyond the shield. A thorough analysis on biological shielding was done by M. S. Hossain et al. [3,4].

Nuclear reactor is a continuous source of ionizing radiation. Shields must be placed around a nuclear reactor and at various points in a nuclear power plant in order to protect operating personnel and the public at large from the radiations emanating from the installation. Reactor shields may be designed for several functions. An integral part of instituting any radiological

protection program is the establishment of biological shielding for the control of ionizing radiation and individual radiation exposures.

The designation and extent of such arrangements should be based on sources of radiation exposure to individuals, potential pathways for radiation exposure to individuals from routine activities and from postulated credible accident conditions, available shielding and methods to control radiation exposure. It is used to keep the dose limit to permitted level exposed to occupational and public surrounding the reactor. According to International Commission on Radiological Protection (ICRP) report number 60 and report number 75, the recommended dose limit for occupational exposures has decreased to20 mSv/year [5, 6]. This can be achieved only by installing biological shielding around the reactor core. By knowing the characteristics of the reactor core, thermal shielding, and reactor vessel the size of the reactor biological shield can be estimated. The objective of this study is to calculate the radiation doses due to gamma-rays and neutrons at the edge of biological shield of a nuclear reactor.

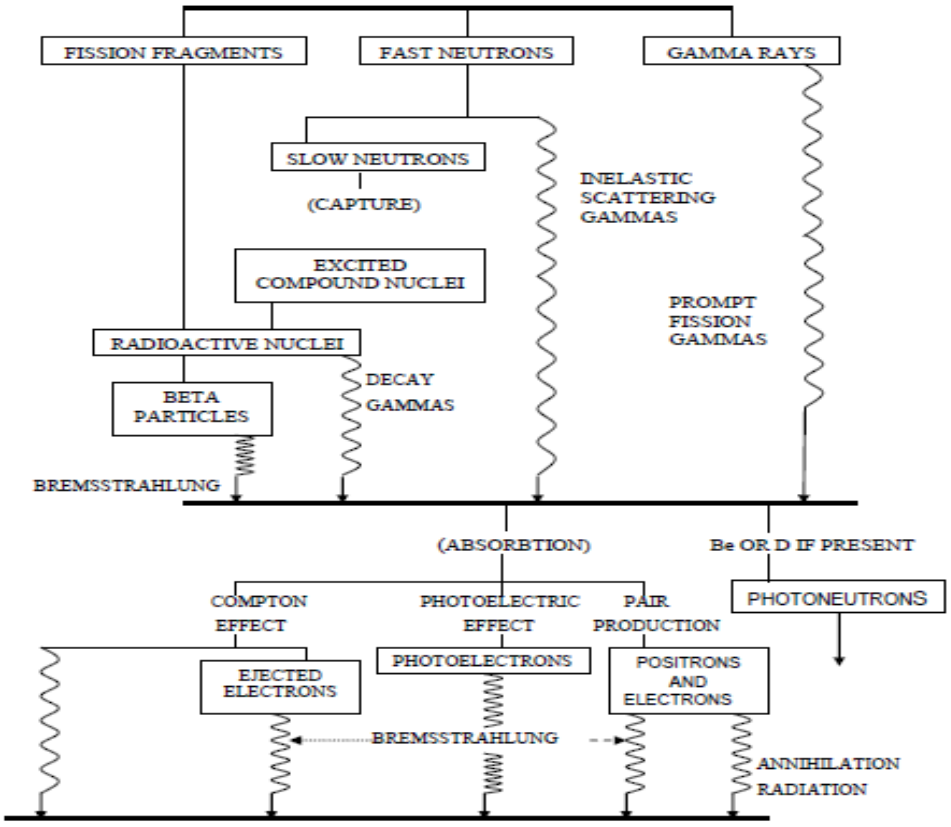

Fig. 1. Sources of radiations from a Nuclear Power Reactor [2].

1.1 Nuclear power reactors

The reactor most widely used in the world today for producing electric power is the thermal reactor, which is moderated, reflected, and cooled by ordinary (light) water, as water has excellent moderating and thermodynamic properties and it is readily available at little cost. On the other hand, water has a high vapor pressure, which means that light water reactors (LWRs) must be operated at high pressures. Basically two types of light water reactors are in use now pressurized water reactor (PWR), and boiling water reactor (BWR).

In the PWR water enters into the pressure vessel at a temperature of about 290 ^{0}C, flows down around the outside of the core where it serves as a reflector, passes upward through the core where it is heated, and then exits from the vessel with a temperature of about 325 ^{0}C. The water in a PWR is maintained at a high pressure, approximately 15 MPa. At this pressure the water will not boil, at least not to any great extent.

Since the water does not boil in the reactor, the steam for the turbines must be produced external to the reactor. This is done in steam generators, which are heat exchangers with pressurized water on the hot side. High pressure, heated coolant water from the reactor enters at the bottom and passes upward and then downwards through several thousand tubes each in the shape of an inverted U. This is a heterogeneous reactor that uses slightly enriched uranium as fuel and light water as moderator and coolant. The core is contained in a cylindrically shaped pressure vessel under a pressure of 1000 to 2000 pounds per square inch (15 MPa) along with the core support structures, the control rod clusters and other parts directly associated with the core. PWRs keep water under pressure so that it heats, but does not boil. Water from the reactor and the water in the steam generator that is turned into steam never mix. In this way, most of the radioactivity stays in the reactor area.

In the BWR, water is allowed to boil at high pressure. In the BWR the steam is formed in the reactor itself and goes directly to the turbines –steam generators in separate heat transfer loop are not necessary as they are with the PWR. For this reason, the BWR is said to operate in a direct cycle. The pressure in a BWR is approximately 7 MPa, about one-half the pressure in a PWR. As a result, the wall of the pressure vessel for a BWR need not be as thick as it is for a PWR. However, it turns out that the power density (watts/cm^3) is smaller in a BWR than in a PWR, so the overall dimensions of a pressure vessel for a BWR must be larger than for a PWR of the same power. As far as the cost of the pressure vessel is concerned, these two effects more or less tend to offset one another.

The development of the boiling water reactor started somewhat later than the pressurized water reactor. The BWR is essentially similar to the PWR. It uses light water for both moderator and coolant and it uses enriched uranium fuel in the form of small ceramic pellets of uranium di oxide in zircaloy tubes. The spacing between the fuel rods is slightly larger than in the PWR. Therefore, the volume of core of BWR is larger than the PWR, both having the same thermal power. Hence the power density of BWR is smaller. The main difference between the two reactor types is that in the PWR the light water coolant is artificially pressurized to stop it boiling whereas in BWR it is not. The pressure in the reactor is much less than the pressure in a PWR, which produces steam at the same conditions. The pressure in the BWR system is maintained at about 72.5 bar. The thickness of the pressure vessel in BWR does not necessarily need to be as thick as in PWR. Fig. 2 shows the design layout of a nuclear power plant.

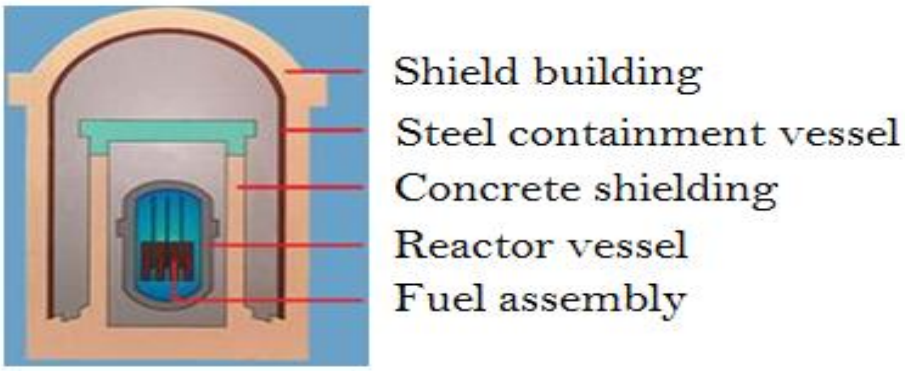

Fig. 2. Design layout of a nuclear power plant (PWR).

2. TOTAL RADIATION IN A NUCLEAR POWER REACTOR

Many of the physical measurements and most of the practical shielding applications actually involve the energy spectrum of all fission neutrons and gammas, both prompt and delayed. Radiation sources are considered here to be materials, which emit either neutrons or gamma photons. The measure of the strength of a source is its rate of emission, i.e., flux or dose. The source strength is measured in terms of the flux or dose emission.

Radiations are classified as primary and secondary radiations. As has been discussed primary radiation results from nuclear fission: it includes the gamma radiation from the decay of the radioactive fission products. Secondary radiation includes all other sources of radiations including gamma radiation generated in the shield materials due to the interaction of the primary neutrons with the materials of the shield, this radiation is a decisive factor in determining the thickness of the reactor's outer shield. Fission radiations can be obtained from fission reactions and are given by

$$R_f = A_1 + A_2 + A_3 + A_4 + A_5 \quad (1)$$

where, R_f = Summation of total radiation, A_1 = Radiations from prompt fission neutrons N_{pn}, A_2 = Radiations from delayed fission neutrons N_{DN}, A_3 = Radiations from prompt fission gamma rays $N_{p\gamma}$, A_4 = Radiations from equilibrium fission product (decay) gammas Γ_t, and A_5 = Radiations from thermal neutrons capture.

Although the release of the primary neutron and gamma radiation is not distributed uniformly throughout the reactor core, for many practical computations it is adequate to assume it is, and to regard the core as a constant volume source of these radiations. This is a suitable point at which to establish some approximate formulae for neutron and gamma ray source strengths for a reactor releasing heat at a steady rate. Assuming that 2.5 fast neutrons are released per fission, then the volume source strength [2] of fast neutrons in the core is given by

$$S_{vn} = 7.8 \times 10^{16} \times (P/V) \text{ neutron cm}^{-3} \text{ s}^{-1} \quad (2)$$

where, S_{vn} is the neutron source strength in the reactor core, and (P/V) is the power density in watts per cubic centimeter.

Assuming that the total primary gamma radiation released per fission consists of 7.54 MeV from prompt and 7.6 MeV from fission products, the volume source strength [2] of primary gamma rays is given by

$$S_{v\gamma} = 2.18 \times 10^{17} \times (P/V) \text{ gamma photons/cm}^3\text{-sec} \quad (3)$$

where, P is the thermal power (in MW) of the reactor and V is the volume (in cm^3) of the core.

2.1 Flow diagram for the calculation procedure of neutrons and gamma rays

The volume source strength of neutron and gamma radiation in the core is calculated using Equs. (2 and 3). These equations are solved for total fission radiation, prompt fission gamma rays and neutron fluxes and doses to the surface of the reactor core edge. To calculate these parameters the values of volume of the core, core surface area, source strength of radiation per unit volume, S_v, fission neutron and fission gamma-ray fluxes are calculated and used. This is shown in the interface labeling of the designed programme. Fig.3.Input values of the programme calculations are shown by three blank boxes represented by X, Y and Z. Command button of the programme running, new calculation and shut down of the programme calculation is shown by C. Output calculated values from the programme are represented by R1 and R2.

The calculated values of the programme are shown in Fig. 4. Programme runningtypical input values and output results are shown. Among the three command buttons calculate button gives the result of calculation is shown. New command button will inter next new set of values and will give results of calculation accordingly. End command button will end the programme of calculation.

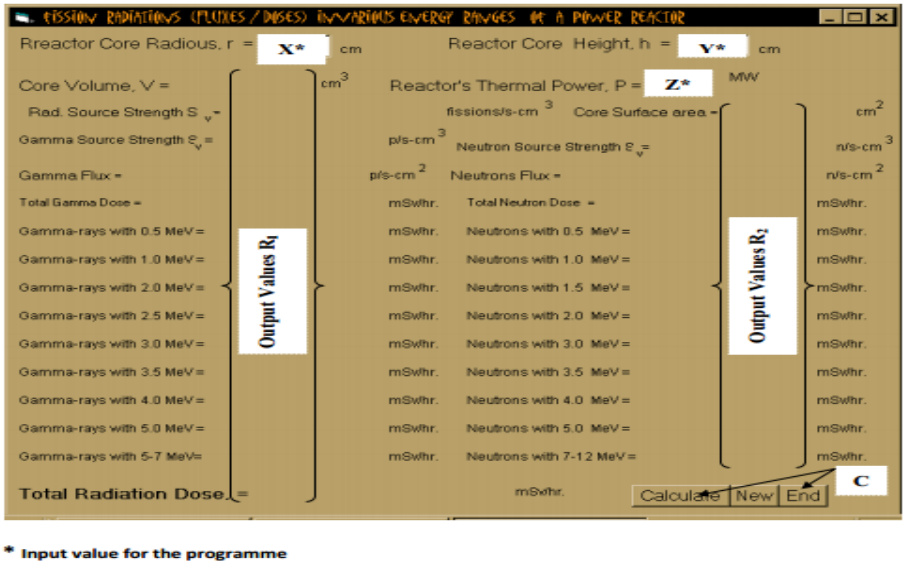

* **Input value for the programme**

Fig. 3. Programme labelling for fission radiations (flux and dose values) for a power reactor.

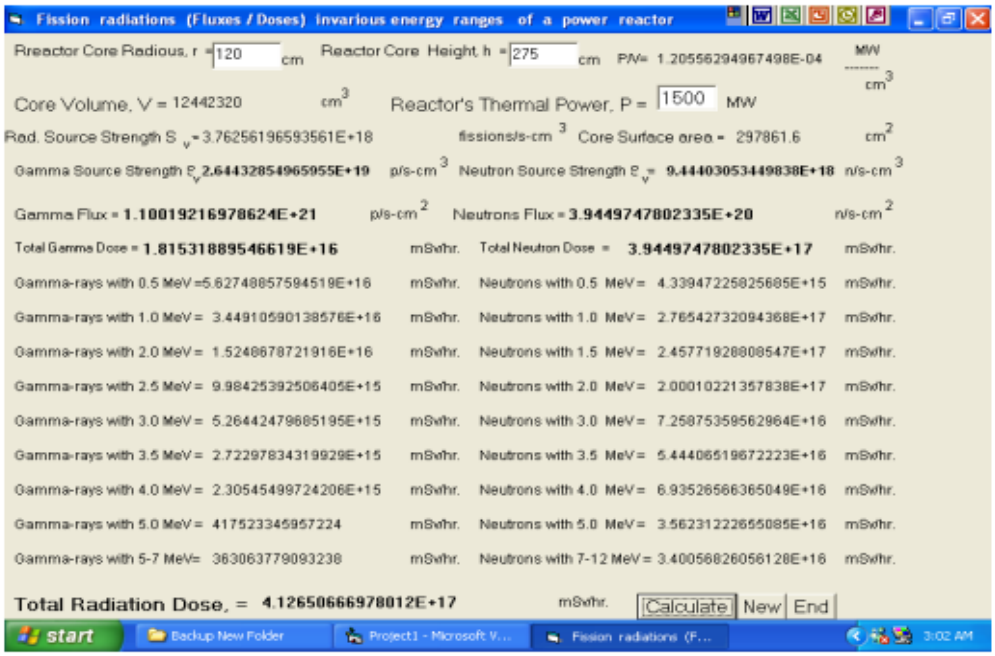

Fig. 4. Snapshot of calculation for flux and dose values from computer programme.

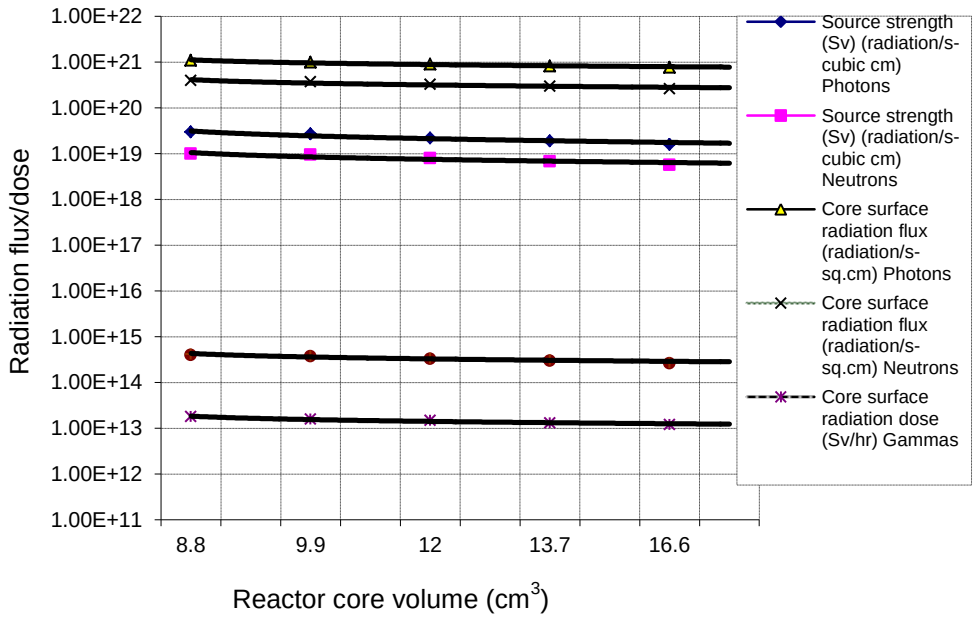

Fig. 5. Variation of radiation flux/dose on the core surface of a PWR of thermal power 1200 MW.

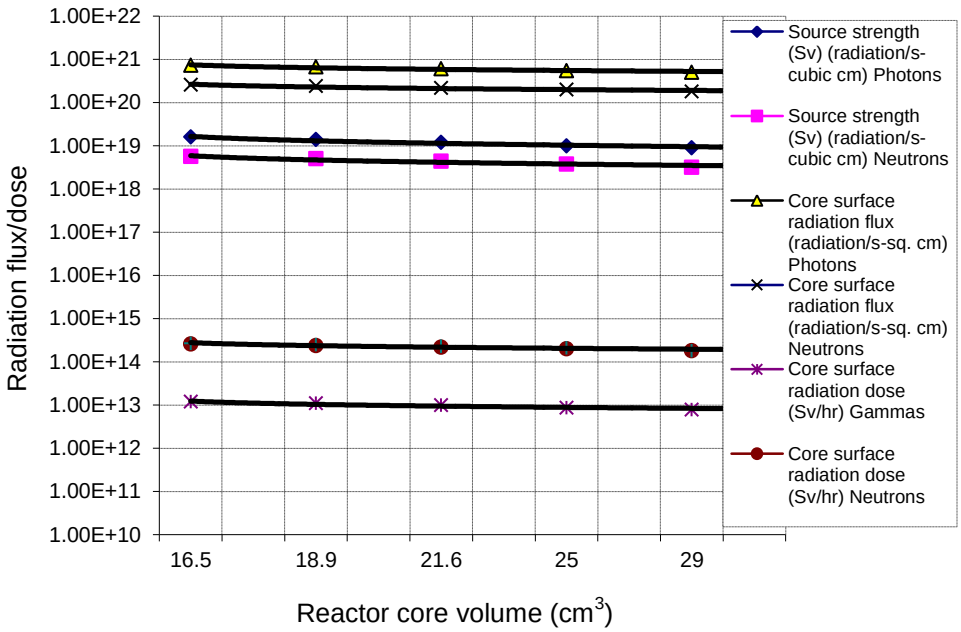

Fig. 6. Variation of radiation flux/dose on the core surface of a BWR of thermal power 1200 MW.

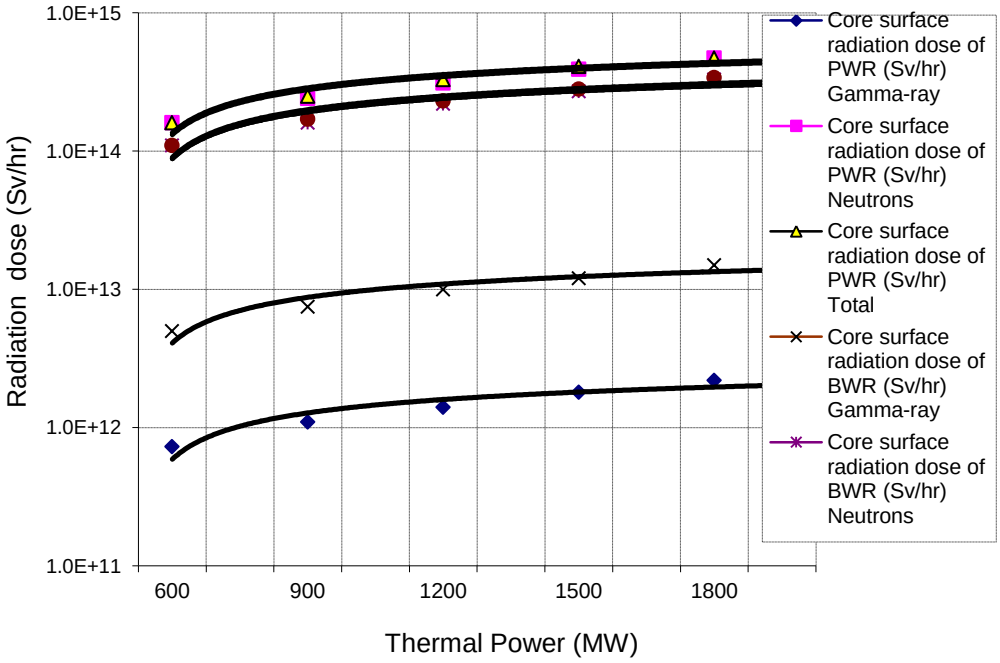

Fig. 7. Variation of radiation dose on the core surface of PWRs and BWRs.

3. RESULTS AND DISCUSSIONS

Because of the complexity of the radiation source and also of the power distribution in an operating core, calculations related to the core and vessel fluxes and subsequently the required biological shield thicknesses become hazardous. To face this situation, calculations have been done using a computer programme. The calculations are made at the edge of the core surface Fig. 2.

The rapid calculation done this way allows the user to fully explore design variations in order to optimize the shield design, as it was previously done using softwares RANKERN [7] and MCBEND [8] of British Nuclear Fuels Limited (BNFL). However, for present the calculations a software developed in the work was used Figs. 3 and 4.

The overall power density (watts/cm^3) of a PWR is higher than that of a BWR as the pressure vessel is comparatively smaller in PWR having the same power. In the work, values of total fission radiations (flux and dose) in the core are calculated both for a PWR and a BWR having different possible cylindrical core sizes. Calculations are made varying thermal powers as well in the range from 600 MW to 1800 MW. In future dose calculation of the biological shield will be carried out for multi-layers of shield combination.

3.1 Core surface flux and dose values

In the present study, nuclear power reactors (PWRs and BWRs) having thermal power values 600 MW, 900 MW, 1200 MW, 1500 MW and 1800 MW have been considered and the radiation source strength (S_v), fluxes and doses of radiation at the surface of the reactor core are calculated.

Figs. 5 and 6 show the results of variation of these quantities with the variation of core volume. The volume has been varied by varying radius and height of the reactor core keeping thermal power fixed at 1200 MW. The values of radiation source strength flux and dose decrease as core volume (PWRs and BWRs) is increased. For PWRs the values of total doses at the core surface are found to vary between 4.2×10^{14} Sv/hr and 2.7×10^{14} Sv/hr respectively for core volume values 8.8 m^3 and 16.6 m^3. For BWRs these values are respectively 2.7×10^{14} Sv/hr and 1.8×10^{14}Sv/hr for 16.5 m^3 and 29 m^3 of the core volume. Of these total dose values, neutron contribution is much larger than that of gammas – more than 20 times.

In case of PWRs the source strength due to photons becomes almost half with increase of the core volume by doubling in magnitude. Similar pattern is also observed for the BWRs. This ratio is again maintained for the case of neutrons. Variation pattern of such a nature is expected, as the thermal power has been kept unchanged in the calculation while the core volume has been increased allowing the photons (or neutrons) to be distributed in a wider volume and thus reducing the number of the sources per unit volume.

The core surface radiation flux due to photons has reduced obviously with the increase of core volume, but not by the same proportion. The ratio is now around 1.5 rather than becoming double while the core volume has been halved in magnitude. Of course, similar variation pattern is again observed in case of surface radiation flux due to neutrons. The core surface radiation dose values also vary similarly like the radiation flux. This pattern of variation is again same for both PWRs and BWRs.

3.2 Variation of source strength and core surface radiation with thermal power

Fig. 7 shows the calculated values of total fission radiations (flux and dose) in the core of PWRs and BWRs having standard cylindrical core sizes [9-10]. The core height and radius are mentioned in the table captions. These values have been taken from literature. For each value of the volume different thermal values, e.g., 600, 900, 1200, 1500 and 1800 MW were considered. Corresponding values of source strength, core surface radiation flux and core surface radiation dose have been calculated separately for gamma photons and neutrons.

The source strength, core surface radiation flux and core surface radiation dose values vary linearly with thermal power values for PWRs and BWRs for both gamma photons and neutrons. These results are expected. In case of source strength and radiation flux, gamma photon contribution is more than that of neutrons – nearly three times. Of course, the neutron contribution to the core surface radiation dose is larger than that of gammas; this time the ratio being around 22 times. These tables may help the reader to easily compare between the core surface radiation dose in a PWR and a BWR for the same thermal power. One may observe that for such a case the dose values are 1.42 – 1.48 times higher for PWRs than for BWRs. The above mentioned results are also evident from Figs. 5-7. In the calculations, the values of doses are separated according to the radiation emission per unit energy interval. These divisions of radiation doses are shown in Fig. 4.

4. CONCLUSIONS

In this study, the radiation source strength (S_v), fluxes and doses of radiation at the surface of the reactor core are calculated for different sizes (height, radius etc.). The values of radiation source strength, flux and dose decrease as core volume (PWRs and BWRs) is increased (Figs. 5-6). Of these total dose values, neutron contribution is much larger than that of gammas – more than 20 times. The source strength, core surface radiation flux and core surface radiation dose values vary linearly with thermal power values for PWRs and BWRs for both gamma photons and neutrons. Of course, the neutron contribution to the core surface radiation dose is larger than that of gammas. The results of this study could be used for estimation of biological shield of any nuclear power plant.

REFERENCES

[1] J. Wood, Pergamon Press, Oxford, “Computational Methods in Reactor Shielding”, 1982, p. 66-67.

[2] S. Glasstone and A. Sesonske, “Nuclear Reactor Engineering”, First Edition, 1986, p. 635.

[3] M S Hossain, M A Zaman, and A S Mollah, Jahangirnagar Physics Studies, “Dose Calculation for Biological Shield of a 600 MW Nuclear Power Reactor”, Vol. 13, 2007.

[4] M S Hossain, “A study on Biological Shielding Design and Analysis of Radiation Doses for a Nuclear Power Reactor” , Dept. of Physics, Jahanginagar University, Ph.D. Thesis, 2006.

[5] Annals of the International Commission on Radiological Protection (ICRP), Oxford Pergamon, Publication 75, Vol. 27, 1997.

[6] Annals of the International Commission on Radiological Protection (ICRP), Oxford Pergamon, Publication 60, Vol. 27, 1997

[7] RANKERN – A Point Kernel Package for the Assessment of Complex Gamma–Ray Shield, Developed in Collaboration with British Nuclear Fuels (BNFL), Yearly Report 2003.

[8] MCBEND – A Monte Carlo Package for Radiation Transport Problems in Shield, Dosimetry and Industrial Applications, Developed in Collaboration with British Nuclear Fuels (BNFL), Yearly Report 2003.

[9] Westinghouse Electric Corp. Reference Safety Analysis Report, RESAR-41, U.S. NRC Report DOCKET-STN-50480, 1974.

[10] Combustion Engineering Corp. Reference Safety Analysis Report, CESSAR, U.S. NRC Report DOCKET-STN-50470, 1974; General Electric Co. Standard Safety Analysis Report, GESSAR-238, U.S. NRC Report DOCKET-STN-50550, 1975.

*Bangladesh Journal of Physics, **23 & 24**, 105-113, 2018*

ANALOGY BETWEEN AC JOSEPHSON JUNCTION EFFECTS AND OPTICAL PHENOMENA IN SUPERCONDUCTORS

H.M.A.R. MARUF [1,*], M.R. ISLAM [2] AND F.-U.-Z. CHOWDHURY[1]

[1]*Department of Physics, Chittagong University of Engineering and Technology, Chittagong 4349, Bangladesh*

[2]*Department of Physics, University of Chittagong, Chittagong 4331, Bangladesh*

** Corresponding author:E-mail:hasnatmaruf@gmail.com*

Received on 24.01.18, Revised received on 16.11. 2018, Accepted for publication on 24.11.2018

ABSTRACT

A model of the multi-junction ac Josephson effect and its behaviour in parallel connection have been discussed. The effects of addition of two or more Josephson junctions have been investigated analogous to interference and diffraction phenomena in optics. Due to the addition of multi Josephson junction, the resultant current amplitude behaves like interference and diffraction phenomena in the absence and in the presence of the magnetic field. Finally, the possible applications of such phenomena associated with superconducting devices are suggested.

Keywords: AC Josephson effect, Interference and Diffraction Phenomena, Superconducting devices.

1. INTRODUCTION

A Josephson junction is a combination of two superconducting material layers separated by a thin layer of a non-superconducting material like, insulator, metal, etc. The Josephson effect is an interesting phenomenon in superconductivity and becoming a great research interest in science and technology [1, 2]. Many superconducting devices, like SQUID (superconducting quantum interference device, consist of one or two Josephson junctions), high-frequency oscillator, voltage standards, terahertz wave emission, ultrafast switching computer elements, etc., have been developed based on this effect [3-5]. Mainly there are two types of Josephson effects in superconductor, viz., dc and ac Josephson effect. The ac Josephson effect (the effect due to Josephson junction in presence of applied voltage) is responsible for the above mentioned types of superconducting devices. Here, to avoid complexity, the parallel combination of the ac Josephson junction has been taken. For parallel connection, the resultant current will simply be the vector sum of the current in each junction. If dc voltage V is applied to a Josephson junction, an alternating supercurrent of frequency $\omega_J = (2e/\hbar)V$ ($2e$ - a Cooper pair charge, $h = 2\pi\hbar$ is Planck's constant) flows through the junction which is given by

$$I = I_0 \sin(\omega_J t + \phi) \tag{1}$$

where, I_0 is the maximum current flowing through the junction and $\phi(=\delta_1-\delta_2)$ is the phase difference across the junction of superconductors S_1 sand S_2, schematically shown in Figure 1.

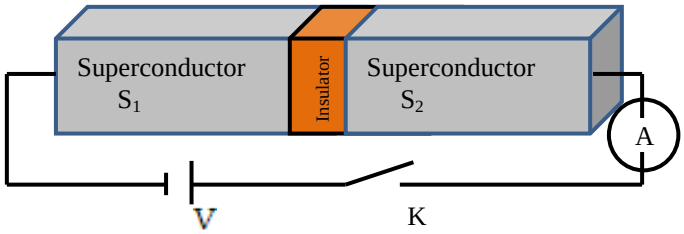

Fig. 1. Schematic diagram of ac Josephson junction. Both electrodes are connected to an external conventional circuit.

The effects of addition of two or more Josephson junctions (called multi-junction) have been investigated analogous to interference and diffraction phenomena in optics. Here, we have explained the amplitude and the intensity of the resultant current with the increasing number of junctions. In the following sections, a theoretical model is proposed for the addition of two or more ac Josephson junctions connected in parallel, which has been discussed in absence and presence of magnetic field.

2. THEORETICAL MODEL

Let us consider two ac Josephson junctions connected in parallel with an applied voltage (V) as shown Figure 2.

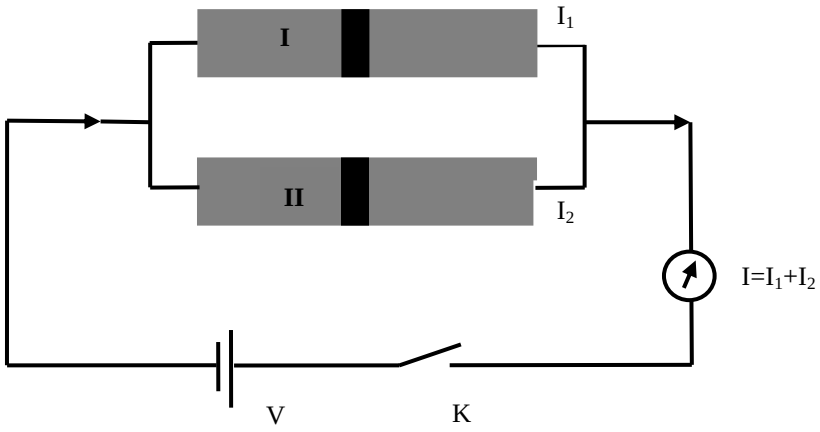

Fig. 2. Schematic diagram of two parallel Josephson junctions with a constant dc voltage (V).

Suppose the expressions for current I_1 and I_2 through the parallel Josephson junctions I and II, are respectively as follows:

$$I_1 = I_{01} e^{i(\omega_J t + \phi)} \tag{2}$$

and

$$I_2 = I_{02} e^{i(\omega_J t + 2\phi)} \tag{3}$$

where, I_{01} and I_{02} be the maximum current flowing through the junctions I and II, respectively; ϕ and 2ϕ be the phase differences across the junctions I and II, respectively. For each junction, $\omega_J = (2e/\hbar)V$ represents the Josephson frequency of oscillation of the ac current.

The resultant current can be written as

$$\begin{aligned} I &= I_{01} e^{i(\omega_J t + \phi)} + I_{02} e^{i(\omega_J t + 2\phi)} \\ &= (I_{01} e^{i\phi} + I_{02} e^{2i\phi}) e^{i\omega_J t} \end{aligned} \tag{4}$$

Considering identical junction ($I_{01} = I_{02} = I_0$) and after some mathematical exercises, the resultant current due to ac Josephson effect for two junctions can be expressed as:

$$\begin{aligned} I &= I_0 e^{i\omega_J t} (e^{i\phi} + e^{2i\phi}) \\ &= 2I_0 \cos(\phi/2) \sin(\omega_J t + 3\phi/2) \end{aligned} \tag{5}$$

For convenience, we have taken imaginary part for the resultant current. The above formulation can be extended for more than two junctions. Let us proceed for N number of identical Josephson junctions, as shown in Figure 3.

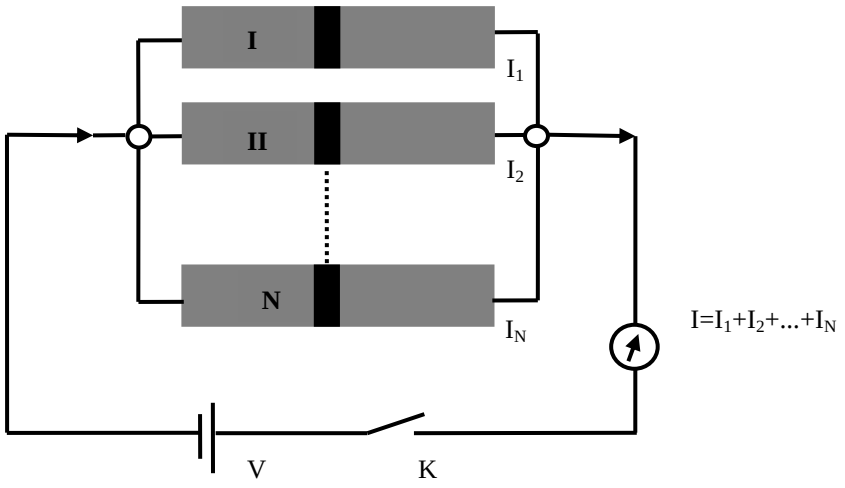

Fig. 3. Schematic diagram of N number of parallel Josephson junctions with a constant dc voltage (V).

The resultant current can be written as

$$I = I_0[e^{i(\omega_J t+\phi)} + e^{i(\omega_J t+2\phi)} + \ldots\ldots\ldots\ldots + e^{i(\omega_J t+N\phi)}]$$

$$= I_0 e^{i\omega_J t}[e^{i\phi} + e^{2i\phi} + \ldots\ldots\ldots\ldots + e^{Ni\phi}]$$

$$= I_0 e^{i\omega_J t} e^{i\phi} \frac{e^{iN\phi}-1}{e^{i\phi}-1}$$

$$= I_0 e^{i\omega_J t} e^{i\phi} \frac{e^{iN\phi/2}(e^{iN\phi/2} - e^{-iN\phi/2})}{e^{i\phi/2}(e^{i\phi/2} - e^{-i\phi/2})}$$

$$= I_0 e^{i\omega_J t} e^{i(N+1)\phi/2} \frac{\sin(N\phi/2)}{\sin(\phi/2)}$$

$$= I_0 e^{i(\omega_J t+(N+1)\phi/2)} \frac{\sin(N\phi/2)}{\sin(\phi/2)}$$

$$\mathrm{I} = I_0 \frac{\sin(N\phi/2)}{\sin(\phi/2)} \sin(\omega_J t + (N+1)\phi/2) \tag{6}$$

This is the resultant current for multi-junction ac Josephson effect in superconductors. It can be noted that for N = 2, the Equation (6) resembles to Equation (5) for two identical Josephson junctions in parallel connection, which supports our assumption.

In presence of magnetic field, an additional condition should be required for phase and flux [6, 7], like

$$\frac{2\pi}{\Phi_0} \sum \Phi_J + \phi = 2\pi \mathrm{n},\ \mathrm{n} = 0,1.2,\ldots \tag{7}$$

Here, $\Phi_0 = (hc/2e)$ is a quantum of flux and Φ_J is the flux due to the addition of Josephson junctions in presence of a magnetic field. In terms of Equation (7), the Equation (6) now can be written as

$$\mathrm{I} = I_0 \frac{\sin\left[N\pi\left(\mathrm{n} - \frac{\Phi}{\Phi_0}\right)\right]}{\sin\left[\pi\left(\mathrm{n} - \frac{\Phi}{\Phi_0}\right)\right]} \sin\left[\omega_J t + (N+1)\pi\left(\mathrm{n} - \frac{\Phi}{\Phi_0}\right)\right] \tag{8}$$

This is the resultant current for multi-junction ac Josephson effect in presence of magnetic field.

3. NUMERICAL RESULTS AND DISCUSSION

For numerical analysis, we have introduced the concept of intensity of current in comparison to the intensity of light waves. As the light intensity is equal to the square of the amplitude, the amplitude for two Josephson junctions (Equation 5) and hence the intensity can be expressed as

$$4I_0^2 \cos^2(\phi/2) \tag{9}$$

which is similar to interference phenomena of light waves observed in Young's double slit experiment.

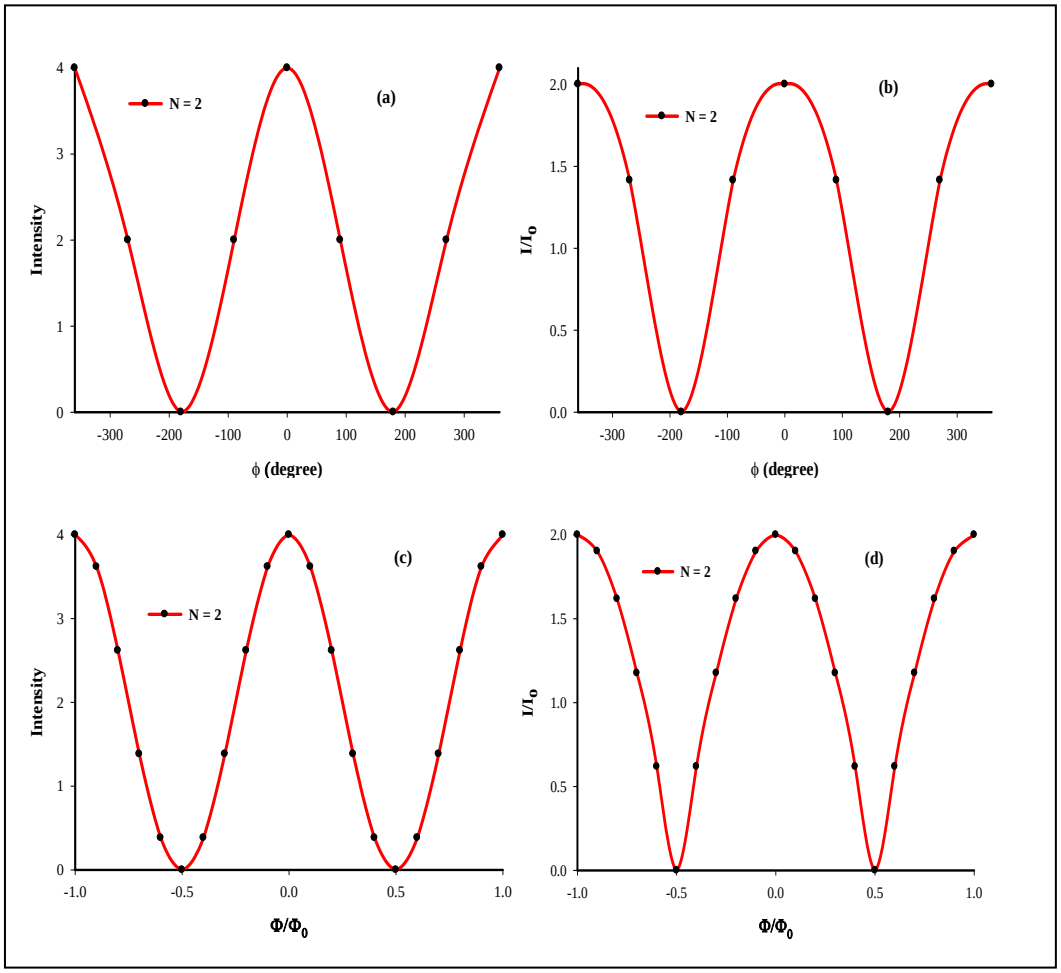

Fig. 4. Plots of (a) Intensity versus phase in absence of magnetic field, (b) maximum I/I_0 versus phase in absence of magnetic field, (c) Intensity versus Φ/Φ_0 in presence of magnetic field and (d) maximum I/I_0 versus Φ/Φ_0 in presence of magnetic field for two Josephson junctions in parallel.

Now facilitating Equation (6), the intensity of current for N (> 2) identical Josephson junctions can be written as

$$I_0^2 \frac{\sin^2[N\phi/2]}{\sin^2[\phi/2]} \tag{10}$$

which is quite similar to diffraction phenomena in optics.

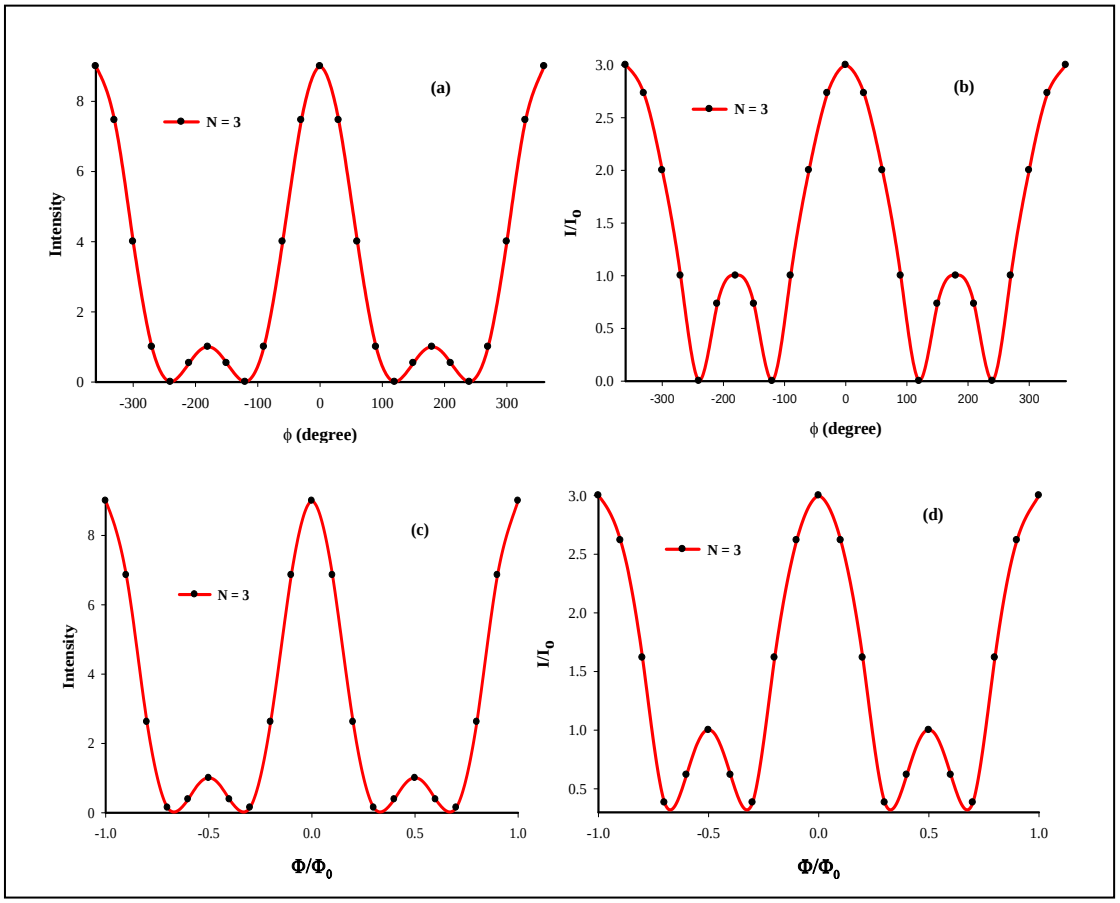

Fig. 5. Plots of (a) Intensity versus phase in absence of magnetic field, (b) maximum I/I_0 versus phase in absence of magnetic field, (c) Intensity versus Φ/Φ_0 in presence of magnetic field and (d) maximum I/I_0 versus Φ/Φ_0 in presence of magnetic field for three Josephson junctions in parallel.

In presence of magnetic field with the aid of Equation (8), the intensity of current can be expressed as

$$I_0^2 \frac{\sin^2\left[N\pi\left(\mathrm{n} - \frac{\Phi}{\Phi_0}\right)\right]}{\sin^2\left[\pi\left(\mathrm{n} - \frac{\Phi}{\Phi_0}\right)\right]} \tag{11}$$

We have considered N = 2, 3, 4 and 5 identical Josephson junctions for numerical analysis for convenience. The results for intensity and maximum current are shown in Figures (4-7), in absence and presence of magnetic field, respectively. The Figures depict the variation of intensity and current with phase and flux.

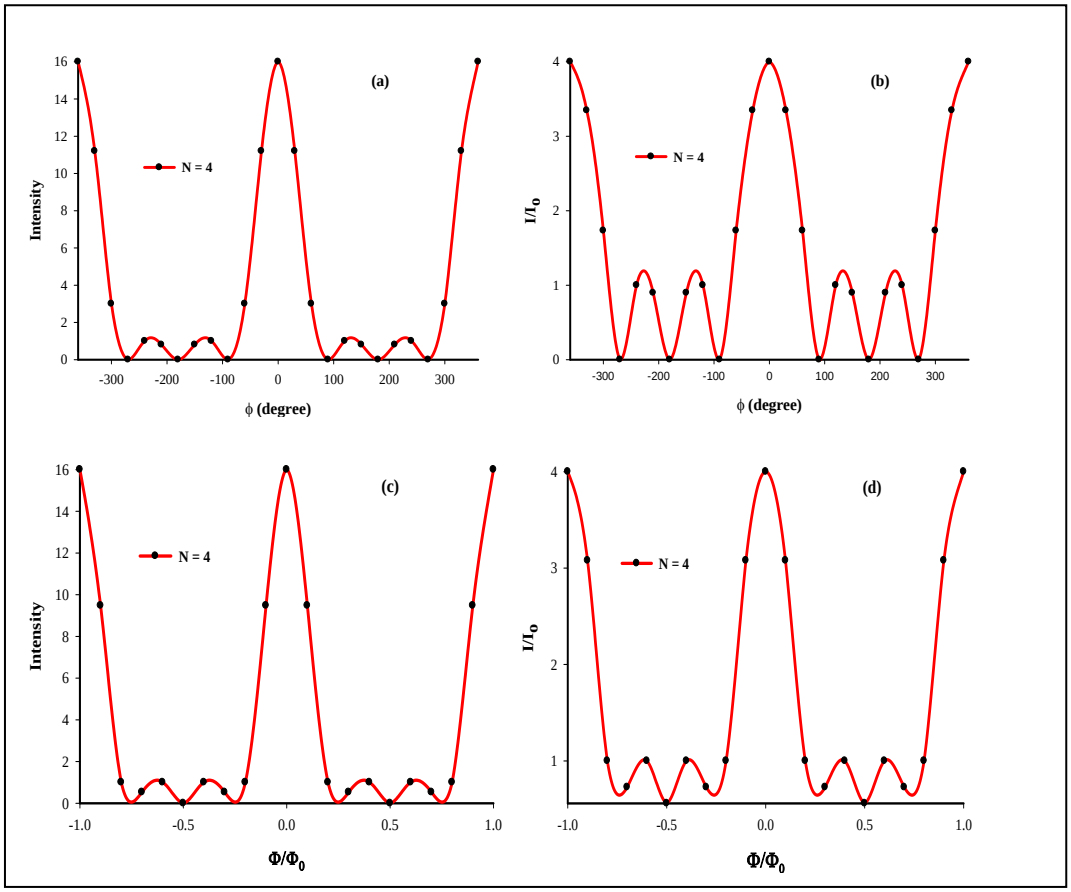

Fig. 6. Plots of (a) Intensity versus phase in absence of magnetic field, (b) maximum I/I_0 versus phase in absence of magnetic field, (c) Intensity versus Φ/Φ_0 in presence of magnetic field and (d) maximum I/I_0 versus Φ/Φ_0 in presence of magnetic field for four Josephson junctions in parallel.

For N =2, it can be considered as the interference phenomena of light as in Young's double slit experiment (Figure 4). Whereas, for N = 3, 4 and 5, it can be considered as the diffraction phenomena in 3 slits (one secondary maxima between principal maxima), 4 slits (two secondary maxima between principal maxima) and 5 slits (three secondary maxima between principal maxima), respectively (Figures 5-7). The numerical results (Figures 5-7) are comparable with the experimental results see in references [8, 9].

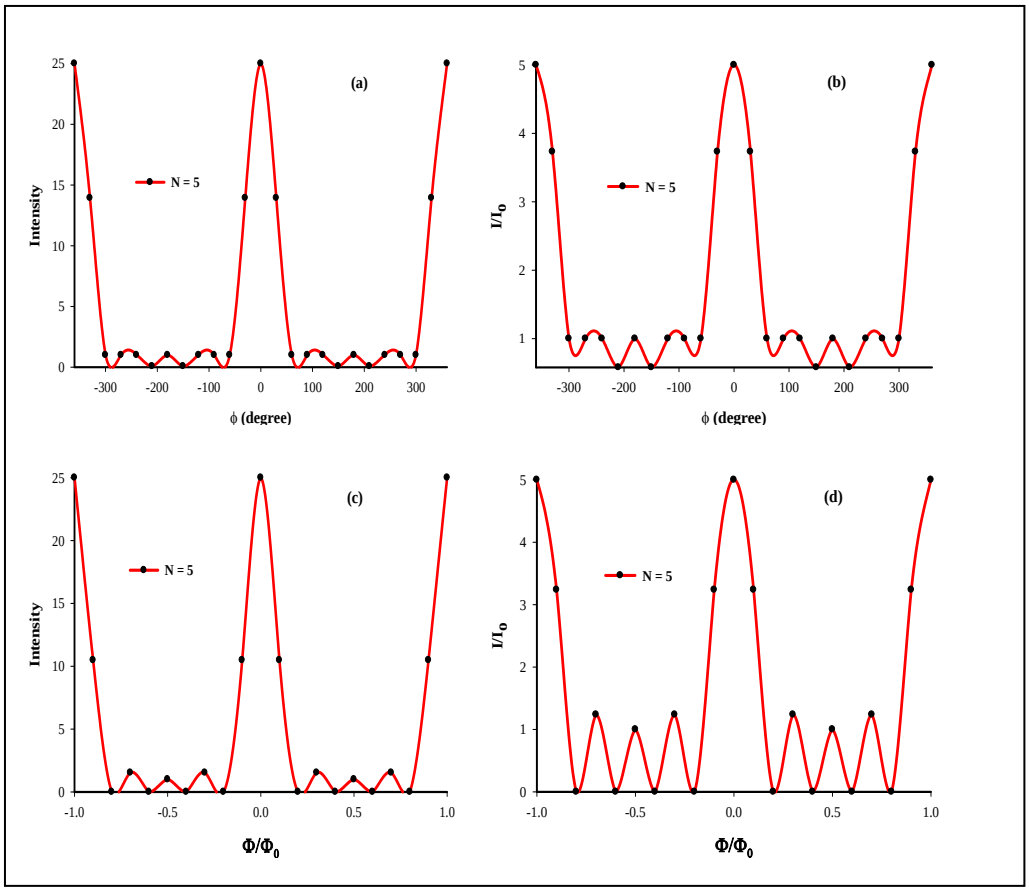

Fig. 7. Plots of (a) Intensity versus phase in absence of magnetic field, (b) maximum I/I_0 versus phase in absence of magnetic field, (c) Intensity versus Φ/Φ_0 in presence of magnetic field and (d) maximum I/I_0 versus Φ/Φ_0 in presence of magnetic field for five Josephson junctions in parallel.

For numerical analysis, we represent the resultant current amplitudes in terms of intensity compared to the intensity of light waves in the reduced form. The theoretical results, i.e., Equations (6, 8, 10 and 11) are shown here for similar N number of Josephson junctions. Both intensity and resultant maximum current variation with phase and flux are shown for clarity. It is noteworthy to mention that the size or shape of the Josephson junction is not taken into account. The amplitude or the intensity of the resultant current is increased with the increasing number of

junctions. Hence, the multi Josephson junction in parallel connections may be interesting contender for further study to find applications in superconductor devices. Besides, the power is directly proportional to the square of the amplitude and the amplitude increase with increasing number of junctions. Hence, a multi Josephson junction is capable of producing enhanced emissive power [10] in terahertz and sub-terahertz frequency ranges. The model of multi-junction ac Josephson effect may play an important role in the development of future device like power amplifier [11] as well as power converter used in superconductor technology.

4. CONCLUSIONS

A model for multi-junction ac Josephson effect in superconductor, in the presence and absence of a magnetic field, is proposed. The theoretical model draws the analogy between Josephson junction effect and optical phenomena in superconductor. The addition of two parallel Josephson junctions behaves as Young's double slit experiment, whereas it behaves as diffraction phenomena in optics for junction more than two. The observed phenomenon is owing to firstly, quantum coherence, indicating the coherent nature of Cooper pair waves in Josephson junction and secondly, increasing number of junctions in Josephson effect and number of slits in optical experiments. Finally, this model of multi-junction ac Josephson effect could be an important tool in further development of device in superconducting technology.

ACKNOWLEDGEMENT

We would like to acknowledge our great appreciation to Chittagong University of Engineering and Technology, Chittagong 4349, Bangladesh for all sorts of support.

REFERENCES

[1] B. D. Josephson, *Phys. Lett.***1**, pp 251 (1962).

[2] R. De Luca, *Eur. J. Phys.* **33**, pp 1547 (2012).

[3] A. Baroneand G. Paterno, *Physics and Applications of the Josephson Effect*, John Wiley and Sons, New York (1982).

[4] C. Poole, H. Farach, R. Creswick and R. Prozorov, *Superconductivity*, 3rd Edition, Elsevier (2014).

[5] M. Tsujimoto, Y. Maeda, H. Kambara, A. Elarabi, Y. Yoshioka, Y. Nakagawa, Y. Wen, T. Doi, H. Saito and I. Kakeya, *Supercond. Sci.Technol.* **28**, pp 105015 (2015).

[6] M. R. Islam, H. Rahman, *Turk. J. Phys.* **38**, pp 73 (2014).

[7] M. Tinkham, *Introduction to Superconductivity*,2nd Edition, McGraw-Hill Inc. (1996).

[8] P. Seidel, *Supercond. Sci.Technol.* **24**, pp 043001 (2011).

[9] M. Lucci, D. Badoni, V. Corato, V. Merlo, I. Ottaviani, G. Salina, M. Cirillo, A. V. Ustinov, D. Winkler, *J. Phys. D: Appl. Phys.* **49**, pp 065303 (2016).

[10] *New T-ray source could improve Airport security*, Cancer Detection", Sci. News, Science Daily (27 November 2007).

[11] A. Kamal, J. Clarke, M. H. Devoret, *Phys. Rev.* B**86**, pp 144510 (2012).

Bangladesh Journal of Physics

A Journal of Bangladesh Physical Society
(Keyword: Bangladesh J. Phys.)
ISSN Number: 1816-1081
Web site: www.bdphso.org

Notes to the Authors for Manuscript Preparation

1. **Publications Scheme**: Bangladesh Journal of Physics publishes half-yearly.
2. **Refereeing**: All contributions submitted will be refereed. The Board of Editors reserves the right to reject manuscript and to edit a contribution if necessary.
3. **Preparation of Manuscripts**

   The following are the requirements which should be met before submission of the manuscripts to Bangladesh Journal of Physics.

(i) **Manuscript**

The original typescript for **Review article** and **Full paper** should be typed on one side of good quality offset paper, with double spacing and a wide margin. The title page should contain title, author(s) name, address (es), abstract and **Keywords**, The main text should start on a new page. All pages should be numbered. The paper must be divided into sections starting preferably with Introduction and ending with Conclusions. The main sections should be numbered as 1, 2, 3, etc. and the subscriptions as 2.1, 2.2, etc.

Rapid communication is devoted to the announcement of timely and important results. Contributions to this and **Note** sections should not exceed 8 typed pages (double spaced), including figures, equations, tables and references. They should follow the same style and format as the full paper except that they need not be divided into sections.

A soft copy of the manuscript (the Text in WORD 97-2003 or higher Version containing Figures, images, tables, etc) should be sent to the Editor in the address mentioned below with a mention of the field under which the paper is being submitted.

(ii) **Title**: The title should be brief and yet convey to the reader the particular nature of the contents of the paper.

(iii) **Address**: The name(s) of the author(s) and address (es) of the institute where the research work was done should be indicated. The name of the author to whom correspondence is to be addressed, should be underlined. The present address (es) of the author(s), if it is different, may be given as a foot note. E-mail address and Telephone number of the corresponding author must be provided.

(iv) **Abstract:** An abstract of less than 200 words is required. It should contain the essence of the result achieved.

(v) **Keywords:** Appropriate Keywords (Not more than three) must be provided for indexing and information retrieval services.

(vi) **Text:** In the preparation of text, the authors should pay attention to the language (usage of words grammar and construction of sentences), logical presentation, enumeration of assumption made, justifications of approximations made etc. and all the limitations must be stated wherever and wherever necessary. Moreover, a paper must be self-contained, its presentation being clear, concise and satisfactory.

(vi) **References**

All references referred to text, tables and figures of a manuscript must be combined in a single list, numbered consecutively in their order of first appearance and arranged in the same order at the end of the text material. They should be cited in text by Arabic numerals in square brackets at appropriate places of a sentence, for example [1], [3], [4-6], etc. The references cited should be limited to the absolute minimum and the list to the submitted in a separate sheet containing names of all authors (**et al. is not allowed**). They should be as complete as possible and be presented at follows:

[1] U. Fano and A. R. P. Rao, Atomic Collisions and Spectra (New York: Academic), Vol 1, Ch 2, Sec. 4, p-25 (1986).

[7] T. Atsumi, T. Isihara, M. Koyama and M. Matsuzawa, Phys. Rev. A **42** (1990) 6391.

[11] T. Le-Brum, M. Lavollee and P. Morin, X-ray and Inner Shell Processess (AIP conf. Proc. 215) eds T. A. Carison, M. O. Krause and S. Manson (New York: AIP) pp-846 (1990).

[14] S. B. Hansen, K. B. MacAdam and L. G. Gray, 12^{th} Int. Conf. on Atomic Physics (Ann. Arbor) Abstracts, pp-12, (1990).

[15] H. Pauly, Atomic and Molecular Beams Methods eds. G. Scoles, D. Bassi, U. Buck and D. Laine (London: Oxford University Press), pp-83, (1988).

[19] W. Fritsch (private communication) (1980)

[21] K. B. MacAdam (to be published) (1991).

[23] T. Roy, Band Structure Calculation of an Alloy, Ph. D. Thesis (University of Calcutta, India) (1992).

(xi) **Foot notes:** As far as possible, footnotes should be avoided.

(xii) **Appendices:** All appendices should be numbered consecutively and typed on separate sheet.

Manuscripts which do not conform to these conventions are returned to the authors immediately.

Corrections and Modifications

Authors are requested to exercise utmost care in preparing the manuscripts so that there is little need to incorporate alterations at the Final stage. Extensive modifications at this stage are not allowed.

Correspondence

All correspondence regarding the manuscripts should be sent to: The Editor, Bangladesh Journal of Physics, Department of Physics, Bangladesh University of Engineering and Technology (BUET), Dhaka-1000, Bangladesh, with full reference to the paper concerned i.e., the name(s) of author(s), the full title and the reference number, if any. Soft copy should be sent to the following address:

E-mail: *bjp_bps@yahoo.com*

Important Instruction to the Contributors

The authors are requested to include the following important Information in their Covering Letters while submitting the papers to Bangladesh Journal of Physics.

(i) The mailing address of the Corresponding Author with E-mail, Fax and Phone Nos.

(ii) A list of Potential Referees with addresses for the submitted Manuscript.

(iii) The specific Field under which the Manuscript is to be placed.

(iv) Whether the Manuscript should be published as (a) Review, (b) Full paper, (c) Short note, (d) Rapid communication.

(v) Justification if the Manuscript is to be published as a Rapid communication.

Bangladesh Physical Society

Web site: www.bdphso.org
E-mail: bdphso@gmail.com

Executive Board
(2018-2019)